

Energetics of Elementary Steps in Catalysis and Their Use to Search for New Catalysts

Christopher A. Wolcott

A dissertation

Submitted in partial fulfillment of the

Requirements for the degree of

Doctor of Philosophy

University of Washington

2014

Reading Committee

Charles T. Campbell, Chair

Eric Stuve

Stuart Adler

Peter Pauzauskie

Program Authorized to Offer Degree

Chemical Engineering

©Copyright 2014

Christopher A. Wolcott

University of Washington

Abstract

Energetics of Elementary Steps in Catalysis and Their Use to Search for New Catalysts

Christopher A. Wolcott

Chair of Supervisory Committee:

Professor Charles T. Campbell

Chemical Engineering

We live in a society based upon the mass production of chemicals. Whether it is the fuel in a car, the fertilizers used to make food, or the plastics present in just about everything, these chemicals are so ubiquitous that it is difficult to imagine living in a world without them. Nearly all consumer chemicals are produced through a catalytic process, the vast majority of which are heterogeneous. On top of their current, massive presence, heterogeneous catalysts are also expected to play an important role in new emerging technologies such as fuel cells, hydrogen production, green chemistry, and more. Considering their ubiquity in the present and their potential uses in the future, it is no surprise that improving catalyst performance is a very active area of research. Yet despite their ubiquity, and despite their long history of active study, there remains much which is unknown about the fundamentals of catalysts on surfaces. One of the major gaps is in quantitative understanding of the energetics of elementary steps in catalytic

reactions on surfaces. The stability or instability of molecules and molecular fragments adsorbed on surfaces in these elementary steps is KEY to understanding what makes one material an effective catalyst and another less effective.

In general, one must use single-crystal model catalysts to produce well-defined adsorbates. Classic studies of the energetics of adsorbates on such surfaces have typically involved techniques (such as temperature programmed desorption or equilibrium adsorption experiments) which limit the types of systems which can be studied to those where adsorption is reversible. For most catalytic intermediates present in these elementary steps, this is not the case. Upon adsorption and heating many molecules fall apart and produce strongly bound adsorbates which further dissociate at higher temperatures, or will not leave the surface until they have reacted with something else. Single crystal adsorption calorimetry (SCAC) is a fairly new technique which allows one to probe the heats of formation of such adsorbates for the first time.

In this thesis SCAC is used to study the dissociative adsorption of diiodomethane on Pt(111) to produce adsorbed $-CH_2$ and $-CH$, and water on $Fe_3O_4(111)$ and $NiO(111)$ to produce adsorbed $-OH$. This work expands the library of adsorbates on transition metal surfaces which has been studied by SCAC, and is among the first ever measurements of molecules on well-defined oxide surfaces using SCAC. These results are compared to density functional theory (DFT) calculations of adsorbate energetics, and their use as computational benchmarks is discussed. A new, universally-applicable method of data analysis for SCAC is also developed which allows for the extraction of heat data even in the presence of complex surface reaction/diffusion dynamics without any need for kinetic modeling as required in previous analysis methods, thus greatly expanding the versatility of SCAC.

Finally a new method of computational catalyst screening is presented which uses the concept of degree of rate control to simplify calculations compared to the standard method developed by Jens Nørskov's group. It greatly reduces the number of adsorbate energies needed to predict the reaction rate for a new catalyst, and provides greater accuracy when studying materials with similar properties to the reference catalyst used. The Nørskov method is more robust when extended to materials that are dissimilar. The new method presented here is thus expected to be an important complimentary tool to Nørskov's method for high-throughput computational screening.

Taken together, the results presented in this dissertation show the importance of experimental measurements for guiding the development of fast quantum mechanical methods like DFT to more closely approach thru "chemical accuracy" in energetic prediction, and how one could use "chemically accurate" DFT energies to rapidly screen potential catalysts for computational catalyst discovery to advance energy and environmental technologies.

Contents	
Acknowledgements	15
Chapter 1: Introduction	16
Tables	24
Chapter 2: Instrumentation	25
Figures	28
Chapter 3: Method for Direct Deconvolution of Heat Signals in Transient Adsorption Calorimetry	31
Introduction	31
Signal Generation and Pulse Shape	35
Direct heat extraction using FFT	38
Comparison of Results to Method of Silbaugh	43
Conclusions	46
Figures	47
Chapter 4: Energetics of Adsorbed CH₂ and CH on Pt(111) by Calorimetry: the Dissociative Adsorption of Diiodomethane	55
Introduction	56
Experimental Methods	58
Computational methods	62
Experimental Results	64
DFT Results	67
Discussion	68
Conclusions	77
Tables and Figures	79
Chapter 5: Energetics of Adsorption of D₂O on Fe₃O₄ (111) and NiO(111)	92
Introduction	92
Experimental details	96
Growth of Fe ₃ O ₄ (111) Film	96
Growth of NiO(111) Film	97
Experimental Procedure for Measuring Heat of Adsorption of D ₂ O on Oxide Surfaces	97
D ₂ O on Fe ₃ O ₄ (111) Results	98
D ₂ O on NiO(111)	99

D ₂ O on Fe ₃ O ₄ (111) Discussion	100
D ₂ O on NiO(111) Discussion.....	102
Conclusions	105
Figures and Tables.	106
Chapter 6: Degree of Rate Control Approach to Computational Catalyst Screening.....	111
Introduction	112
Degree of Rate Control as a Screening Method for DFT	118
Application of Method to Evaluate Catalysts for Methane Steam Reforming and Comparison to Prior Results by Linear-Scaling Approach	119
Computational Methods	121
Results	122
Computational Time Comparison	130
Comparison to Previous Theory and Experiments.....	131
Conclusions	132
Tables	134
Figures	137
Conclusion	142
References.....	146
Curriculum Vitae	160

List of Figures and Tables

Table 1.1. Comparison of previously measured adsorbate energies for species measured by SCAC on Pt(111) with those calculated by different DFT methods. (Prepared by Trent Silbaugh ⁸⁰)	24
Figure 2.1. Photograph of the interior of the SCAC instrument described in this chapter. Each element is labeled as corresponds to those used in text.	28
Figure 2.2. Quadruple mass spectrometer response for zero sticking pulse on Au flag (blue) and a the non-sticking fraction of an experimental pulse (red). Shaded area is 100ms pulse window used to differentiate short and long term sticking. Comparing the areas of the shaded region between the Nonsticking and zero sticking fractions allows the calculation of the fraction of molecules sticking to the surface during the timescale of the heat measurement. Because some molecules may also desorb slowly, it is necessary to calculate the “long term” sticking fraction, which determines the total coverage of molecules on the surface. This is accomplished by comparing the areas of the two peaks across the entire pulse window	29
Figure 2.3. Pyroelectric heat detector response for laser pulse and molecular pulse. In the simplest case (shown here), without and slow heat deposition step, the energy of the molecular beam pulse can be determined by scaling the energy in the laser pulse so that the two curves match. If a slow heat deposition step occurs, the molecular pulse appears broadened relative to the laser, and a more complicated analysis is needed to extract heat data (see Chapter 3).	30
Figure 3.1. Comparison of typical normalized response signals measured for single pulses of the laser beam and the molecular beam (MB), for a case where the latter shows peak broadening due to slow kinetics. Also shown is the incident beam profile, which is approximately a square wave. This profile is essentially identical for both the laser and the molecular beams, and its shape is determined by the diameter of the beam, the geometry of the chopper wheel and its rotational velocity. The incident beam profile shown here was collected by measuring the direct molecular beam intensity with a quadruple mass spectrometer (QMS).	47
Figure 3.2. A typical heat deposition profile ($I(t)$, here a square-wave model of the incident laser power) is convoluted with the instrument response function ($R(t)$) to yield the measured detector signal ($S(t)$). Here, $R(t)$ was actually calculated by deconvolution of the known $I(t)$ from the measured $S(t)$, as detailed in the text. Because the instrument response is partially determined by the quality of the physical contact between the heat detector and the sample, it is necessary to extract the instrument response function every time a new contact is established (once for each heat-versus-coverage run). The laser power input function is modelled here as a square wave. It was also modelled as a trapezoidal wave based on the known open/close profile of the chopper in this system, which produced an identical instrument response function (see text).	48
Figure 3.3. Top: The incident beam profile and typical response signals measured for the laser beam and the molecular beam (MB), reproduced from Fig. 3.1. Bottom: the incident power at the detector from the molecular beam as a function of time, extracted by deconvoluting the instrument response function from the MB heat signal using the FFT method. The square wave incident beam model is also shown. The deconvoluted MB signal is the result of deconvoluting	

the MB heat signal with the instrument response function, while the deconvoluted laser signal is the result of deconvoluting a single laser heat signal with that same instrument response function. (The average of many laser heat signals is used to extract the instrument response function.) It can be seen that for this individual MB pulse, the deconvoluted heat signal is broader than the incident beam, showing that heat is deposited on a slower time scale than during the laser pulse. The deconvoluted pulse tail decays quickly towards the baseline zero, but continues to be distinguishable above the baseline noise for almost 1s before being overwhelmed by the periodic noise introduced by this method. 49

Figure 3.4. Differential heat of adsorption of CH₂I₂ on clean Pt(111) at 125K as a function of CH₂I₂ coverage, extracted by integrating each deconvoluted pulse (see Fig. 3.3) over the different integration windows stated. By increasing the integration window by time increments that are ¼ of the period of the dominant periodic noise by moving either to earlier start times (a) or later stop times (b), this shows that no systematic change in heat is found at most coverage. Thus, the periodic noise does not have a significant impact on the choice of window for integration. However, at very low coverages, which had the most broadened heat signal pulses, increasing the integration window to longer times does increase the heats systematically as it captures more and more of the slow heat deposition. The heat stops increasing when this is extended to ~1000 ms, after which the effect saturates (see Fig. 3.5). 50

Figure 3.5. Differential heat of adsorption of CH₂I₂ on Pt(111) at 125K as a function of CH₂I₂ coverage obtained using different time window widths for integrating the heat pulses. These heats were extracted by integrating each deconvoluted pulse (see Fig. 3.3) over the specific time windows shown. A large enough window must be selected to capture all of the heat deposited (see low coverage results in Fig. 3.4), and ideally one would integrate across the full time window. This shows, however, that as the integration window gets larger, the noise increases, although the average heat remains unchanged at most coverages. At low coverages where the heat signal is most broadened, the heat increase with integration window until 300-1000 ms, above which it has the same average. This shows that whatever slow kinetics are occurring on the surface, they have already completed by 1000 ms. 51

Figure 3.6. The standard deviation of the heat measured in Fig. 3.5 over the coverage range from 0.2 to 0.4 ML (where the heat is nearly constant with coverage) as a function of integration window width beginning at 0.3 s. The standard deviation increases proportional to the integration window width. The best selection of window width was decided based on seeking to minimize this noise while simultaneously capturing all of the heat deposition occurring for a pulse of gas (which time duration varies depending upon the reaction being studied and surface temperature). 52

Figure 3.7. Comparison of differential heat of adsorption versus coverage results for CH₃I on clean Pt(111) at 270 K, between the convolution fitting method of Silbaugh et al.⁴⁶ (blue points) and the direct deconvolution method of this paper (red points). In Silbaugh's method, four pulses were averaged to reduce noise. Each of the points of Silbaugh is essentially the average of the four adjacent points from the method of this paper. The best-fit lines shown are very similar, and

represent the equations: $y = (259-969x)$ kJ/mol using the convolution fit method, and $y = (263-911x)$ kJ/mol using the direct deconvolution method..... 53

Figure 3.8. Bottom: Comparison of the input power versus time due to the heat of adsorption followed by dissociation for CH₃I adsorption on Pt(111) at 270 K for a typical 0.0046 ML pulse within the coverage range 0-0.02 ML, as calculated from: 54

(a) The two-step model of Silbaugh et al.⁴⁶ for this condition wherein CH₃I first adsorbs molecularly with a heat of 184 kJ/mol and then dissociates via a first-order reaction with time constant $\tau = 170$ ms and heat of 64 kJ/mol (purple, dashed curve). Also shown are the separate heat inputs from the fast step (blue) and slow step (green). The curve at the top shows the simulated signal waveform for this same exact two-step heat input model, as generated using the simulation method of Silbaugh et al. which sums heat-scaled waveforms for its two steps, using the measured lineshape for the signal response to laser heating for the first, fast step and its convolution with first-order exponential decay kinetics for the slow step. 54

(b) Deconvolution of top simulated signal to remove the instrument response function (shown in Fig. 3.2). 54

Curves (a) and (b) agree, except for the damped periodic noise that results from deconvoluting over the finite time window used (4000 points over 5 s). 54

Figure 4.1. Typical deconvoluted heat versus time plot for a single 100 ms gas pulse that occurs at ~0.45 s on this scale. The method of deconvolution is explained in the text. Integration of the signal (μ W) over time (s) yields the total adsorption energy (μ J) for that pulse. Discussion of the best choice of integration time-window is given in the text. 79

Figure 4.2. Differential heat of adsorption of CH₂I₂ on Pt(111) at 100 K as a function of total CH₂I₂ coverage (θ). Dissociation to CH_{2,ad} + 2 I_{ad} occurs in the first 1/8 ML with a heat of (222-4800) kJ/mol. Continued dosing leads to adsorption in a second layer and then multilayer, with the heat of adsorption eventually approaching the bulk heat of sublimation for CH₂I_{2,s} at 100K (measured to be 89 kJ/mol, estimated to be 87 kJ/mol from bulk thermodynamic values, see text). 80

Figure 4.3. Differential heat of adsorption of CH₂I₂ on Pt(111) at 210 K as a function of total CH₂I₂ coverage (θ). Dissociation to CH_{ad} + 2 I_{ad} + H_{ad} occurs in the first 0.09 ML with a heat of (533-14300) kJ/mol. Continued dosing leads to adsorption in a second layer on top of the layer of fragments and atomic species. The long-term sticking probability measurements, not shown, show a rapid drop from unity to zero between 0.15 ML and 0.18 ML. 81

Figure 4.4. Summary of the differential heats of adsorption of CH₂I₂ on clean Pt(111) as a function of total CH₂I₂ coverage measured at different temperatures. These data are interpreted as follows (see text): At 100 K, adsorption produces CH_{2,ad} plus 2 I_{ad} in near-neighbor sites. At 210 K, dissociation to CH_{ad} + 2 I_{ad} + H_{ad} occurs in the first 0.09 ML. Increasing temperature above 100 K results in an increasing fraction of further decomposition of CH_{2,ad} to CH_{ad} + H_{ad}, which is enabled by the increasing extent of diffusion of I_{ad} away from the near-neighbor sites of CH_{2,ad}, thus producing free Pt sites needed for CH_{2,ad} decomposition (see text). 82

Figure 4.5. Top (upper panels) and side (lower panels) snapshots of the DFT (optB86b vdW-DF) calculated minimum-energy configurations for the various species adsorbed on Pt(111): (a) CH₂I₂; (b) CH₂I; (c) CH₃; (d) CH₂; (e) CH; (f-g) CH₂+2I; and the transition states for C-I bond scission in (h) CH₂I_{2,ad} and (i) CH₂I_{ad} coadsorbed with one I_{ad}. Large white, large grey, medium black, and small white spheres represent Pt, I, C, and H atoms, respectively. The coverage is 1/16 ML for (a-e), and 1/16 ML for (f, h, i) and 1/9 ML for (g), respectively, referring always to the starting amount of CH₂I₂ needed to generate each structure. The surface unit cell vectors are indicated in (f) and (g) for the (4×4) (corresponding to 1/16 ML) and (3×3) (corresponding to 1/9 ML) surface unit cells, respectively. The C-I bond distance (dC-I) at the two transition states are: (h) 3.180 Å; (i) 3.034 Å. 83

Figure 4.6. DFT-calculated reaction energy profile for the dissociative adsorption of CH₂I_{2,g}. Points 2-4 are each calculated on a (4×4) surface unit cell, whereas the last point is calculated with each adsorbate on a separate (4×4) surface unit cell, approximating the zero-coverage limit. The numberings of the three activation barriers for the successive decomposition of CH₂I_{2,ad} to CH_{ad} are indicated, as referred to in the text. 84

Figure 4.7. Thermodynamic cycle for the formation of adsorbed methylene on Pt(111) (with two nearby I_{ad}) from CH₂I_{2,g} at 100 K, used to estimate the standard heat of formation and bond enthalpy of CH_{2,ad} to Pt(111). The measured number reported in red is the integral heat of adsorption up to a coverage of 0.04 ML from Fig. 4.1. Numbers in blue are calculated, and numbers in black are taken from literature as described in the text. This heat of formation is strongly affected by the presence of two nearby I_{ad} (see text). 85

Figure 4.8. Thermodynamic cycle for the formation of methylidyne on Pt(111) from CH₂I_{2,g} at 210 K, used to estimate the standard heat of formation and bond enthalpy of CH_{ad} to Pt(111). The measured number reported in red is the integral heat of adsorption up to a coverage of 0.04 ML from Fig. 4.3. Numbers in blue are calculated, and numbers in black are taken from literature as described in the text. 86

Table 4.1. Best-fit lines for experimental differential heats of adsorption, heat of formation, and bond enthalpies versus coverage for various fragments on Pt(111). Coverages here are defined for each reaction listed as the number of reactant species (CH₂I₂, CH₃I, or I) adsorbed on the surface of the Pt(111) single crystal divided by the number of Pt atoms on the Pt(111) surface (1.5 × 10¹⁵/cm²). Heat of adsorption determined by calorimetry for the reactions listed except for I_{ad}, which values come from TPD. Heats of formations were calculated using the integral heat of adsorption (differential heat of adsorption integrated over the stated coverage range) together with known enthalpies from the literature, as explained in Figs. 4.6 and 4.7. The numbers given here are from integration of the differential heat of adsorption's linear fit given in the 3rd column. (The data presented elsewhere in the paper come from numerical integration of data points.) ... 87

Figure 4.9. DFT-calculated differential dissociative adsorption energy of CH₂I_{2,g} → CH_{2,ad} + 2I_{ad} as a function of total dissociated CH₂I₂ coverage. The zero-coverage limit is approximated with each product calculated on a separate (4×4) surface unit cell. 88

Table 4.2. Comparison of experimentally measured bond energies of adsorbates to Pt(111) with DFT calculations.....	89
Figure 4.10. Experimental enthalpy landscape for stepwise dehydrogenation of methane on Pt(111) at low coverage. Adsorbing gas and its total coverage used for SCAC measurements are indicated in parentheses under each species. For other species, see text for citations.	91
Figure 5.1. Heat of adsorption of D ₂ O on Fe ₃ O ₄ (111) at 100K as a function of D ₂ O coverage. Surface of Fe ₃ O ₄ (111) believed to already be hydroxylated before dosing begins. Adsorption is believed to be molecular D ₂ O adsorption on top of hydroxyls. Break is seen at 1 ML coverage and at 2 ML coverage suggesting growth of first and second layers. Heat eventually reaches the heat of sublimation at ~2.5 ML which is also the multilayer heat. Data is normalized to heat of sublimation in multilayer region because reflectivity of Fe ₃ O ₄ (111) film is unknown and has been seen to depend on thickness as discussed in the text. The heat of adsorption of D ₂ O at 150 K is seen to be ~10-15 kJ/mol higher than at 100K in the first ML. The explanation for this is unclear, but it could be that the water molecules are more mobile at 150 K and are able to find more energetically favorable sites to adsorb. At 150 K no sticking is seen beyond ~1.25 ML of D ₂ O coverage and no multilayers are formed.....	106
Table 5.1. Summary of ultimate saturation coverage for D ₂ O on Fe ₃ O ₄ calculated using sticking probabilities measured simultaneous to calorimetric measurements.....	107
Table 5.2. Comparison of experimental results of this paper with TPD and DFT numbers for molecular (associative) adsorption of water on Fe ₃ O ₄ (111). SCAC data reported is the integral heat in the first monolayer of D ₂ O coverage.	108
Figure 5.2. Heat of adsorption of D ₂ O on NiO (111) at different temperatures as a function of D ₂ O coverage. Surface of NiO(111) believed to already be hydroxylated before dosing begins. Adsorption is believed to be molecular D ₂ O adsorption on top of hydroxyls. Break is seen at 1 ML coverage at 100K, where heat of sublimation (which is equal to the multilayer heat) is reached. Data is normalized to heat of sublimation in multilayer region because reflectivity of NiO(111) film is unknown. Experiments performed at higher temperatures (150K) yielded similar, though slightly lower heat curves out to 1 ML, at which point the sticking probability dropped to 0. The slightly lower heat is attributed to the heat capacity of water as discussed in the text. Going to still higher temperatures (>220K) resulted in identical heats, but lower sticking probability even at zero coverage.	109
Figure 5.3. Sticking probability for D ₂ O on NiO(111) as a function of D ₂ O coverage and temperature. 100K sticking probability is 1 at all coverages, and is not shown. Break at 1 ML of coverage at 150K is similar to what has been observed for water on other surfaces where multilayers are not formed. Higher temperatures result in smaller coverages being reached before sticking probability becomes 0.	110
Table 6.1. Reaction conditions used in microkinetic model for steam reforming of methane, from Xu et al. ²³⁵ . These are similar conditions to those used in the experiments conducted by Jones et al. ²³⁴ they. Note that these concentrations correspond to 29 % conversion starting from pure methane and water. The total pressure (P) is nearly constant throughout the reactor.	134

Table 6.2. The degrees of rate control for all intermediates and transition states for Rh(211) at the conditions of Table 6.1, calculated using CatMAP software and the microkinetic model laid out in this paper.....	135
Table 6.3. Comparisons of the ranking of catalytic activities between different metals which are similar (defined as $\Delta E_M < 1.5$ eV, where ΔE_M is the distance from Rh on a plane of E_{C^*} , E_{O^*} , formation energies, see text of Fig. 6.3) to Rh for steam reforming of methane from experiments and theory.....	136
Figure 6.1. Volcano plot of catalyst activity (log TOF) for steam reforming of methane on the (211) face of different metals at the conditions of Table 6.1, plotted as a function of the two descriptors used in the most common method for computational catalyst screening: the formation energies of adsorbed O and C atoms. The energies for all other species needed in the microkinetic model were calculated from these descriptors using linear scaling relations. Three plots are shown, A) is the original volcano plot calculated by Xu et al. B) is the volcano plot produced in this paper in an attempt to reproduce that of Xu et al. and the differences between the two are discussed in the text. C) shows the log of the ratio of the TOFs between these two plots, and it can be seen that excellent agreement is seen near the top of the volcano (less than 1 order of magnitude difference) and good agreement (2 or less orders of magnitude difference) is seen for all cases where E_{O^*} is greater than -1 eV.	137
Figure 6.2. A plot of the relative rates of methane steam reforming for the (211) face of different metals, plotted versus the two new descriptors proposed in this paper: the energies of the two species in the reaction mechanism with the highest magnitude degrees of rate control. The rates were estimated using Eq. (6.6), assuming that only the two most rate-controlling species, the adsorbed CO intermediate of energy E_{CO^*} and the transition state of energy E_{C-O^*} , determine the rate. The color axis is the rate relative to the reference metal, (r_n/r_o) from Eq. (6.6) and plotted logarithmically. The red dots represent the calculated rates for various catalytic materials with their relative energies $E_{C-O^*,n}$ and $E_{CO^*,n}$ being the only two parameters which change relative to the purple dot, which represents the reference catalyst, Rh. The energies of the species on each metal are taken from Medford et al. and were all calculated directly by DFT on the (211) crystal surface. By definition, the purple dot (Rh), should have a relative rate equal to 1, all worse catalysts have relative rates below 1, and better catalysts above 1. Used as a screen for potential new catalysts, one sees here that materials with better rates than Rh require descriptor values in the range: $E_{CO^*,n} > E_{CO^*,Rh}$ and $E_{C-O^*,n} < E_{C-O^*,Rh}$. In these reaction conditions, there are actually three species with high degrees of rate control on Rh, so greater accuracy could be achieved by including this third species in Eq. (6.6), as done in Fig. 6.3 below.	138
Figure 6.3. A comparison of the expected relative rate versus Rh(211) for different metals at the conditions of Table 6.1 as a function of distance from Rh on a plane of M-C (E_{C^*}), M-O (E_{O^*}) formation energies. Four sets of numbers are shown. The purple triangles are the rates calculated in this paper using the Nørskov-Bligaard Direct method with linear scaling relationships, NB Direct LS. The rates from this NB Direct LS method are off scale for Ag, and Au at values of -18.8 and -19.0, respectively. The X points are calculated using the DRC method of this paper (ie.,	

Eq. (6.6)) with three descriptors (3D), the energies of the three species with the largest DRCs: CO*, C-O*, and C*, with the formation energies for each species in this case (DRC: LS, 3D) taken from the linear scaling relationships used to generate Fig. 6.1 (except for the Rh reference). These green **X**'s and the purple triangles show excellent agreement for metals similar to Rh. The blue diamonds are calculated also using the DRC method of this paper with the same three descriptors, s only now getting their energies directly from DFT calculations without invoking linear scaling approximations (DRC: DFT, 3D). Lastly, the orange circles are calculated using the DRC method of this paper with numbers from DFT, but now only using two descriptors (2D), the energies of the two species with the largest DRCs: CO* and C-O* (DRC: DFT, 2D). These points are identical to the points in Fig. 6.2. The X-axis positions for Pt and Pd are nearly identical and so their points have been nudged apart by 0.1eV here in order to more clearly differentiate those points. Points not shown are outside the range shown..... 139

Figure 6.4. Degrees of rate control for different species as functions of E_{C^*} and E_{O^*} descriptors used in linear scaling relationships calculated by CATMAP. Species are A) C*, B) CO*, C) O*, D) C-O*, E) C-OH*, and F) O-CH*. The variability in these degrees of rate control corresponds to the observation in Fig. 6.3 that the further one moves from Rh in descriptor space, the more inaccurate the “constant DRC method” of predicting rates (i.e., Eq. (6.6)) becomes. 140

Figure 6.5. Comparison of estimated computer time needed for catalyst screening as a function of the number of surfaces to be screened. The black line shows the time for the traditional Nørskov-Bliggaard approach. The blue line shows the integrated DRC method with transition-states computed using DFT, while the red line assumes that transition-states are estimated from linear scaling relationships. For this plot, reasonable values of $N_I = N_T = M = \alpha = 10$ and $N_{I,K} = N_{T,K} = 1$ were used. These numbers will differ from system to system, and in particular α will vary considerably based on the transition-state and the search algorithm used. However, the qualitative behavior shown here will remain. 141

Acknowledgements

I would like to thank Isabel X. Green for all of her assistance in collecting the SCAC data for the diiodomethane on platinum and water on magnetite projects. I would like to thank Trent L. Silbaugh for his assistance in troubleshooting and problem solving when the instrument was uncooperative. I would like to thank the collaborators I worked; Ye Xu, who performed the DFT calculations for the CH₂I₂ project; and Felix Studt and AJ Medford who helped us with the microkinetic modeling, analysis, and development of the DRC screening methodology. I would like to thank Brian Holm, John Heutink, and Ed McArthur for all of their assistance and expertise in the UW Chemistry Machine Shop, working on a homemade instrument would have been completely impossible without their help repairing, designing, and machining components as we worked to improve the functionality of our instrument. I would like to thank Lon Buck, Bill Beaty, and Roy Olund in the UW Chemistry Electronics Shop; there is no good way to estimate the amount of time and frustration their expertise in troubleshooting electronics saved me, but I am sure that without them I'd still be pulling my hair out trying to find that one bad transistor, capacitor, or some other two cent electronic component. I would like to thank all my family and friends for their continuing, unwavering support throughout my graduate student career. Finally and most importantly, I would like to thank Charlie Campbell and all of the other members of the Campbell group for all the support, assistance, and encouragement they provided every day. There is no way I would be where I am today without you.

Chapter 1: Introduction

The modern technological world could not exist without the development and improvement of heterogeneous catalysis over the past century in critical areas such as fertilizer production, fuel refining, and plastics production¹⁻⁴. Given the significance and scale of these three industries in particular it is no surprise that there is a tremendous amount of effort spent to understand and improve catalytic efficiency, selectivity, and to drive down catalyst cost through rational catalyst design⁵. At the same time there is desire for improved catalytic materials for new applications such as fuel cells⁶⁻¹¹, green chemistry¹²⁻¹⁷, and hydrogen production¹⁸⁻²². In order to improve the rate of heterogeneous catalyst development it is necessary to gain a better understanding of the fundamentals of catalysis, a task which surface scientists have been pursuing for years with great success, recognized with the 2007 Nobel Prize.

Classically, much of catalyst design has often been done through complicated combinatorial experimentation built around tweaking existing catalysts or trying to find catalysts with similar but improved behavior to those currently available²³⁻²⁵. Given the complexity of a typical industrial catalyst, which might typically include mixed metal nanoparticles with dopants on a nanostructured oxide support, this process of catalyst discovery and improvement is slow, expensive, and often of a limited scope. Instead of trying to test every possible real catalyst, the surface science approach is to study model systems in an attempt to gain better fundamental understanding of which factors of a real catalyst play an important role²⁶.

The simplest version of model catalyst is the single crystal catalyst surface. These surfaces possess a single repeated structure consisting of only a few atoms, allowing for precise

determination of what is happening on a molecular scale upon exact surface sites. These studies can provide a tremendous amount of fundamental understanding regarding particular chemical reactions, from the significance of structure to exact energetic and kinetic information regarding reactions on the surface^{2,26}. The value of these discoveries was brought to the public eye with the 2007 Nobel Prize for Gerhard Ertl's work on studying ammonia synthesis on an iron catalyst using surface science techniques.

While many surface science studies have been shown to have value and aid in catalyst design, this fundamental information has a second and perhaps more important role to play. Even with the guiding information provided by surface science studies, the number of potential catalysts to study remains vast. With the advent of rapid computation and the developments of sophisticated molecular simulation software, particularly density functional theory (DFT), theoretical and computational approaches are poised to take the forefront in catalyst design²⁷⁻³³. If accurate and efficient computational methods can be developed it would be possible to screen hundreds or even thousands of potential new catalysts before ever sitting down at the bench.

Work continues on the development of the efficiency and accuracy of current computational tools^{27, 29, 31, 34}, but in order to gauge that accuracy it is necessary to have precise experimental values to compare to. Without an extensive library of information to compare to, it is difficult to say whether a particular computational package is valuable or not. As far as the energetics of catalytic intermediates on surfaces go, this library is currently rather small, limited to a small number of surfaces and adsorbates. It is an ongoing task of our group to try and expand this library of adsorbate energetics.

Typical surface science techniques used to study adsorbate energetics are limited to those compounds which adsorb reversibly to the surface³⁵. Temperature programmed desorption

(TPD) and Langmuir adsorption experiments³⁶ have been used to study the energetics of adsorption of species such as CO, O₂, H₂, N₂, and other simple gases on a variety of different surfaces³⁶⁻³⁸. These techniques cannot directly study any species which adsorbs irreversibly on a surface, such as any species which dissociates upon adsorption or decomposes before desorbing. Unfortunately it is these dissociated species which are the molecular fragments which are so critical to catalysis. Surface bound species such as alkyls, hydroxyls, formate, and alkoxys cannot be studied directly on any surface with these techniques, and instead necessitate the development of kinetic models to interpret the measured data.

While many single crystal catalyst studies are performed on transition metals due to their high catalytic activity for many reactions, metal-oxides also represent an important class of catalysts which are studied. As catalysts metal oxides display unique behavior due to the ionic nature of their surfaces. The presence of adjacent metal and oxygen sites act as acid-base pairs on the surface. At the same time oxides with narrow band gaps can also possess delocalized electrons granting catalytic properties more typically associated with metals^{3,39}. Additionally the presence of oxygen in the surface allows for unique chemical kinetics to occur through the Mars-van-Krevelen mechanism⁴ where the oxygen is removed from the surface temporarily during reaction and replaced at the end of the catalytic cycle. However due to the complexity and difficulty in working with oxide surfaces much work remains to be done to study these systems using surface science.

Single crystal adsorption calorimetry (SCAC) is an ultrahigh vacuum technique developed in the early 1990's by Sir David King⁴⁰. In his original technique an ultrathin single crystal is dosed with a collimated molecular beam of high vapor pressure molecules and the minute temperature change resulting from adsorption on the sample was measured using an

optical pyrometer. This technique allowed for the measure of the heats of adsorption directly on single crystals for the first time. Over the years many improvements were made to this technique, including by our own group which pioneered the use of a pyroelectric polymer ribbon detector⁴¹ to dramatically increase signal to noise, as well as allowing measurements to be performed at cryogenic temperatures. This development was coupled with the use of a molecular beam used for low vapor pressure molecules to dose and measure a wider range of adsorbates⁴². At the core of the technique is the measurement of a minute change in temperature for a laser pulse of known intensity and duration. A molecular beam pulse is then dosed on the surface using the same orifices and pulse duration which were used to shape the laser pulse. Comparing the magnitude of these two responses allows for the extraction of the amount of heat deposited by the molecular beam pulse. More information about this technique and our instrumentation will be provided in Chapter 2.

In this dissertation new work is presented which 1) adds significantly to the small library of measured molecular fragment adsorption energetics on well-defined transition metal surfaces, 2) lays the ground work for studies on well-defined oxide surfaces using SCAC, 3) expands the utility of SCAC with a new data analysis methodology, and 4) develops a new computational catalyst screening tool utilizing adsorption energies obtained from DFT. In Chapter 4, experimental results are presented using SCAC that extend the number of well-defined catalytic intermediates whose energies are known on well-defined transition metal surfaces. Specifically, results are presented for $\text{CH}_{2,\text{ad}}$ and CH_{ad} on Pt(111) which is a model catalyst surface/adsorbate system which occurs in many real world catalytic systems. In Chapter 5, preliminary work studying the adsorption of water and hydroxyls on $\text{Fe}_3\text{O}_4(111)$ and $\text{NiO}(111)$ is presented. No published papers describe SCAC measurements of any molecules or molecular fragments on any

oxide surface, although metal atom adsorption energies have been reported by our group. All of these adsorbate energies on well-defined crystal surfaces are crucial as benchmarks to check the energy accuracy of new DFT techniques that are being developed worldwide to improve energy accuracy. In the course of these studies, we developed a new, direct methodology to analyze SCAC data without any assumption about the kinetic model, which is presented in Chapter 3, and expands the capabilities of SCAC considerably. Previously it was observed that surface reaction/diffusion kinetics occurring on the same time scale as the experimental measurements caused line shape broadening in the heat signal pulse, requiring kinetic modeling to extract meaningful adsorption energies. Finally in Chapter 6, we move to a purely theoretical study where we assume that computational techniques like DFT give “chemical accuracy”, a possibility we see as being close on the horizon and aided by the benchmarking energy measurements mentioned above. We address there how one most efficiently uses computational energetics of catalytic intermediates and transition states to screen materials to find better catalysts. A new method of computational screening is presented which uses the concept of the degree of rate control to define new search ‘descriptors’ that dramatically reduce the number of adsorbates on a potential new catalyst whose energy needs to be calculated in order to predict the catalytic activity on that new material.

Because of the SCAC technique is still fairly new and highly specialized, the technique itself is still being refined. While studying the adsorption of water on Pt(111)⁴³, it was found that the molecular beam heat detector response did not possess the same shape as the laser pulse heat detector response. The cause of this mismatch was found to be caused by the occurrence of a “slow” heat deposition which was occurring on the same timescale as the pulse duration (~100 ms). It was necessary to account for this shape mismatch with a kinetic model in order to extract

quantitative heat data from the experiment. A similar phenomenon was observed for the adsorption of CH_3I on $\text{Pt}(111)$ ⁴⁴ and CHOOH on $\text{Pt}(111)$ ⁴⁵, which was caused by a combination of a fast and slow heat step. This resulted in yet another method⁴⁶ of data analysis for “broadened” molecular beam heat pulses requiring a multistep kinetic model. While studying the adsorption of CH_2I_2 on $\text{Pt}(111)$ (Chapter 4 of this thesis), it was found that the adsorption process resulted in multiple slow steps, and none of the previous methods could be used to analyze the data. A new, universal method of SCAC data analysis was developed which relied on Fast Fourier Transforms (FFTs) to extract the heat signal from the detector response which functions regardless of the complexity of the adsorption process and requires no kinetic model whatsoever. The development of this new data analysis method is discussed in Chapter 3.

Analyzing the work done by our group up to now, a variety studying different intermediates on $\text{Pt}(111)$ produced from water⁴³, methanol⁴⁷, formic acid⁴⁵, and methyl iodide⁴⁸, and more. Chapter 4 of this report will focus on a recent project looking at the adsorption of diiodomethane on $\text{Pt}(111)$. Other work was completed previously by our group studying molecular adsorption of complex organic species on $\text{Pt}(111)$ which decompose during desorption. This work investigated the adsorption of benzene, naphthalene, and cyclohexane⁴⁹. All of this work has provided a tremendous amount of information about different adsorbates on $\text{Pt}(111)$ and has been invaluable to the DFT community as a way of quantifying the accuracy of their simulations. Table 1.1 shows a comparison of different surface species energetics measured by our group compared to numbers calculated by different DFT groups. It can be seen that DFT seems to work well for certain species, but less so for others, and no clear trends in accuracy seem to present themselves. These differences can have a significant impact on the reaction

pathway and kinetics predicted by a model and they show the necessity of continuing to improve DFT.

Once one possesses accurate DFT numbers for a variety of adsorbates and intermediates on a catalyst surface, what can one do with them? Because only one surface has been studied, one cannot use this data to predict a better catalyst. Even if one has data for several surfaces, the trends are often murky and other methods of screening for improved catalysts are necessary. An approach was developed by Nørskov and Bligaard^{28, 31, 34, 50-52} which develops linear scaling relationships between adsorbates in a chemical reaction and a single other chemically adsorbed species. For example, the energy of adsorbed CO scales linearly with the energy of adsorbed C across different metal surfaces. Using this approach, a small number of descriptors (typically C and O binding energies) can be in conjunction with a microkinetic model to construct a volcano plot of catalyst activity for a wide range of metals. This simple approach allows for easy probing of potential new catalysts (such as alloys) by simply finding their descriptors and seeing where they fall on the volcano plot. This approach is not without its flaws however, most notably the scatter which exists in the linear scaling relationships, and the potentially high cost^{30, 31} of using the state of the art, high accuracy DFT to extract meaningful numbers. In Chapter 6 of this thesis a new method of catalyst screening is developed using the concept of degree of rate control^{53, 54} to improve the accuracy of these screening tools and limit the number of high accuracy DFT calculations necessary in computational catalyst screening.

From the improvement of experimental techniques to measure thermodynamic quantities through the development of a universal data analysis methodology (Chapter 3), to an application of that technique to quantify previously unmeasured energetics of catalytically important molecular fragments and the tie between those measurements and the accuracy of DFT (Chapter

4), to the beginnings of measuring heats of adsorption on more complex oxide surfaces (Chapter 5), to the development of a new computational catalyst screening tool to rapidly identify new potential catalysts from a small number of descriptors based on degree of rate control (Chapter 6), taken together these pieces represents a snapshot in the quest to better understand the fundamentals of catalytic processes. Chapter 4 is a prime example of how SCAC and DFT are coupled together, and also represents a further piece in building a library of energies of adsorbates on Pt(111) shown in Table 1.1. The developments of new methodologies for SCAC data analysis and catalyst screening (Chapters 3 and 6) in particular have the potential to be highly referenced and impactful work because of their broadly applicable nature.

Tables

Adsorbates on Pt(111)	Experiment	GGA-PBE	GGA-RPBE	GGA-PW91
	ΔE (kJ/mol)	ΔE (kJ/mol)	ΔE (kJ/mol)	ΔE (kJ/mol)
Methyl	200 ⁴⁸ †	174, 192 ⁵⁵	163 ^{33 a}	197 ³³
tert-butyl	216 ⁵⁶ †	125		
Methane	15.2 ⁵⁷ *	1.2	-3 ⁵⁸	3.8 ^{59 a}
Propane	41.5 ⁵⁷ *	6.3, 6 ⁵⁵	0 ^{60 b}	
Propane	41.5 ⁵⁷ *	6.3 ^a	-9 ^{60 a}	
Benzene	166 ⁶¹	78.6, 78 ⁶²		67.5 ⁶³ , 86.8 ⁶⁴ , 117 ⁶⁵
Methylidyne	561.5 ⁴⁴	630, 643 ⁵⁵	569 ^{33 a}	620 ³³
OH within (H ₂ O-OH)complex	248 ^{66 d}	262	217 ^{66 d}	
Methanol	59.4 ^{47 e}	24 ^{67 e §}		
Methanol	59 ^{47 a}	72.4 ^{68 a}		31.8 ^{69, 70} , 20 ⁷¹
Methoxy	186 ^{47 a}	204 ⁶⁸	95	161 ^{72 a}
Water hexagonal network	51.3 ^{66 f}	38.7	30 ^{66 f}	
Formate (monodentate w/ OH _{ad})	222 ^{73 a}	151 ^{74 a}		
Formate (bidentate w/ H ₂ O _{ad})	257 ^{73 a}	241 ^{74 a}	159 ^{75 a}	223 ⁷⁵
O	348 ^{66 a*}	384	352 ^{66 a}	360 ⁷⁵ , 389 ⁷⁶
CO	116 ^{77, 78 a}	160 ^{74 a}	129 ^{79 a}	176 ⁷⁵

Table 1.1. Comparison of previously measured adsorbate energies for species measured by SCAC on Pt(111) with those calculated by different DFT methods. (Prepared by Trent Silbaugh⁸⁰)

All coverages are 1/9 ML unless otherwise noted

All experimental data from SCAC unless otherwise noted

* Temperature programmed desorption data

† coverage of 1/20 ML coadsorbed with 1/20 ML atomic iodine

§ adsorbed on H₂O-sat. Pt(111)

^a coverage of 1/4 ML

^b coverage of 1/8 ML

^c coverage of 1/16 ML

^d coverage of 1/3 ML

^e coverage of 1/37 ML

^f coverage of 2/3 ML

Experimental data entries without citations are in manuscripts under preparation

GGA-PBE DFT calculations without citations performed by Ye Xu (currently unpublished)

Chapter 2: Instrumentation

Single crystal adsorption calorimetry (SCAC) is an ultrahigh vacuum (UHV) surface science technique. All of the experiments performed or proposed in this work have been or will be using a custom built instrument which is discussed in exhaustive detail in a 2004 article in *Review of Scientific Instruments*⁴². In this section I will briefly discuss the instrument as well as the single crystal adsorption technique.

Briefly, a pulsed molecular beam strikes the surface of a thin single crystal. The resulting surface reaction is exothermic and thus creates a transient temperature rise in the single crystal with each pulse of the beam. This transient temperature rise is monitored with a heat detector, whose response is calibrated using pulses of known heat.

The SCAC is part of a UHV system with base pressure $<2 \times 10^{-10}$ mbar which contains two levels. The lower ‘calorimetry’ level, photographed in Figure 2.1, houses the calorimeter itself as well as all of the components necessary for SCAC experiments including a collimated pulsed molecular beam, a quartz crystal micro balance (QCM), a quadruple mass spectrometer (QMS), and a gold flag. The upper ‘surface analysis’ level, not shown in Figure 2.1, contains a variety of classic surface science analytical tools including Auger Electron Spectroscopy (AES), X-Ray Photoelectron Spectroscopy (XPS), Low Energy Ion Scattering (LEIS), and Low Energy Electron Diffraction (LEED), which are used together to check the cleanliness, composition, and order of the surface. Additionally the upper level includes a metal evaporation source used to deposit material for thin film growth like the Fe_3O_4 films discussed in Chapter 5.

The calorimeter’s heat detector itself is made from a 4mm wide, 9 μm thick metal-coated pyroelectric polymer ribbon made of β -polyvinylidene fluoride (PVDF)⁸¹. This ribbon is held as an arch and is driven into contact with the back surface of the single crystal. The single crystals

are 1 μm thick and about 1 cm in diameter, and were prepared by Jacques Chevalier at Aarhus University in Denmark. The ribbon and sample are capable of being cooled by a liquid nitrogen cryostat down to temperatures of ~ 100 K. The molecule of interest is dosed onto the surface using the pulsed molecular beam (~ 102 ms per pulse, one pulse every 5 seconds), whose flux is measured using a liquid nitrogen cooled QCM. In the molecular beam a constant backing pressure of gas is collimated through a heated glass capillary array (GCA). The beam is then shaped by passing through five liquid nitrogen cooled orifices to produce a spot 4.36mm in diameter on the sample. With each molecular pulse heat is deposited on the surface resulting in a miniscule temperature change which causes a transient voltage rise across the pyroelectric ribbon. Simultaneous to the heat measurements being made using the calorimeter, the sticking fraction is measured using the King-Wells non-line of sight method⁸². In brief, this method uses a non-line of sight QMS to observe a rise in the chamber background pressure of the molecule being dosed. This is then calibrated using a gold zero sticking flag, which in our experiments is a room temperature gold flag to determine the sticking fraction. The sticking fraction is divided into two parts, the short term sticking which is the fraction of molecules that desorb during the 102ms pulse, and the long term sticking which takes into account the number of molecules that desorb in the entire 5 second pulse window. An illustration of how this is performed is shown in Figure 2.2. The short term sticking impacts the measured heat of adsorption while the long term sticking determines the total coverage on the surface. Finally, a laser pulse from a HeNe (632.8nm) laser of known intensity and duration is then shone through the same orifices in the molecular beam on to the surface, whose reflectivity is known, and a similar transient voltage rise is observed in the calorimeter signal. Comparing the magnitude and shape of the molecular beam and laser calorimeter responses as is shown in Figure 2.3 allows for the calculation of the

heat deposited by each molecular beam pulse. Combining this information along with the sticking fraction and measured beam flux allows the extraction of the differential heat of adsorption as a function of coverage. Additionally if dissociation occurs on the same timescale as the heat measurement, it is possible to extract kinetic information for the surface adsorption and reaction⁴⁶

The number of SCAC apparatus currently in operation is quite small. Each SCAC instrument has been specialized to a great degree to probe a specific kind of adsorption system with recent systems being developed to study ultra-low vapor pressure metals⁸³, gas adsorption on nanoparticles⁸⁴, and electrochemical systems⁸⁵. Though the SCAC instrument discussed in this report was the third SCAC apparatus built; it has been one of the most prolific, resulting in a vast number of papers during the first decade of its operation due largely to the tremendous variety of adsorbates it is able to utilize. Future work on this instrument will likely continue by expanding the list of adsorbate/surface systems it studies beyond Pt(111) to include other metals and metal-oxides it is likely this instrument can continue to be just as productive going forward.

Figures

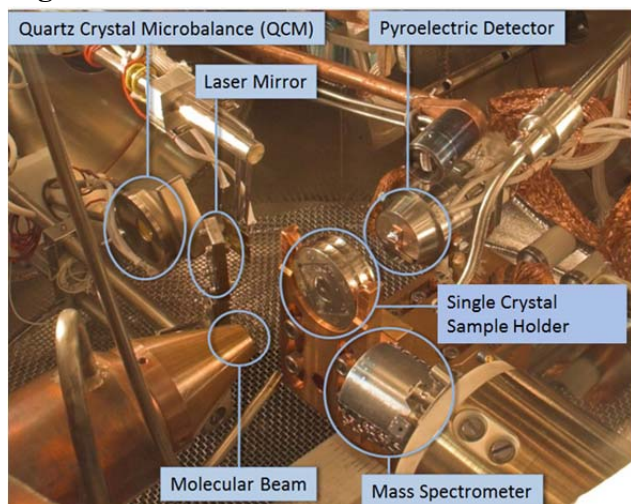


Figure 2.1. Photograph of the interior of the SCAC instrument described in this chapter. Each element is labeled as corresponds to those used in text.

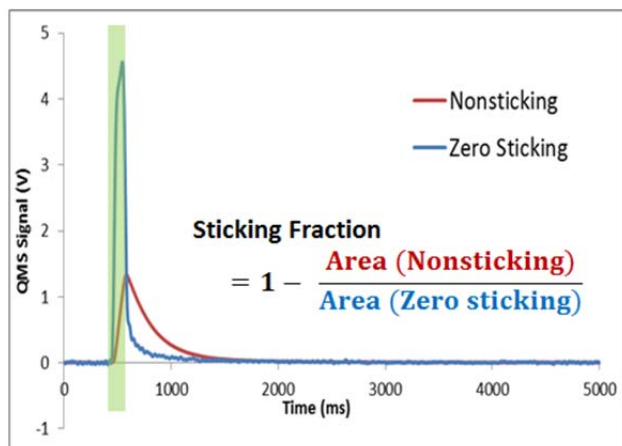


Figure 2.2. Quadrupole mass spectrometer response for zero sticking pulse on Au flag (blue) and a the non-sticking fraction of an experimental pulse (red). Shaded area is 100ms pulse window used to differentiate short and long term sticking. Comparing the areas of the shaded region between the Nonsticking and zero sticking fractions allows the calculation of the fraction of molecules sticking to the surface during the timescale of the heat measurement. Because some molecules may also desorb slowly, it is necessary to calculate the “long term” sticking fraction, which determines the total coverage of molecules on the surface. This is accomplished by comparing the areas of the two peaks across the entire pulse window.

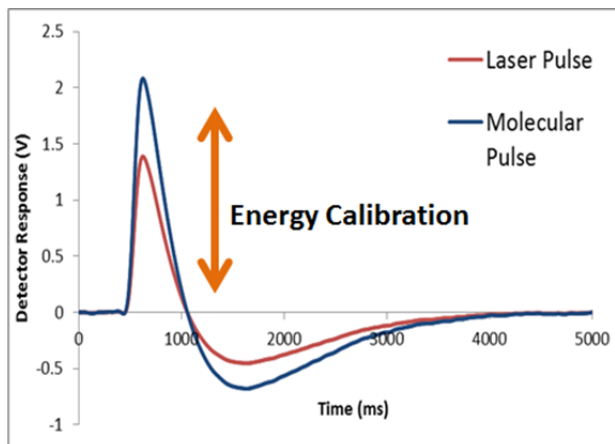


Figure 2.3. Pyroelectric heat detector response for laser pulse and molecular pulse. In the simplest case (shown here), without and slow heat deposition step, the energy of the molecular beam pulse can be determined by scaling the energy in the laser pulse so that the two curves match. If a slow heat deposition step occurs, the molecular pulse appears broadened relative to the laser, and a more complicated analysis is needed to extract heat data (see Chapter 3).

Chapter 3: Method for Direct Deconvolution of Heat Signals in Transient Adsorption Calorimetry

This chapter is reprinted with permission from: C.A. Wolcott, C.T. Campbell, Method for direct deconvolution of heat signals in transient adsorption calorimetry, Surf. Sci. (2014), <http://dx.doi.org/10.1016/j.susc.2014.11.005>

Chapter Abstract

A method of heat signal analysis is presented for transient adsorption calorimetries including single crystal adsorption calorimetry (SCAC) which uses fast Fourier transforms (FFT) to determine the instrument response function and deconvolute the heat-versus-time signals. The method utilizes a heat signal generated by a laser pulse of known power-versus-time to extract the instrument response function for the calorimeter. The instrument response function is then used to extract the heat power signal from a molecular beam heat pulse of unknown intensity. This method allows for the extraction of the total heat deposited by the molecular beam pulse without any kinetic modeling even in the event of complex reaction dynamics. This method is compared to previous methods used to analyze SCAC data using example data from the two-step dissociative adsorption of methyl iodide on Pt(111). It is found to be equally accurate for extracting total heats and simpler to perform than the previous methods.

Introduction

The measurement of reaction enthalpies for elementary steps occurring on solid surfaces is crucial for fundamental understanding in heterogeneous catalysis and many other technologies. Few techniques exist to measure these quantities directly, especially on single crystal surfaces which allow for the adsorbed species to be fully characterized using a variety of surface science techniques and computationally modelled using state-of-the-art density function theory (DFT)

with periodic boundary conditions. Typical techniques used to extract reaction enthalpies for surface processes are indirect, such as temperature programmed desorption (TPD) and equilibrium adsorption experiments (typically performed in either isobaric or isothermal conditions). These techniques require that a process be reversible to extract thermodynamic information such as the heat of adsorption for a particular surface species³⁵. Since many surface processes of interest, especially in heterogeneous catalysis are irreversible processes such as dissociative or reactive adsorption, these techniques cannot be used to probe many important species. Though some qualitative information about the stability of molecular fragments can be gained through very clever application of these classic techniques such as the work of Friend et al.⁸⁶ looking at competitive adsorption of different species on a surface, quantitative information remains largely unattainable. Common surface processes such as dissociative adsorption or other surface reactions require a different technique in order to extract quantitative thermodynamic information about adsorbed species.

Single crystal adsorption calorimetry was developed to study the energetics of adsorption on single crystal surfaces directly⁸⁷. It does not require that a process be reversible, nor that a kinetic model be developed to extract the heats of adsorption in most cases. A tremendously wide range of adsorbates have been studied using this technique, from simple gases⁸⁸ like CO, NO, O₂, and C₂H₄, to larger, low vapor pressure molecules like benzene⁶¹, naphthalene⁸⁹, cyclohexene⁹⁰, water^{43, 91, 92}, methanol⁴⁷, formic acid⁴⁵, methyl iodide^{44, 48}, t-butyl iodide⁹³, and diiodomethane⁹⁴, and even to metals like Ca⁹⁵, Li^{95, 96}, Pb⁹⁷⁻⁹⁹, Ag^{100, 101}, and Cu¹⁰². The same general type of technique that works on single crystals and is known as SCAC also works on many other types of planar surfaces, and has recently been applied to CO adsorption on oxide supported metal nanoparticles¹⁰³, metal adsorption on spin-coated polymers^{104, 105} and even to

electrochemical systems^{106, 107} with a solid-liquid interface. For the purposes of this present paper, we describe these more generally as “transient adsorption microcalorimetry”, and the signal analysis techniques we describe below apply to all such methods. In many of these systems, the heat that is generated upon adsorption is transferred nearly instantaneously to the calorimeter’s heat detector, allowing a simple calibration to a known heat signal to be used to extract the adsorption heat of the unknown process. In these cases, simply scaling the calibration signal until it matches the unknown signal exactly lets one determine the amount of energy in the unknown signal. We address here what happens when the heat deposition instead is not instantaneous, and occurs with some time delay on the same millisecond time scale as the heat measurement, due to slower surface reaction kinetics.

This phenomena of a non-instantaneous or “slow” heat deposition was first reported by Lew et al.⁴³, who observed that the calorimeter signal seen for the adsorption of D₂O on a Pt(111) surface did not possess the same normalized lineshape as the calibration signal generated with a laser pulse (which deposits its heat to the sample’s surface instantaneously). The heat signal pulse appeared to be “broadened” relative to the laser signal, possessing a larger full width at half max (FWHM). The mismatch was very slight, with only a 6% mismatch between the FWHM of the measured heat signal and the laser calibration signal. By convoluting the measured laser calibration signal with an exponential decay function with a time constant of ~30ms, they were able to produce an identical signal to the heat signal measured, suggesting the heat of adsorption was produced by a single slow process which had a characteristic time constant equal to ~30ms. This slow heat process was attributed to adsorption and relaxation of the adsorbed D₂O molecules into their most stable packing arrangement on the Pt(111) surface.

This slow heat deposition phenomenon was observed again for the adsorption of methyl iodide on a Pt(111) surface⁴⁴. In this instance the heat of adsorption could not be fit using the convolution method of Lew et al., suggesting that the process was more complex than a single slow process. A new method was developed by Silbaugh et al.⁴⁶, which modelled the adsorption process as a single instantaneous “fast” step followed by a slower step modelled by convoluting the laser signal with an exponential decay function as was done in the method of Lew et al.. The sum of the signals from these “fast” and “slow” steps could then reproduce the measured signal. This method had three variables to fit, the heat of the fast step, the heat of the slow step, and the time constant for the slow step time decay function. When appropriately fit, this method produced a unique solution which yielded not only the heats of both the initial fast step and second slow step, but also for the first-order rate constant for the slow reaction (i.e., the inverse of the time constant obtained from the fit). This powerful method, while labor intensive as it requires fitting three parameters for each pulse’s lineshape (or an average lineshape from a small number of pulses), yields a wealth of information on adsorption energetics and dynamics. In addition to being used for methyl iodide adsorption on Pt(111) to yield information about the heat of adsorption of CH₃I, CH₃, and the dynamics of the reaction CH₃I_{ad} → CH_{3,ad} + I_{ad}, this method has also been used to study the adsorption of formic acid on Pt(111)⁴⁵, yielding information about the energetics of molecular formic acid, monodentate and bidentate formate, and kinetic information about the reactions HCOOH_{ad} + O_{ad} → HCOO_{ad,mono} + OH_{ad} and HCOO_{ad,mono} → HCHOO_{ad,bi}. Both of these methods present valuable and highly functional techniques for analyzing simple adsorption-relaxation and adsorption-reaction processes. Through the development of a mechanistic and kinetic model, they allow the extraction of both thermodynamic and kinetic information in whatever system they are applied. They each

however, have their limitations. The key limitation is that they only work for the precise processes they model, i.e. a single slow step or a combination of a single fast step followed by a single slow step. While in theory the method of Silbaugh et al. could be expanded to include any number of fast and slow steps occurring either in series or parallel, this rapidly becomes infeasible as the number of parameters which are necessary to fit increases, making it more labor intensive and at the same time harder to show the uniqueness of a solution. As a result a new method is needed to analyze any reaction with more complex surface reaction dynamics than those modelled by Lew and Silbaugh.

This paper presents a more general method for analysis of transient adsorption calorimetry data which requires no kinetic modelling or parameter fitting even in the event of signal broadening. This new method utilizes FFTs to extract heat data directly from the calorimeter signal without any scaling or kinetic parameters. This method successfully yields the total heat deposited on the surface regardless of any signal broadening. This method possesses universal applicability and a complete absence of fitting parameters or requirements for pulse averaging give it many distinct advantages. This technique is demonstrated here by applying it to study the heat of adsorption of diiodomethane on Pt(111), whose adsorption, reaction, and diffusion dynamics were sufficiently complex that they could not be modelled using the method of Silbaugh et al.. A more extensive presentation of the results of this application is presented elsewhere⁹⁴.

Signal Generation and Pulse Shape

We describe here the technique in association with SCAC, although the same principles could be applied to any transient adsorption calorimetry. For the purposes of clarity, a brief explanation of the SCAC technique itself will be given first. The explanation given here is for

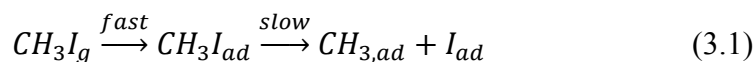
ultrahigh vacuum (UHV) gas / solid interactions, which is the most common form of SCAC. For full details of this version of SCAC, see Ajo et al.⁴² For details of the electrochemical version of SCAC, see Schuster et al..⁸⁵

SCAC is typically performed in a stainless steel UHV chamber (base pressure $< 2 \times 10^{-10}$ mbar). Other surface science techniques such as Auger electron spectroscopy (AES), low energy ion scattering (LEIS), low-energy electron diffraction (LEED), and x-ray photoelectron spectroscopy (XPS) are used to verify sample cleanliness and order. A very thin (typically $1 \mu\text{m}$) single crystal is used as the sample, to minimize thermal mass while maintaining structural stability. A heat detector, typically a pyroelectric polymer ribbon made of β -polyvinylidene fluoride (β -PVDF), is driven into gentle contact with the back of the sample, and is then used to measure minute temperature changes in the sample upon heat adsorption, which are recorded as a transient voltage signal after preamplification and further amplification and electronic signal filtering. This gives rise to the observed instrument response lineshape, as discussed previously^{46, 108}. The heat detector is calibrated using a laser pulse whose intensity is measured using a photodiode. Molecules are dosed using a molecular beam and the sticking fraction of molecules is measured using the King-Wells method⁸². The duration of a pulse, either laser or molecular, is controlled by chopping the beam with the same mechanical chopper. The flux of molecules is measured using a liquid nitrogen cooled quartz crystal microbalance (QCM). Each pulse of molecules or laser is typically around 100 ms long. The output from the detector is recorded as a voltage signal as a function of time shown, such as in the top of Fig. 3.1.

If the heat deposition from the molecular beam pulse occurs rapidly (< 10 ms) the resulting detector signal will have the identical shape as the laser pulse (which also deposits heat extremely rapidly). By simply scaling the molecular beam pulse to match the magnitude of the

laser pulse, whose intensity is known, the amount of heat deposited by the molecular beam pulse can be found.

If the heat deposition is on the same timescale as the pulse duration (~10 ms – 1000 ms) then the molecular beam pulse appears broadened, as shown in Fig. 3.1. This figure shows a superposition of the laser calibration response and the heat deposition of CH₂I₂ on Pt(111) at 125K. In this case, a more complex analysis is necessary. The approach depends on what the expected reaction dynamics are. If the reaction is simple, consisting of two or fewer steps, then the method of Silbaugh et al.⁴⁶ can be used. An example of a two-step process where this occurs is shown in Eq. 3.1.



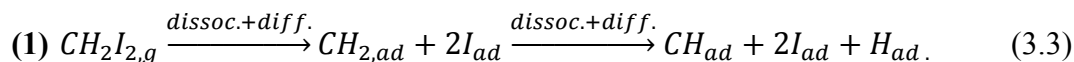
A model is generated consisting of the sum of scaled laser pulse and another scaled laser pulse which has been convoluted with an exponential decay function shown in Eq. 3.2.

$$D = 1/\tau e^{-t/\tau} \quad (3.2)$$

The scaling factors of each of the pulses and the time constant in the exponential decay function are varied until the sum of the two pulses matches the measured pulse. The method of Lew et al. discussed in the Introduction can be seen as identical to the method of Silbaugh et al. if the instantaneous heat is zero. If there is a heat deposition process which occurs with a time constant slower than the time between pulses, it is not measurable using SCAC and will appear as if it is not occurring, since it contributes only to an increase in the background. In practice, even processes that occur with a time constant longer than 1/5 of this (i.e., > 1 s) are difficult to see about the background noise, since such extreme broadening decreases pulse amplitude too much.

If the adsorption process has more than one step with a rate constant on the same order as the pulse duration, then in theory it could be fit using the method of Silbaugh et al.. This approach of convoluting multiple contributions to try to fit the signal rapidly becomes unfeasible, however, as more variables are added along with the possibility of each additional step occurring either in series or in parallel with other steps. In addition to being extremely labor intensive, one should be skeptical of the uniqueness of any solution found when very many variables are needed to fit the data.

This scenario of multiple slow steps was encountered when studying the energetics of diiodomethane on Pt(111). The dissociation of diiodomethane (Eq. 3.3) on Pt(111) to produce CH_{ad} , $2I_{ad}$, and H_{ad} is expected at temperatures as low as 130K¹⁰⁹.



This process involved the breaking of two C-I bonds, one C-H bond, as well as surface diffusion of strongly bound surface species such as I_{ad} and $CH_{x,ad}$. If any two or more of these processes are slow, then the data cannot be analyzed using the method of Silbaugh et al.. Attempts were made using the two step method Silbaugh et al. to fit the data, but the complete reaction dynamics could not be captured (as evidenced by a poor fit of the models to the data). Attempts were made to modify the method of Silbaugh to include a third step either in series or in parallel and even this did not seem to capture the complete reaction dynamics (again evidenced by a poor fit). To extract meaningful heats out of the signals, a different approach was necessary.

Direct heat extraction using FFT

The shape of the detector response signal, $S(t)$, results from the convolution of a heat input ($I(t)$) with an instrument response function ($R(t-t')$):

$$S(t) = (I * R)(t) = \int_{-\infty}^{\infty} I(t')R(t - t')dt' \quad (3.4)$$

For the heat detector used in this paper the functions, $S(t)$, $I(t)$, and $R(t)$ are shown graphically in Fig. 3.2. If the heat input is known for any given measured detector response signal, it is possible to use deconvolution via FFT to extract the instrument response function from the measured detector response signal. This is done by first taking the a discrete Fourier transform of the measured signal, $F[S(t)]$, which allows the convolution to be split into the product of two separate Fourier transforms, as a direct mathematical consequence of Eq. (3.4) above:

$$F\{S(t)\} = F\{(I * R)(t)\} = F\{I(t)\}F\{R(t)\} \quad (3.5)$$

Equation (3.5) is only true when the detector response is linear. One should always test the calorimeter response during calibration with different laser powers to ensure that the signal magnitude scales linearly with laser power and the lineshape is independent of power, as described previously^{41, 108}. Simple mathematical rearrangements, followed by an inverse Fourier Transform, then provides a direct solution for the instrument response function via:

$$R(t) = F^{-1}\{F\{S(t)\}/F\{I(t)\}\}(t), \quad (3.6)$$

where $F^{-1}[X]$ represents the inverse Fourier Transform of X .

Similarly if the instrument response function is known for any given measured detector response signal but the heat input is unknown, the heat input can be found using an identical method only solving for $I(t)$ instead of $R(t)$:

$$I(t) = F^{-1}\{F\{S(t)\}/F\{R(t)\}\}, \quad (3.7)$$

During laser calibration of the calorimeter, the magnitude of the heat input from the laser pulses is measured with a photodiode and properly scaled to correct for imperfect transmittance through a window on the UHV chamber (which separates the photodiode from the sample). The pulse width of both the laser and the molecular beam is set by adjusting the speed of the chopper in the molecular beam line. The laser pulse lineshape is trapezoidal and can be calculated exactly from the known geometry of the chopper blade. However, it is closely approximated by a square wave as shown in Fig. 3.2. This square wave “model” of the laser heat input was then used to extract the instrument response function from the detector response to the laser pulse (as shown in Fig. 3.2) using the mathematical procedure described above. We also used the true trapezoidal lineshape of the laser pulse, and found this to produce results that were indistinguishable from the approximate square-wave lineshape, so we use this simpler square-wave model in the results below.

All calculations and FFTs were performed in Wolfram Mathematica 9.0 using its built-in functions. Once the instrument response function had been found, the same analysis can be done using the detector response signal for the molecular beam pulses, only solving for the heat input instead. An example result showing one heat input for a pulse of CH_2I_2 adsorbed on Pt(111) at 125K is shown in Fig. 3.3. Superimposed on Fig. 3.3 is the laser power model square wave used to extract the instrument response function from the average of 50 laser pulse signals, and an individual laser pulse heat input which was deconvoluted using that instrument response function. Immediately, it is clear that the heat input of the molecular beam pulse is broadened to longer times compared to the laser pulse heat input. Additionally it can be seen in Fig. 3.3 that there is a periodic baseline noise in the deconvoluted signal, which is an unavoidable mathematical artefact of the deconvolution procedure. The deconvoluted heat signal presented in

Fig. 3.3 has already been low-pass filtered and further filtering to attempt to remove the periodic noise which remains resulted in a change in the shape and magnitude of the signal. No apodization functions were used in this FFT, although it is possible they would clean the signal even more.

It is obvious that integrating the heat input obtained in Fig. 3.3 would yield the adsorption energy for that pulse. Integrating across the entire five-second pulse period would be the ideal integration window for this. However, the baseline noise present in the deconvoluted signal contributes to noise in this time-integrated heat, and the magnitude of that noise contribution grows with increasing integration time, as shown below. The best integration window depends on the time duration of the actual heat input, which varies with the reaction being studied and surface temperature. In general, heat deposition for first-order processes shows as an exponential time decay with some characteristic time constant, τ . The limits of the integration window can then be understood in terms of the fraction of heat captured at specific times after the pulse center. By integrating out to 1τ , 63% of the heat is captured, 2τ yields 86%, and 3τ yields 95%, and so on, increasing as the integral of Eqn. 3.2. Alternatively, for any fixed time window, we can calculate the largest τ for which we capture 95% of the heat. In our example we chose a start time ~ 200 ms before the middle of the molecular beam pulse (which is 102 ms long) and a stop time ~ 500 ms after that. This means we miss any heat deposited slower than ~ 500 ms, and means we get $>95\%$ of the heat for any reactions that happen with $\tau < \sim 170$ ms. Further discussion of the method for intelligent selection of the integration window is discussed below with numerical examples. By measuring the amount of molecules sticking in the pulse using the same methods typically used in SCAC,⁴² the heat of adsorption in kJ per mole adsorbed can be found from the time-integrated heat for each pulse.

Since the limited data range used for the Fourier transform deconvolution introduces periodic oscillations in the deconvoluted heat input, one should also fine-tune the integration start- and stop-times to fall halfway between the minima and maxima of these noise oscillations to avoid systematic error. It is easy to identify the periodicity and time locations of these minima and maxima by averaging multiple curves like Fig. 3.3. To assess the significance of this potential source of error, we stepped through the period of oscillation in $\frac{1}{4}$ increments on both ends of the integration window. The resulting heat vs. coverage plots are shown in Fig. 3.4. These heats are averaged across four sets of data collected upon the adsorption of CH_2I_2 on Pt(111) at 125K. The result shows that there is no systematic offset at almost all coverages produced by changing the integration windows in this way (Fig. 3.4a), showing that the periodic noise does not contribute significantly to the averaged or integral heat of adsorption. However, there is a systematic increase in the heats at very low coverage when the end point of integration is increased (Fig. 3.4b). These low-coverage pulses were the most broadened by contributions from the slow process, and this systematic increase is due to capturing more and more of this slowly deposited heat. This result highlights the problem with picking a window that is too short, and thus not capturing all of the heat input when a significant part of it occurs in a reaction step with a long time constant, as it does at very low coverages here.

Several different end points for integration were tested using the same raw sets of data as in Fig. 3.4 and are shown in Fig. 3.5. It can be seen that although the noise present in the data increases with increasing the size of the window, integrating beyond 1000 ms no longer changes the magnitude of the low-coverage heats as it did up to 750 ms (Fig. 3.4). By inspection of the raw pulse shapes, we found that the largest noise spikes in Fig. 3.5 all come from a few isolated spikes in the baseline signal which are picked up at large integration times but not at short times.

Figure 3.6 shows the pulse-to-pulse standard deviation of the heat in the coverage range 0.2-0.4 ML in Fig. 3.5 (where the heat is relatively constant) plotted versus the width of the integration window. As seen, the noise increases nearly proportional to the width of the integration window. Thus, to minimize noise, one should choose the shortest window that captures all of the heat, which unfortunately gets longer the slower the reaction rate for the heat deposition reactions being studied.

Returning to Fig. 3.4 in light of Fig. 3.6, it can be seen that the additional noise introduced by increasing the integration window from 300 to 400 ms there increased the standard deviation only by about ~ 10 kJ/mol, a very small amount compared to the magnitude of the heat signals measured.

Striking the right balance between collecting as much slow heat deposition as possible in the integration window and minimizing the noise in the data is important in the use of this method. The appropriate selection of the end points of integration is clearly very important, and it must be carefully selected when using this technique. Since it depends on the time duration of heat input, which varies with the reaction kinetics, it will depend sensitively on both the reaction being studied and surface temperature.

Comparison of Results to Method of Silbaugh

To showcase the functionality of this new method, we reanalyzed a set of raw data which had been previously analyzed using the method of Silbaugh et al.^{44,46}. The experiment consists of the measured heat of dissociative adsorption for CH_3I on Pt(111) at 270 K. A plot showing both the method of Silbaugh and the method of this paper are shown in Fig. 3.7. The heat plotted here is the total heat from Silbaugh, which is the sum of the slow and fast step heats from Eq.

3.1. In the method of Silbaugh, sets of four pulses were averaged in order to produce clean enough data to fit with that method. This averaging of multiple pulses was not necessary for the method of this paper, which can extract heat for every pulse individually. The two methods can be seen to yield nearly identical heat-versus-coverage plots when both are fitted to straight lines, as shown. Each point from Silbaugh's method should nearly equal the average of the four adjacent points around it using the method of this paper. This is indeed found to be the case, with an average difference of 6.5 ± 11.8 kJ/mol (95% confidence) between the two sets of data when compared in that way. This can be compared to the 1.7 kJ/mol pulse-to-pulse standard deviation of this particular SCAC instrument at similar conditions but when the data pulses show no broadening and can be quantified by simply comparing pulse amplitude to the laser calibration⁸¹.

One advantage of this FFT technique over the method of Silbaugh can be readily seen in Fig. 3.7 by the point at ~ 0.009 ML coverage, highlighted with a green arrow. Because the method of Silbaugh required the averaging of four pulses to get a clean enough lineshape to model, outlying points can be incorporated into that average without the knowledge of the person analyzing the data. That is not the case with this new method, and that highlighted point can easily be identified as an outlier, as shown here. Upon looking through the raw pulse lineshape for this pulse, it was found that this point was the result of a baseline noise spike.

The method of Silbaugh et al.⁴⁶ also allows for the extraction of kinetic parameters as well as thermodynamic heats of adsorption. The details of this methodology are discussed briefly in the Introduction above, and in detail in that paper. Two attempts were made to extract kinetic information in the same vein as the method of Silbaugh et al but instead using the FFT deconvoluted heat pulse lineshape. The first approach was to simply fit the tail of the deconvoluted heat pulse with an exponential of the form of Eq. 3.2. Attempting to fit the same

data of Silbaugh et al. but instead using this method resulted in fit parameters that were similar in magnitude to those reported by Silbaugh. However, it was found that even minor variations in the starting point of the fit would result in changes in the time constant by 50% or more. A method for properly determining the correct starting point could not be found, due to the small magnitude of the slow heat signal compared to the noise present in the deconvoluted signal.

To demonstrate that kinetic information can be obtained in principle by this FFT method when the signal / noise ratio is good enough, we simulated a nearly noiseless heat signal lineshape that would be expected in the absence of noise due to the heat of adsorption followed by dissociation for CH₃I on Pt(111), as shown in Fig. 3.8. At the conditions modelled here, Silbaugh et al.⁴⁶ showed that CH₃I first adsorbs molecularly with a heat of 184 kJ/mol and then dissociates via a first-order reaction with time constant $\tau = 170$ ms and heat of 64 kJ/mol. Curve (a) at the bottom shows the reaction heat input to the sample versus time for this two-step process. The curve at the top shows the signal waveform simulated for this same heat input model generated using the simulation method of Silbaugh et al.⁴⁶, which sums heat-scaled waveforms for its two steps. This simulation uses the nearly noiseless measured response to laser heating (averaged over many pulses) for the first, fast step and its convolution with first-order kinetics for the slow step. Curve (b) at the bottom shows the heat input versus time obtained by deconvolution of this nearly noiseless signal to remove the instrument response function using the FFT method of this paper. As seen, curves (a) and (b) agree very closely, except for the damped periodic noise in (b). It is clear that one could model this red curve with the sum of the blue and green curves to extract values for the two separate heat contributions and the time constant for the exponentially decaying tail, although somewhat different values would be obtained due to the small amount of noise present even in this heat-versus-time curve.

Conclusions

A universal method is demonstrated to analyze transient adsorption calorimetry data regardless of reaction dynamics on the surface. Traditional methods^{42, 43, 46} require that the heat of adsorption consist of either a single fast step, a single slow step, or a combination of a single fast and a single slow step in order to extract thermodynamic information. In the event of the presence of a slow step, these other methods require fitting the measured heat data with a mechanistic and kinetic model to obtain any heat information, something this new universal method does not require. In addition to being less labor intensive than these other methods, this new technique allows for the extraction of the total adsorbed heat from even extremely complex adsorption-reaction-diffusion-relaxation systems.

This new data analysis method has been applied to the study of the adsorption of diiodomethane on Pt(111), providing coverage dependent heats of adsorption for this system at temperatures ranging from 100 K to 210K⁹⁴. The complex, many-step dynamics of this system made it impossible to analyze using any of the previous methods, showcasing the unique power of this new method. The method has also been used to reanalyze and compare with data from Silbaugh et al.⁴⁶, showing that both of the methods yield the same total heat of adsorption for a process consisting of a single fast and a single slow step.

Figures

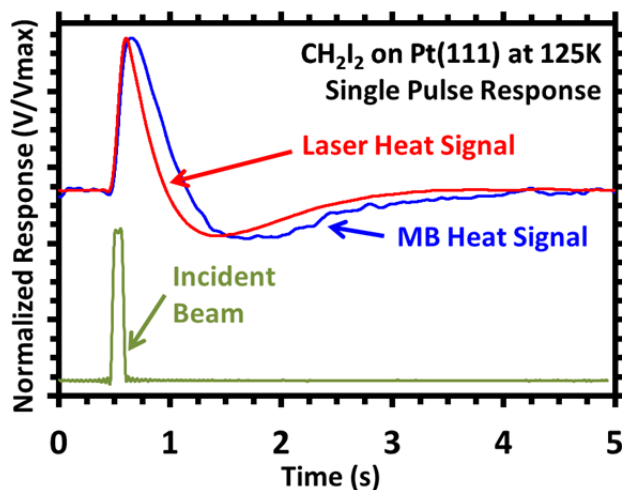


Figure 3.1. Comparison of typical normalized response signals measured for single pulses of the laser beam and the molecular beam (MB), for a case where the latter shows peak broadening due to slow kinetics. Also shown is the incident beam profile, which is approximately a square wave. This profile is essentially identical for both the laser and the molecular beams, and its shape is determined by the diameter of the beam, the geometry of the chopper wheel and its rotational velocity. The incident beam profile shown here was collected by measuring the direct molecular beam intensity with a quadrupole mass spectrometer (QMS).

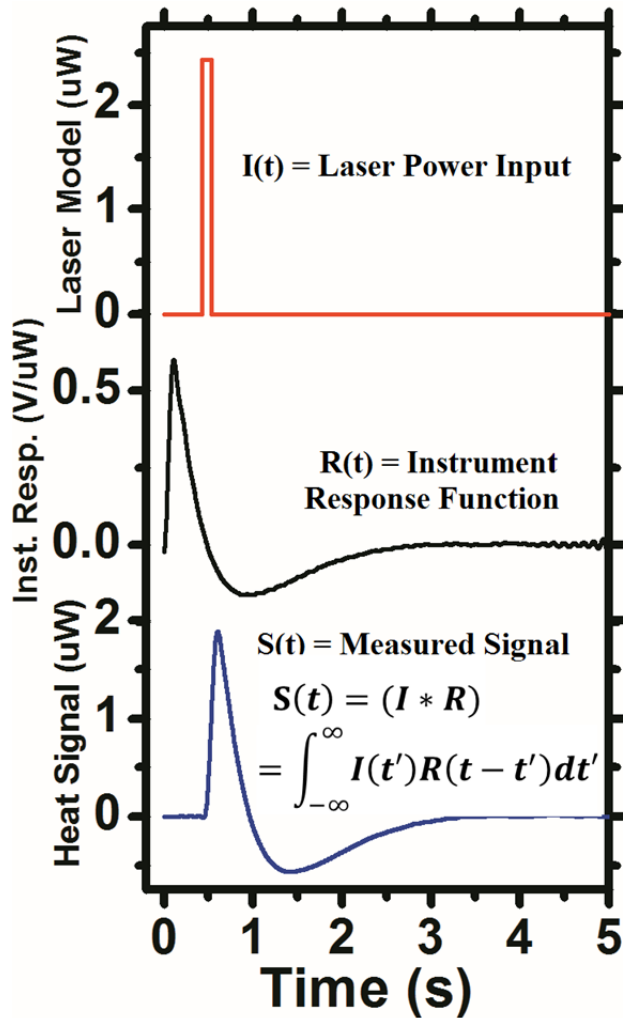


Figure 3.2. A typical heat deposition profile ($I(t)$, here a square-wave model of the incident laser power) is convoluted with the instrument response function ($R(t)$) to yield the measured detector signal ($S(t)$). Here, $R(t)$ was actually calculated by deconvolution of the known $I(t)$ from the measured $S(t)$, as detailed in the text. Because the instrument response is partially determined by the quality of the physical contact between the heat detector and the sample, it is necessary to extract the instrument response function every time a new contact is established (once for each heat-versus-coverage run). The laser power input function is modelled here as a square wave. It was also modelled as a trapezoidal wave based on the known open/close profile of the chopper in this system, which produced an identical instrument response function (see text).

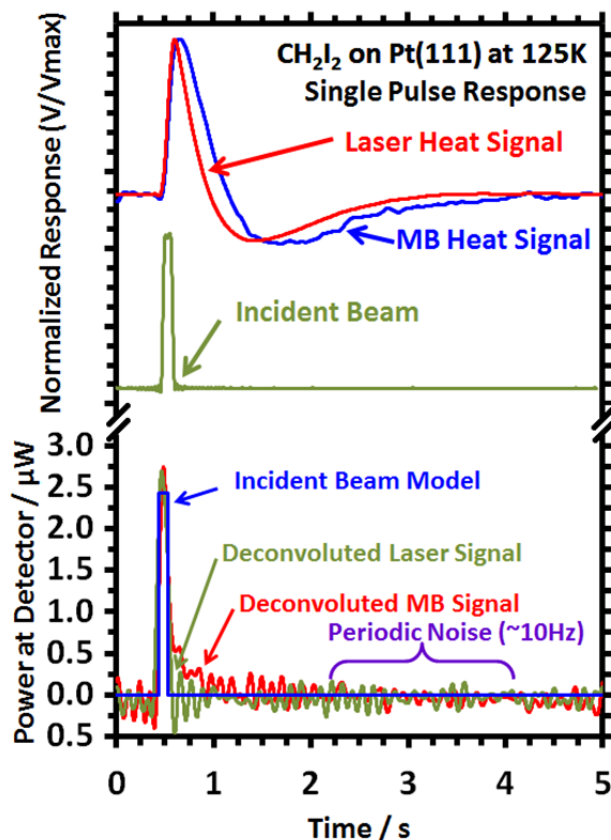


Figure 3.3. Top: The incident beam profile and typical response signals measured for the laser beam and the molecular beam (MB), reproduced from Fig. 3.1. Bottom: the incident power at the detector from the molecular beam as a function of time, extracted by deconvoluting the instrument response function from the MB heat signal using the FFT method. The square wave incident beam model is also shown. The deconvoluted MB signal is the result of deconvoluting the MB heat signal with the instrument response function, while the deconvoluted laser signal is the result of deconvoluting a single laser heat signal with that same instrument response function. (The average of many laser heat signals is used to extract the instrument response function.) It can be seen that for this individual MB pulse, the deconvoluted heat signal is broader than the incident beam, showing that heat is deposited on a slower time scale than during the laser pulse. The deconvoluted pulse tail decays quickly towards the baseline zero, but continues to be distinguishable above the baseline noise for almost 1s before being overwhelmed by the periodic noise introduced by this method.

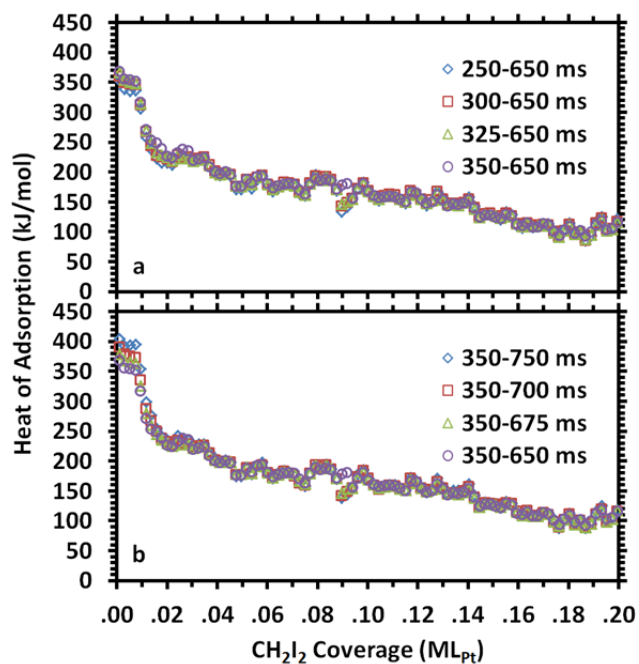


Figure 3.4. Differential heat of adsorption of CH_2I_2 on clean Pt(111) at 125K as a function of CH_2I_2 coverage, extracted by integrating each deconvoluted pulse (see Fig. 3.3) over the different integration windows stated. By increasing the integration window by time increments that are $\frac{1}{4}$ of the period of the dominant periodic noise by moving either to earlier start times (a) or later stop times (b), this shows that no systematic change in heat is found at most coverage. Thus, the periodic noise does not have a significant impact on the choice of window for integration. However, at very low coverages, which had the most broadened heat signal pulses, increasing the integration window to longer times does increase the heats systematically as it captures more and more of the slow heat deposition. The heat stops increasing when this is extended to ~ 1000 ms, after which the effect saturates (see Fig. 3.5).

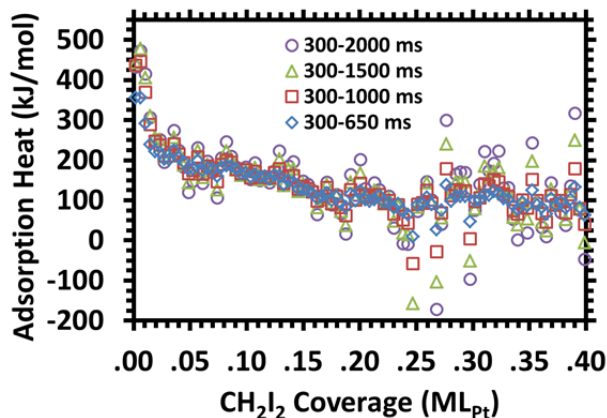


Figure 3.5. Differential heat of adsorption of CH_2I_2 on Pt(111) at 125K as a function of CH_2I_2 coverage obtained using different time window widths for integrating the heat pulses. These heats were extracted by integrating each deconvoluted pulse (see Fig. 3.3) over the specific time windows shown. A large enough window must be selected to capture all of the heat deposited (see low coverage results in Fig. 3.4), and ideally one would integrate across the full time window. This shows, however, that as the integration window gets larger, the noise increases, although the average heat remains unchanged at most coverages. At low coverages where the heat signal is most broadened, the heat increase with integration window until 300-1000 ms, above which it has the same average. This shows that whatever slow kinetics are occurring on the surface, they have already completed by 1000 ms.

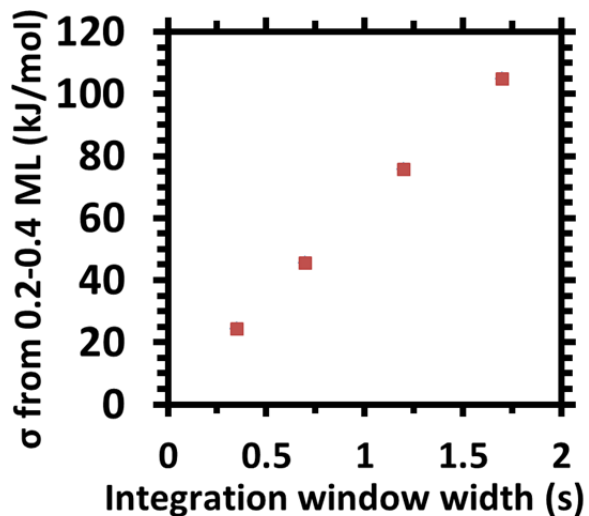


Figure 3.6. The standard deviation of the heat measured in Fig. 3.5 over the coverage range from 0.2 to 0.4 ML (where the heat is nearly constant with coverage) as a function of integration window width beginning at 0.3 s. The standard deviation increases proportional to the integration window width. The best selection of window width was decided based on seeking to minimize this noise while simultaneously capturing all of the heat deposition occurring for a pulse of gas (which time duration varies depending upon the reaction being studied and surface temperature).

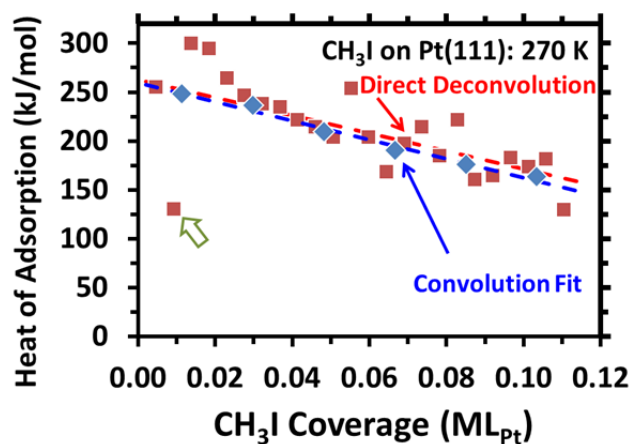


Figure 3.7. Comparison of differential heat of adsorption versus coverage results for CH₃I on clean Pt(111) at 270 K, between the convolution fitting method of Silbaugh et al.⁴⁶ (blue points) and the direct deconvolution method of this paper (red points). In Silbaugh's method, four pulses were averaged to reduce noise. Each of the points of Silbaugh is essentially the average of the four adjacent points from the method of this paper. The best-fit lines shown are very similar, and represent the equations: $y = (259-969x)$ kJ/mol using the convolution fit method, and $y = (263-911x)$ kJ/mol using the direct deconvolution method.

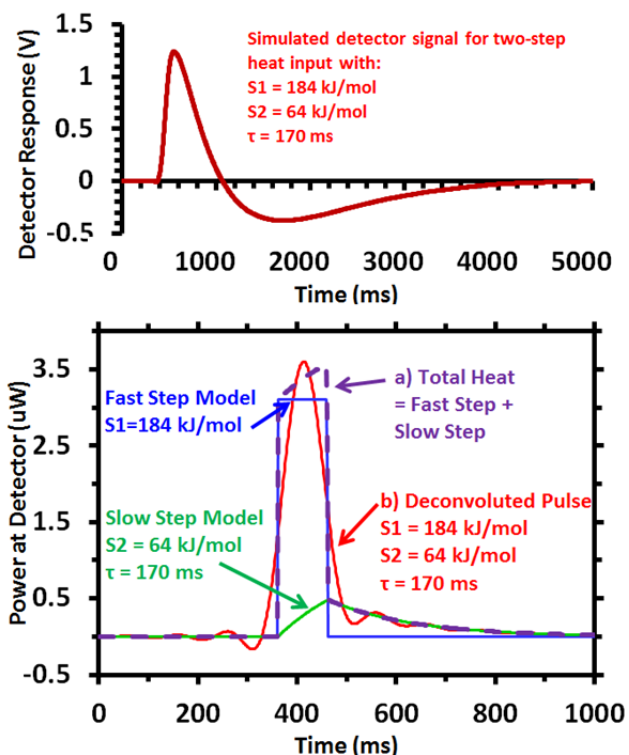


Figure 3.8. Bottom: Comparison of the input power versus time due to the heat of adsorption followed by dissociation for CH_3I adsorption on $\text{Pt}(111)$ at 270 K for a typical 0.0046 ML pulse within the coverage range 0-0.02 ML, as calculated from:

(a) The two-step model of Silbaugh et al.⁴⁶ for this condition wherein CH_3I first adsorbs molecularly with a heat of 184 kJ/mol and then dissociates via a first-order reaction with time constant $\tau = 170$ ms and heat of 64 kJ/mol (purple, dashed curve). Also shown are the separate heat inputs from the fast step (blue) and slow step (green). The curve at the top shows the simulated signal waveform for this same exact two-step heat input model, as generated using the simulation method of Silbaugh et al. which sums heat-scaled waveforms for its two steps, using the measured lineshape for the signal response to laser heating for the first, fast step and its convolution with first-order exponential decay kinetics for the slow step.

(b) Deconvolution of top simulated signal to remove the instrument response function (shown in Fig. 3.2).

Curves (a) and (b) agree, except for the damped periodic noise that results from deconvoluting over the finite time window used (4000 points over 5 s).

Chapter 4: Energetics of Adsorbed CH₂ and CH on Pt(111) by Calorimetry: the Dissociative Adsorption of Diiodomethane

This chapter reprinted with permission from: C.A. Wolcott, I. X. Green, T.L. Silbaugh, Ye Xu, and C.T. Campbell, Energetics of Adsorbed CH₂ and CH on Pt(111) by Calorimetry: The Dissociative Adsorption of Diiodomethane, *J. Phys. Chem. C*, Article ASAP, DOI: 10.1021/jp505494a

Chapter Abstract

The enthalpies of molecular and dissociative adsorption of CH₂I₂ on Pt(111) at 100-210 K were studied using single crystal adsorption calorimetry (SCAC) and density functional theory (DFT). Gaseous CH₂I₂ was found to adsorb on the Pt(111) surface at 100 K to form CH_{2,ad} plus 2 I_{ad}, with a calorimetric heat of adsorption that decreases with coverage as 222-4800 kJ/mol for $\theta < 1/8$, where θ is the coverage in monolayers, ML, defined as the number of dissociatively adsorbed CH₂I₂ molecules per Pt(111) surface atom. These coadsorbed iodine atoms greatly destabilize the methylene species even at the lowest coverage, which we attribute to their inability to diffuse away from the near-neighbor sites where they are initially produced on the short time scale of the heat measurement. A mixture of dissociative adsorption fragments of methylene and methylidyne were detected at elevated temperatures between 125 K and 190 K. At 210 K, CH₂I₂ adsorption produced CH_{ad}, H_{ad}, and 2 I_{ad}, with the I_{ad} now able to diffuse away to minimize repulsions on the time scale of heat measurements. The calorimetric heats for this reaction provide an estimate of the heat of formation of CH_{ad} on Pt(111) of -71 kJ/mol with a HC-Pt(111) bond enthalpy of 665 kJ/mol at 0.04 ML coverage. These results are used together with prior measurements to construct an energy landscape for the stepwise dehydrogenation of methane on Pt(111), and are compared to previous experimental results and theoretical predictions. DFT calculations reproduce the experimental stability of CH_{ad} and CH_{3,ad} on Pt(111)

to within ~ 20 kJ/mol, and the experimentally measured I_{ad} - I_{ad} repulsion energy between coadsorbed iodine adatoms to within 25%, and show that there is very strong repulsion between $CH_{2,ad}$ and I_{ad} when in nearby sites, which seems to be the case when formed at 100 K from CH_2I_2 , even at very low coverage.

Introduction

The fossil fuel industry relies heavily on heterogeneous catalytic processes, such as hydrocarbon reformation, isomerization, hydrogenation, and dehydrogenation². With the increasing scarcity of crude oil and a boom in newly discovered methane resources, understanding the catalysis of methane conversions is crucial for both advancing current catalytic processes and the discovery of new generations of catalysts. Despite this importance, the enthalpies of formation of the adsorbed fragments produced by methane dissociation on various catalyst surfaces are still largely unmeasured. These have only been measured on Pt(111), where only the values for adsorbed CH_3 ($CH_{3,ad}$) and CH_{ad} have been reported⁴⁴. That value for CH_{ad} was only measured in the presence of high coverages of coadsorbed iodine and CH_{ad} . The Pt(111) single crystal surface is the simplest and most studied model of Pt catalysts. It is the lowest energy Pt surface, and is believed to be the dominant facet of Pt nanoparticles. Here we report direct measurements of the enthalpies of formation of $CH_{2,ad}$ and CH_{ad} species on the Pt(111) single crystal surface versus surface coverages using single crystal adsorption calorimetry (SCAC) to study the dissociative adsorption of diiodomethane. The enthalpy for the low-temperature $CH_{2,ad}$ species is complicated by the presence of nearby I_{ad} even at the lowest coverage. Together with our previously reported measurements of the enthalpies of formation of $CH_{3,ad}$ and CH_{ad} on Pt(111) from the dissociative adsorption of methyl iodide⁴⁴ and prior results from temperature programmed desorption (TPD)^{110, 111}, these combined results allow us to build

a complete energy diagram for the stepwise dehydrogenation of methane on this important model catalyst surface. The results also provide benchmarks for validating the accuracy of new methods for density functional theory (DFT) calculations of reaction energies for adsorbed species on metal catalysts. Improving such computational methods is very important in improving basic understanding of catalytic mechanisms and in rational catalyst design.

Methane dehydrogenation products on the Pt(111) surface have been studied intensively using a variety of techniques including infrared spectroscopy (IR)^{112,113}, electron energy loss spectroscopy (EELS)¹¹⁴, X-ray photoelectron spectroscopy (XPS)¹¹⁰, sum frequency generation spectroscopy (SFG)¹¹⁵, and TPD¹¹⁶. The first dehydrogenation fragment, CH_{3,ad}, is usually generated by CH₃I dissociative adsorption^{117,118} or high energy CH₄ impingement¹¹⁰. It has been reported that CH_{3,ad} is stable on Pt(111) up to 270 K^{112,110,117}, and dissociates to form CH_{ad} species at higher temperatures^{110,117}. CH_{2,ad} is proposed to be a very unstable intermediate, and CH_{ad} species is stable up to 500 K.^{110,109} Our SCAC study of CH₃I dissociative adsorption on Pt(111) found that the enthalpy of formation of CH_{3,ad} is -53 kJ/mol at 0.04 ML coverage. The CH_{2,ad} species is not produced in significant quantities on the Pt(111) surface when CH_{3,ad} is heated up to its dissociation temperature (~270 K). Instead, when its first C-H bond breaks, it converts almost immediately to CH_{ad} and methane gas^{44, 111} (probably via transient CH_{2,ad} + H_{ad} intermediates). Thus, it is impossible to acquire enthalpy information on the CH_{2,ad} intermediate using CH_{3,ad} dissociation, whether produced from CH₃I or some other reagent. This is because the C-I bond in CH₃I does not readily break until over 190 K¹¹², while the C-H bond in CH_{2,ad} on Pt(111) (produced by dissociative adsorption of CH₂I₂) breaks already at ~130 K¹⁰⁹. In an attempt to study the energetics of CH_{2,ad} here, we therefore study the dissociative adsorption of

CH₂I₂ below 130 K, and the energetics of CH_{ad} (the product of its further dissociation) above 130K.

The surface adsorbed CH₂ intermediate on Pt(111) has been observed by reflectance adsorption IR spectroscopy (RAIRS) by Deng et al., following the dissociative adsorption of CH₂I₂¹⁰⁹. Diiodomethane was found to adsorb dissociatively on the Pt(111) surface at 85 K forming CH_{2,ad} and 2 I_{ad}. Further increase of the surface temperature induced the dissociation of CH_{2,ad} species to CH_{ad} and H_{ad} on the Pt(111) surface, where a combination of CH_{2,ad} and CH_{ad} species was observed in IR spectra at 130 K and 150 K. Only CH_{ad} species was observed between 200 K and 500 K, as all CH_{2,ad} species had dissociated by 200 K. No reaction products were detected by TPD below 200 K, while C₂H₄ and CH₄ desorption peaks were observed at 224 K and 266 K respectively. Following this report, we probe here the dissociative adsorption of CH₂I₂ molecule on Pt(111) surface at a variety of temperature ranges, aiming to measure the heat of formation of CH_{2,ad}, and CH_{ad}. It is important to note that the time scale on the RAIRS experiments is quite long, minutes or longer, whereas the SCAC measurements have a relatively short measurement window of 102 ms dosing time with 5 s delay between doses. It is crucial for these calorimetric experiments to find the “perfect” temperature where the adsorption and dissociation of CH₂I₂ on Pt(111) is complete on the SCAC measurement time scale with clean production of the desired fragment.

Experimental Methods

Experiments were performed in a stainless steel ultrahigh vacuum (UHV) chamber (base pressure < 2×10⁻¹⁰ mbar) equipped with XPS, Auger electron spectroscopy (AES), low energy ion scattering spectroscopy (LEIS), low-energy electron diffraction (LEED), quadrupole mass

spectrometry (QMS), liquid N₂ cooled molecular beam, and SCAC. This apparatus and the procedures for SCAC have been described in detail previously⁴². In short, a 1 μm thick Pt(111) single crystal was employed and was routinely cleaned by cycles of sputtering with 1.25 kV Ar⁺, annealing at 1123 K for 1 min, and annealing to 873 K in 1×10⁻⁸ mbar of O₂ for 2 min. After each cycle the cleanliness of the sample was checked using AES until no carbon residue was detected. The order of the cleaned Pt(111) surface was confirmed by LEED with a sharp hexagon pattern. Between each SCAC experiments, a quick flash to 1173 K of the Pt(111) sample was performed to restore a clean surface.

SCAC was performed by exposing the Pt(111) surface to a pulsed molecular beam of diiodomethane gas. Each pulse of CH₂I₂ was 102 ms long and there was a five-second delay between pulses to avoid adsorption/reaction overlap. The diiodomethane was purchased from Sigma-Aldrich (99+%) and further purified by repeated freeze-pump-thaw cycles. The liquid CH₂I₂ reservoir was held at room temperature and shielded from light to prevent its dissociation (cite 15). The molecular beam was created by expanding ~0.9 mbar of CH₂I_{2,g} (its vapor pressure near room temperature) through a glass capillary array heated to 328 K, and was collimated via a series of five liquid N₂ cooled apertures producing a spot 4.36 cm in diameter on the sample. Based on the large barrier to isomerize CH₂I₂ (estimated to be ~200 kJ/mol by DFT)¹¹⁹ and the short residence time of gas molecules (<20 s) in the heated part of the beam (the glass capillary array alone), it is unlikely that isomers formed in any appreciable quantity. (Note that CH₂I₂ molecules at 328K have less than 2 kJ/mol more energy than at room temperature based on the reported heat capacity of CH₂I_{2,g}.¹²⁰) The purity of the diiodomethane molecular beam was also verified periodically with the QMS cracking pattern when monitoring the direct CH₂I₂ beam. The

flux of the CH₂I₂ beam was measured using a liquid N₂ cooled quartz crystal microbalance (QCM) and each CH₂I₂ pulse was determined to be $\sim 5 \times 10^{11}$ CH₂I₂ molecules.

The heat released by each pulse of CH₂I₂ was measured using a pyroelectric polymer ribbon gently pushed to the backside of the sample. The sensitivity of the pyroelectric ribbon was calibrated using a HeNe (632.8 nm) laser with known energy for each individual experiment. Calorimetric measurements versus coverage at each temperature were repeated at least 5 times and the average values are reported.

The heat response during each pulse is recorded as a function of time. When calibrating the total heat deposited using the laser pulse, the shape of the molecular deposition heat pulse determines how to extract the heat of adsorption data. If the heat deposited by a molecular beam pulse happens very quickly (<10 ms) no advanced analysis is needed, and the heat can be determined by scaling the laser pulse heat data to fit the molecular pulse heat data. If there is a single slow (~10-1000 ms) rate-limiting step, the molecular heat pulse data appears broadened relative to the shape of the laser pulse heat data. The data then can be fitted by modelling the molecular pulse heat data as the sum of two components from a two-step mechanism as described previously⁴⁶; an instantaneous heat due to molecular adsorption, which has the same shape as the heat signal from laser pulses, and heat from a slow dissociation step, which is a convolution of the laser pulse signal's line shape with an exponential decay function. If the any heat deposition of a step is too slow (>1000 ms) then it will not contribute measurably to the heat signal measured. If the heat deposition is slow (>10 ms) and there is not a single rate-determining step, as was the case for CH₂I₂ adsorption on Pt(111), neither of these methods will work.

A new method was developed and used here for the first time to extract the heats of adsorption from SCAC data. During a SCAC experiment, each calorimeter heat signal versus time collected for a single pulse of gas is a convolution of the heat deposition function generated during the adsorption/reaction process and the calorimeter's instrument response function. This new method uses basic signal processing techniques to extract the instrument response function for the calorimeter from the signal measured for a known heat-versus-time input, and then uses that instrument response function to extract the heat-versus-time data for each pulse directly. In brief, the laser heat signal is the convolution of the instrument response function and the laser pulse heat deposition profile, which is a square wave of known intensity and duration. Using deconvolution by Fourier transformation and basic signal processing techniques it was possible to extract the instrument response function from the heat signal averaged from many laser pulses. Using this instrument response function and the molecular beam heat signal versus time for each pulse of the molecular beam, the heat deposited during each pulse of adsorbing gas was deduced as a function of time using the same Fourier transformation signal deconvolution method. This method of data processing was tested on data from our group which was modeled using both of the previously used methods of data processing and was found to agree extremely well with them. Fig. 4.1 shows a typical heat versus time plot extracted from the signal for one gas pulse using this new method. To extract the energy deposited in a pulse one simply integrates the heat curve over time. Care is required in choosing the integration window of the heat signal since the noise grows with the total time integrated but one wants to capture all the relevant heat. To balance this, we chose a start time ~ 200 ms before the middle of the molecular beam pulse (which is 102 ms long) and a stop time ~ 500 ms after that. This means we miss any heat deposited by reactions that occur slower than ~ 650 ms, which means we get $>95\%$ of the heat for

any reactions that happen with a time constant faster than ~ 200 ms. It should be noted that while increasing the integration window to as much as ~ 1500 ms after the peak of the pulse increased the point-to-point noise in our differential heat measurements, the integral heat remained the same to within 2%. Since the limited data range used for the Fourier transform deconvolution introduces periodic oscillations in the heat versus time, one must also fine tune these integration limits to fall halfway between these minima and maxima to avoid systematic error. It is easy to identify the periodicity and time locations of these minima and maxima by averaging multiple curves like Fig. 4.1. It was found that in these experiments the periodic noise contributed negligibly to the heat.

Computational methods

Self-consistently periodic DFT calculations were performed using the Vienna Ab Initio Simulations Package¹²¹⁻¹²³ (VASP) with the Perdew–Burke–Ernzerhof functional in the generalized gradient approximation (GGA-PBE)¹²⁴ as well as with the optB86b van der Waals functional (optB86b vdW-DF) developed by Klimeš et al..^{125, 126} Both GGA-PBE and optB86b vdW-DF reproduced reasonable accurately the experimental differential heat of adsorption of I_{ad} alone and its coverage dependence (see Table 4.1), with a slope versus I_{ad} coverage of -148 kJ/mol per ML, which is within 25% of the reported experimental slope of -199 kJ/mol per ML. Furthermore, we showed previously that optB86b vdW-DF provides excellent predictions for the adsorption properties for *tert*-butyl iodide and the *t*-butyl group on Pt(111)⁹³. The core electrons were described by the projector augmented wave (PAW) method^{123, 127} (Pt, 230 eV cutoff; I, 176 eV cutoff; C, 400 eV cutoff; and H, 250 eV cutoff) and the Kohn-Sham valence states (including Pt(5d6s); I(5s5p); C(2s2p); and H(1s)) were expanded in a plane wave basis set up to a cutoff

energy of 400 eV. The electronic states were smeared using a first-order Methfessel-Paxton scheme with a temperature of 0.075 eV.¹²⁸ All total energies were extrapolated back to 0 K.

The gas-phase species were calculated in an $18 \times 18.2 \times 18.4 \text{ \AA}^3$ unit cell. The majority of the adsorbates were modeled on a Pt(111) slab with a (4×4) surface unit cell, corresponding to 1/16 monolayer (ML) of coverage. In addition, $(\sqrt{3} \times \sqrt{3})$, (2×2) , (3×3) , and (6×6) surface unit cells were also used in a limited number of cases, corresponding to 1/3, 1/4, 1/9, and 1/36 ML of coverage, respectively. The surface Brillouin zone was sampled on a $5 \times 5 \times 1$ Monkhorst-Pack k -point mesh for the (2×2) – (4×4) surface unit cells, and on a $2 \times 2 \times 1$ Monkhorst-Pack k -point mesh for the (6×6) surface unit cell. A vacuum space of $\sim 16 \text{ \AA}$ was included in the z direction, together with electrostatic decoupling in the z direction,¹²⁹ to minimize interactions of neighboring images. The calculated lattice constant for Pt was 3.978 \AA in PBE and 3.958 \AA in optB86b vdW-DF, both in close agreement with experiment (3.92 \AA ¹³⁰). Spin polarization was found to be negligible for all of the surface species in this study.

All of the Pt(111) slabs consisted of four Pt(111) layers. The top two layers were fully relaxed and the bottom two were fixed at bulk positions during geometry optimization. All geometry optimization was converged to 0.01 eV/\AA for each relaxed degree of freedom. Adsorption and bond energies were calculated as $\Delta E = E_{slab} + (E_{mol} + E_{mol}^{ZPE}) - (E_{total} + E_{total}^{ZPE})$, where E_{slab} , E_{mol} , and E_{total} are the total energies of the clean surface without any adsorbate, the adsorbate isolated in the gas phase in a neutral state (closed-shell or radical), and the surface with the adsorbate. E^{ZPE} is the corresponding zero point energy (ZPE; see below). A more positive ΔE therefore corresponds to stronger adsorption. All DFT-calculated ΔE 's reported below included ZPE corrections unless stated otherwise. In all cases the ZPE correction for the same system was practically identical in GGA-PBE and optB86b vdW-DF. For the adsorption of gas-

phase species, the DFT total energy ΔE 's can be converted to the corresponding adsorption enthalpies (ΔH 's) by adding $k_B T$ (or RT) to ΔE , the amount of which is small at the experimental temperatures (100~210 K). The ΔE of a set of coadsorbates at the zero-coverage limit was estimated using the energy of each individual adsorbate calculated on a separate (4×4) surface unit cell. The convergence of the adsorption energies with respect to parameters including the valence state cutoff energy, k -point sampling density, and number of metal layers in the Pt(111) slab had been previously verified⁹³.

The minimum-energy reaction path for an elementary step and the associated transition state (TS) were determined using a combination of the climbing-image nudged elastic band (CI-NEB) method¹³¹ and the dimer method.¹³² The activation energy was calculated as

$$E_a = (E_{TS} + E_{TS}^{ZPE}) - (E_{IS} + E_{IS}^{ZPE}),$$

where IS and TS denote the initial state and transition state,

respectively. Each TS was verified to possess only one vibrational mode with imaginary frequency in the direction of the dissociating bond. The vibrational modes and frequencies were calculated in the harmonic oscillator approximation from a finite difference approximation of the Hessian matrix. The magnitude of the displacement was 0.01 Å in each relaxed degree of freedom. The zero point energies were calculated from the vibrational frequencies (ν_i) of a

molecule (gas-phase or adsorbed) as
$$E^{ZPE} = \frac{1}{2} \sum_i h \nu_i.$$

Experimental Results

Diiodomethane adsorption on Pt(111) was studied over a range of temperatures between 100 K and 210 K. Coverages (θ) are reported in CH₂I₂ monolayers (MLs), and defined as the number of CH₂I₂ molecules irreversibly adsorbed to the surface (irrespective of whether they dissociated or not) normalized to the atomic surface density of Pt(111), 1.50×10^{19} Pt atom/m².

We report below the heat of adsorption, defined here as the negative of the differential standard molar enthalpy change for the adsorption reaction with the gas being at the same temperature as the Pt(111) surface. This heat required small corrections of the raw measured heats as described previously⁴². The sticking probability of CH₂I₂ molecules was measured by the King and Wells method⁸² simultaneously with the heat measurements. Unity sticking probability was observed for all the coverage ranges and their corresponding temperatures reported below.

Dissociation of CH₂I₂ to produce CH_{2,ad} plus 2 I_{ad} on Pt(111) was reported to take place at 85 K by Deng et al.¹⁰⁹, giving the net reaction:



Fig. 4.2 shows the heat of adsorption of CH₂I₂ on Pt(111) at 100 K versus coverage, which decreases linearly with coverage (θ , in ML) as (222-480 θ) kJ/mol in the first 1/8 ML.

Continuing to dose eventually leads to saturation of the Pt sites and formation of a multilayer of molecular CH₂I₂ solid, which is indicated by a sharp change of slope in Fig. 4.2 to nearly zero at ~0.20-0.22 ML. The negative slope in the chemisorbed layer is due to the increasing lateral repulsion between adsorbed fragments and molecules with increasing coverage. The sharp change in slope at ~1/8 ML is attributed to the saturation of the dissociative adsorption of CH₂I₂ to produce CH_{2,ad} + 2 I_{ad}. This coverage agrees well with that expected based on the footprint of each product, as follows: Assuming that each I_{ad} blocks three Pt atoms since it adsorbs on three-fold hollow sites and has a saturation coverage of 0.33 ML^{133, 134} and that each CH_{2,ad} blocks two Pt atoms since it adsorbs on the bridge sites on Pt(111)¹³⁵, the dissociative adsorption of CH₂I₂ will need at least eight platinum atoms for its three products, if none share the same Pt surface atoms in bonding. These should therefore saturate at 1/8 ML. The heat decreases rapidly between 1/8 ML and ~1/4 ML. In this coverage range, we propose that the CH₂I₂ or its

dissociation products are still bonding directly to Pt atoms but now in a much less stable bonding configuration, whereby two adsorbates must now bind to the same Pt atom. By 0.20 to 0.25 ML, the heat has almost reached its multilayer value, but is slightly higher up to 0.4 ML, possibly due to a long-range attraction to the underlying metal when separated from it by only one layer of adsorbates, which damps to nearly zero for thicker layers.

Fig. 4.2 shows that at higher coverages, the heat reaches a constant multilayer value of 89.1 kJ/mol. This multilayer heat should be nearly identical to the heat of sublimation of CH₂I₂, and indeed agrees well with our estimate of the heat of sublimation of bulk CH₂I_{2,s} of 87 kJ/mol at 100 K. This heat of sublimation was estimated using the reported heats of vaporization and fusion of CH₂I₂ at their normal transition temperatures as well as the heat capacities of the gas and liquid phase CH₂I₂ at 298 K^{136, 137}. The heat capacity of the CH₂I_{2,s} could not be found, and was estimated to be the same as the heat capacity of the liquid. All heat capacities were assumed to be independent of temperature with the same value as reported at 298 K.

Adsorption heats were measured for CH₂I₂ on Pt(111) at 210 K to study the formation of CH_{ad} species, based on the IR observation of CH_{ad} as the only adsorbed hydrocarbon species after adsorbing CH₂I₂ at 85 K and warming briefly to 200 K¹⁰⁹. This was attributed to the net reaction:

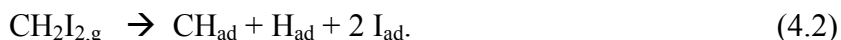


Fig. 4.3 shows the differential heat of adsorption of CH₂I₂ on Pt(111) at 210 K as a function of coverage in the range below 0.15 ML, where the short-term sticking probability remained at unity. The long-term sticking probability drops from ~unity at 0.16 ML to ~zero by 0.18 ML. The heat of adsorption of CH₂I₂ on Pt(111) at 210 K forming CH_{ad} + H_{ad} + 2 I_{ad} was well fitted by the straight line (533-1480θ) kJ/mol in the first 0.09 ML, as shown in Fig. 4.3. Above 0.09

ML, the heat drops much more rapidly, then almost levels off between 0.11 and 0.15 ML, with the heat slowly decreasing from 120 to 100 kJ/mol, very similar to the heat measured in this same coverage range at 100 K (Fig. 4.2) and attributed above to molecularly adsorbed CH_2I_2 only partially bonded to Pt atoms between the adsorbed fragments produced at lower coverages. The rapid drop in heat starting at 0.09 ML suggests that the full decomposition of CH_2I_2 to $\text{CH}_{\text{ad}} + \text{H}_{\text{ad}} + 2 \text{I}_{\text{ad}}$ stops at this coverage. This coverage agrees well with the expected coverage of 0.10 ML required to block all of the Pt atoms by these products, based on the following: Each CH_2I_2 should require a total of ten platinum atoms: three for each CH_{ad} which should sit in a threefold hollow site¹³⁵, three for each of the two I_{ad} (see above) and one for each H_{ad} (whose saturation coverage is 1 ML¹³⁸). No CH_2I_2 multilayer formation was observed at this temperature, indicated by the drop of the sticking probability from \sim unity at 0.15 ML to \sim zero by 0.18 ML. This temperature range for multilayer stability agrees with Zaera *et al.*¹³⁹, who reported the desorption of CH_2I_2 multilayers from Ni(110) surface already at 198 K in a TPD study.

Figure 4.4 presents the differential heat of adsorption of CH_2I_2 on clean Pt(111) as a function of total CH_2I_2 coverage measured at six different temperatures in the range 100-210 K. The data at intermediate temperatures show a transition between the behavior at 100 K and 210 K with increasing temperature. They are interpreted in detail in the Discussion section below.

DFT Results

Adsorbed CH_2I_2 , CH_2I , CH_3 , CH_2 , and CH on Pt(111) were calculated at the low coverage of 1/16 ML. The minimum-energy adsorption geometries of these species are shown in Fig. 4.5 a-e, and the associated bond energies, in both functionals used (optB86b vdW-DF and GGA-PBE) are reported in Table 4.2. Also shown in Fig. 4.5 are the minimum-energy structures for $\text{CH}_{2,\text{ad}}+2\text{I}_{\text{ad}}$ at two different low coverages (f and g) and the transition states for C-I bond

scission in $\text{CH}_2\text{I}_{2,\text{ad}}$ and in $\text{CH}_2\text{I}_{\text{ad}}$ coadsorbed with one I_{ad} (h and i). The adsorption of atomic I_{ad} on Pt(111) was investigated theoretically previously and found to sit in three-fold hollow sites^{93, 140}, as also in these coadsorbed structures here. Fig. 4.6 shows the DFT-calculated reaction energy profiles for the dissociative adsorption of $\text{CH}_2\text{I}_{2,\text{g}}$ at low coverage based on the two different functionals, both of which indicate that the step-wise loss of the two I atoms and then an H atom is exothermic at each step. The activation barrier along the minimum-energy reaction path for the initial C-I bond scission in $\text{CH}_2\text{I}_{2,\text{ad}}$ was calculated to be $E_{a,1} = 31/27$ kJ/mol (optB86b/PBE). The barrier for the 2nd C-I bond scission (i.e., in $\text{CH}_2\text{I}_{\text{ad}}$) was calculated to be $E_{a,2} = 7/10$ kJ/mol (optB86b/PBE) and the barrier for C-H bond scission in $\text{CH}_{2,\text{ad}}$ was previously reported by Michaelides et al. to be $E_{a,3} = 14$ kJ/mol (PBE without ZPE at 1/6 ML coverage)¹⁴¹, both of which are lower than the first barrier. These results will be discussed in detail below.

Discussion

The standard enthalpies of formation (ΔH_f) of $\text{CH}_{2,\text{ad}}$ and CH_{ad} can be estimated using the integrated heats of the dissociative adsorption of CH_2I_2 on Pt(111) measured by SCAC at 100K and 210K, respectively, in both cases at 0.04 ML. The thermodynamic cycles employed to estimate $\Delta H_f(\text{CH}_{2,\text{ad}})$ and $\Delta H_f(\text{CH}_{\text{ad}})$ as well as the bond enthalpies for these two adsorbed species, $\text{D}(\text{Pt}=\text{CH}_2)$ and $\text{D}(\text{Pt}\equiv\text{CH})$, are shown in Figs. 4.7 and 4.8, respectively. The enthalpies of formation are calculated assuming repulsive interactions from adsorbed iodine has a negligible contribution¹⁴² at this low coverage, an assumption discussed below to be very inaccurate for $\text{CH}_{2,\text{ad}}$ but not for CH_{ad} . The enthalpies of formation of the gaseous methylidyne (CH) and methylene (CH_2) and iodine (I) radicals shown here were adopted from measured values¹⁴³, while the enthalpy of formation of adsorbed iodine atoms as a function of iodine adatom coverage (θ_I) is adopted from a careful TPD study carried out by Labayen et al.¹³⁴, which is

given as a function of iodine coverage as (255-1990_I) kJ/mol. The enthalpy of formation of H_{ad} on Pt(111) is calculated from the reported enthalpy of adsorption of H_{2,g} (-36 kJ/mol, which is an average from several reports⁹⁰). The $\Delta H_f(\text{CH}_{2,\text{ad}})$ and $\Delta H_f(\text{CH}_{\text{ad}})$ on Pt(111) are calculated to be 188 kJ/mol and -71 kJ/mol, respectively, both at 0.04 ML total coverage. The subsequent bond dissociation energies for adsorbed CH₂ and CH detaching from Pt(111), D(Pt=CH₂) and D(Pt≡CH), were calculated to be 198 kJ/mol and 665 kJ/mol respectively. The bonding enthalpy for the Pt≡CH bond is in excellent agreement with the bond enthalpy of 633 kJ/mol measured by Yeo et al.¹⁴⁴ for the Pt≡CCH₃ species which contains an equal number of Pt-C bonds but where the H is replaced with CH₃. (The number reported here from Yeo et al. was corrected from their reported value to account for a heat calibration error, following the same procedure we reported earlier⁶⁶.) The coverage used for Figs. 4.7-4.8 (0.04 ML) was chosen to be approximately half the saturation coverage for the CH_{2,ad} and CH_{ad} formation processes captured at 100 K and 210 K (in Figs. 4.2 and 4.3, respectively), and was selected to balance the possible influence of surface defect sites (<0.01 ML for this sample^{43, 47, 48, 92}) and lateral repulsion from adsorbed species due to surface crowding (high coverage).

The slopes of the straight lines through the differential heats from zero to saturation coverage in Figs. 4.2 and 4.3 (-480 and -1430 kJ/mol per ML, respectively) can be used to correct these heats of formation and bond energies from 0.04 ML to other coverages in the range up to ~0.09 ML. Figs. 4.7 and 4.8 use the *integral* heats, which vary with exactly half these slopes. One must also correct for the variation in the integral heat of iodine adsorption with I_{ad} coverage (using the equation given above for pure iodine adlayers). Table 4.1 shows the resulting variations with coverage in the heats of formation and bond energies for these three species, as well as for CH_{3,ad} from our previous paper⁴⁸. Table 4.1 shows that decreasing the

coverage of adsorbed iodine and CH_{ad} or $\text{CH}_{3,\text{ad}}$ pushes the enthalpies of formation more negative (more stable) and makes the apparent bond energies to Pt stronger, while increasing the coverage of adsorbed iodine and CH_{ad} or $\text{CH}_{3,\text{ad}}$ has the opposite effects. This strong coverage dependence seen in Table 4.1 is attributed to lateral repulsion between the adsorbed products.

This is not seen for the $\text{CH}_{2,\text{ad}}$ species, for which the heat of formation and bond enthalpies have a negative slope, suggesting increasing coverage makes the adsorbate more stable. Based on the general behavior of other adsorbed hydrocarbons and their fragments, this is not considered to be physically reasonable. We attribute it to an artefact of the highly non-equilibrium population of surface sites achieved in the short measurement time (<200 ms) at the low temperature of this measurement (100 K).

At 100 K, the adsorbed fragments from CH_2I_2 dissociation ($\text{CH}_{2,\text{ad}} + 2 \text{I}_{\text{ad}}$) are probably frozen in their initial locations (at nearest-neighbor), and unable to diffuse apart to minimize adsorbate-adsorbate repulsions in the short time scale of the heat measurements. Because of this, the enthalpy we used to estimate the stability of the I_{ad} products at low coverage here (based upon large, equilibrium separations) is too stable, which leads to badly underestimating the stability of isolated $\text{CH}_{2,\text{ad}}$ with this approach. That is, it is probably not valid to assume at 100 K that the coadsorbed iodine has a negligible effect on the adsorption energetics of the methylene fragment and the other I_{ad} , as was done in Fig. 4.7. This is a problem even in the limit of zero coverage, since each CH_2I_2 produces a $\text{CH}_{2,\text{ad}}$ and two I_{ad} in such close proximity. Thus, strong lateral repulsion from and between neighboring iodine species probably causes the bond enthalpy of the methylene species to Pt(111) as estimated here to be much lower than the true value for an isolated $\text{CH}_{2,\text{ad}}$ species. Similar adsorption experiments were carried out at 110 K and 115 K in hopes that this would allow the adsorbates to diffuse apart during the heat

measurement time, but these showed an identical heat profile as the 100 K data in Fig. 4.2.

Further experiments were done at even higher temperatures, but partial decomposition of $\text{CH}_{2,\text{ad}}$ to $\text{CH}_{\text{ad}} + \text{H}_{\text{ad}}$ was observed to occur already by 125 K, and occurred in increasing fractions as temperature was increased further, as shown in Fig. 4.4 and discussed below.

Two clear trends with increasing adsorption temperature can be seen in Fig. 4.4. The first trend is an increase in the initial heat deposited during the CH_2I_2 adsorption. We attribute this to the adsorption product composition change from $\text{CH}_{2,\text{ad}} + 2\text{I}_{\text{ad}}$ (i.e., reaction (1)) at 100 K to forming a mixture of $\text{CH}_{2,\text{ad}}$, 2I_{ad} , CH_{ad} , and H_{ad} species at higher temperatures (i.e., a combination of reactions (1) and (2)), with increasing $(\text{CH}_{\text{ad}} + \text{H}_{\text{ad}}) : \text{CH}_{2,\text{ad}}$ ratio from 130 to 193 K. By 210 K, the further dissociation of $\text{CH}_{2,\text{ad}}$ is sufficiently fast for SCAC measurements to capture heats related only to forming $\text{CH}_{\text{ad}} + \text{H}_{\text{ad}}$ (i.e., reaction (2) only). No gaseous reaction products that leave the Pt(111) surface such as C_2H_4 and CH_4 were observed in our simultaneous QMS measurements at 210 K. This is in agreement with what has previously been observed in TPD studies of CH_2I_2 and CD_2I_2 on Pt(111), which reported peaks for these gases only above 230 K^{109, 145}. The second trend with increasing reaction temperature in Fig. 4.4 is that the apparent saturation coverage of the initial high-heat adsorption process also increases.

The complicated reaction kinetics of $\text{CH}_{2,\text{ad}}$ decomposition apparently results in the observation of only a fraction of that reaction occurring during the timescale of our heat measurements at these intermediate temperatures, with possible further diffusion and reaction occurring more slowly than our heat measurements (i.e., on timescales >1 s). Because the dissociation of one CH_2I_2 blocks 8 Pt atoms when it makes $\text{CH}_{2,\text{ad}}$ and even more when it makes CH_{ad} , it requires a large, adsorbate-free area to dissociate to $\text{CH}_{2,\text{ad}}$ and even more for CH_{ad} . Since molecular CH_2I_2 is rather weakly adsorbed, it probably diffuses rapidly even at 100 K, so

that if it lands initially in an area with insufficient free sites to dissociate to $\text{CH}_{2,\text{ad}}$, it can diffuse to other sites and try again. Thus, dissociation to $\text{CH}_{2,\text{ad}}$ is not poisoned very quickly with coverage. The situation is quite different to further make CH_{ad} from $\text{CH}_{2,\text{ad}}$, since $\text{CH}_{2,\text{ad}}$ and the 2 I_{ad} are strongly adsorbed and will not diffuse away rapidly. Our DFT calculations gave a diffusion activation barrier for I_{ad} of 22/23 kJ/mol (optB86b/PBE), which corresponds to a hopping time of ~ 1 s at 100 K, assuming a prefactor of $k_{\text{B}}T/h$ ($= 2 \times 10^{12}/\text{s}$). This is considerably slower than the measurement time of ~ 100 ms. The barrier for $\text{CH}_{2,\text{ad}}$ diffusion was estimated to be 89 kJ/mol³³, so that is even slower. Thus, the 2 I_{ad} can self-poison the local sites needed for that same $\text{CH}_{2,\text{ad}}$ to dissociate starting even at the lowest coverage, at 100 K and to some extent at higher temperatures. The diffusion of these species gets faster with increasing temperature, so the extent of reaction is expected to increase with temperature, as indeed observed in Fig. 4.4.

The fact that the 2 I_{ad} co-products might be localized quite near to the $\text{CH}_{2,\text{ad}}$ that is made at 100 K implies that the heats measure at 100 K may reflect repulsions between the $\text{CH}_{2,\text{ad}}$ and its two I_{ad} neighbors even in the limit of lowest coverage, as noted above. To estimate the magnitude of this effect, we calculated the dissociative adsorption energy of CH_2I_2 to make $\text{CH}_{2,\text{ad}}$ coadsorbed with two atomic I_{ad} at several different coverages (Fig. 4.9). The dissociative adsorption of CH_2I_2 to make $\text{CH}_{2,\text{ad}} + 2 \text{I}_{\text{ad}}$ is exothermic by 452/354 kJ/mol (optB86b/PBE) in the zero-coverage limit, whereas the experimental heat is exothermic by 222 kJ/mol (Fig. 4.2). Thus, the experimental heat of formation and bond enthalpy for $\text{CH}_{2,\text{ad}}$ in Table 4.1 at the limit of zero coverage is probably greatly destabilized compared to truly isolated $\text{CH}_{2,\text{ad}}$ due to repulsive interactions with nearby I_{ad} , and this destabilization at 100 K amounts to 230/132 kJ/mol by comparing the experimental and DFT results. Furthermore, Fig. 4.9 yields the differential dissociative adsorption energies from DFT as $\Delta E = (450-1028\theta)$ kJ/mol (optB86b) and (354-

12300) kJ/mol (PBE), based on which the mutual destabilization between the $\text{CH}_{2,\text{ad}}$ and 2I_{ad} can be as high as 226/135 kJ/mol at 0.22/0.11 ML (optB86b/PBE) vs. the zero-coverage limit. Thus the extent of the mutual destabilization in the experiment could be well above 100 kJ/mol, depending upon how far the 2I_{ad} can move away from the $\text{CH}_{2,\text{ad}}$ when they are co-produced.

The enthalpies of formation and bond energies reported here are the first calorimetric measurements at low coverages of $\text{CH}_{2,\text{ad}}$ and CH_{ad} on a Pt(111) surface (albeit in the former case with 2I_{ad} as close neighbors). Table 4.2 provides comparisons to various DFT calculated bond energies of the $\text{CH}_{2,\text{ad}}$ and CH_{ad} species to Pt(111). A small amount ($= RT$) was subtracted from the bond enthalpies estimated in Figs. 4.7 and 4.8 in order to compare to theoretical predictions of bond energies at 0 K. Our measurements are seen to be in excellent agreement with reported DFT results for CH_{ad} .

The heat of formation of CH_{ad} was also estimated in previous calorimetry work by our group from the heat of dissociative adsorption of CH_3I at 320 K and saturation coverage⁴⁴. This gave a heat of formation 104 kJ/mol above the value measured in this present paper in the limit of low coverage at 210 K. This is not surprising considering the very strong repulsive interactions between adsorbates and corresponding strong coverage dependences of the adsorbate energies shown in Table 4.1 and the present DFT calculations.

Combining this study with previously reported calorimetric measurements of $\Delta H_{\text{f}}(\text{CH}_{3,\text{ad}})$ on Pt(111) by our group^{44,48}, and previous studies by TPD⁵⁷ and temperature-programmed XPS (TPXPS)^{110, 111}, it is now possible to construct a complete enthalpy landscape for methane dehydrogenation on Pt(111) as shown in Fig. 4.10. The landscape is referenced to the enthalpy of gas-phase methane as the zero of energy (which is 75 kJ/mol lower than the elements in their standard states¹⁴³). The enthalpy of formation of adsorbed methane on Pt(111) was taken to be -

90.1 kJ/mol, using its desorption energy of 15 kJ/mol measured by TPD at half-saturation⁵⁷. The calorimetric measurement condition for CH_{3,ad}, CH_{2,ad}, and CH_{ad} are also labeled in Fig. 4.10.

Additionally shown in Fig. 4.10 is an energy level for CH_{2,ad} + 2H_{ad}, estimated from the measurements of Papp et al.^{110, 111} of the kinetics of dehydrogenation of adsorbed methyl on Pt(111) (produced by dissociative adsorption of a fast methane molecular beam) using TPXPS. They observed the activation energy for the decomposition of CH_{3,ad} to CH_{ad} + 2 H_{ad} to be 61 kJ/mol. (This number is slightly corrected from the number (70.6 kJ/mol) given in the paper by Papp et al. by using a prefactor of 10¹¹ s⁻¹ instead of the value of 10¹³ s⁻¹ they assumed, since 10¹¹ s⁻¹ is now believed to be a better estimate of the prefactor for such reactions¹⁴⁶.) Since this decomposition must go via CH_{2,ad} + H_{ad} as an intermediate state, this activation barrier sets an upper limit for the energy of CH_{2,ad} + H_{ad} relative to CH_{3,ad}. Adding this number to the energy of CH_{3,ad} + H_{ad} gives an estimate of 47 kJ/mol for the maximum possible formation energy for CH_{2,ad} + 2 H_{ad} from CH_{4,g}. Note that this number is 144 kJ/mol below the corresponding number of 191 kJ/mol that would be estimated based on our heat of formation of CH_{2,ad} (with 2 I_{ad} nearby) from the heat of dissociative adsorption of CH₂I₂ at 100 K in Table 4.1. This difference is attributed to the fact that the CH_{2,ad} made here from CH₂I₂ decomposition at 100K is not in its energetically most favorable state due to strong repulsions from and between the two nearby iodine adatoms that are simultaneously produced (see above).

Methylene is seen to be very unstable relative to other observed alkyl products; and, methylidyne is seen to be largely downhill in energy from the other CH_x fragments, making it the most stable surface intermediate. The relative stability ranking of the CH_x species on Pt(111) observed in this report (i.e., CH_{ad} + 3H_{ad} > CH_{3ad} + H_{ad} > CH_{2ad} + 2H_{ad}) is in excellent agreement with previous studies.^{109, 110, 117} The energy landscape also agrees with a TPD study carried out

by White *et al.*¹⁴⁵, where the dehydrogenation of the product of adsorbing CD_2I_2 ($\text{CD}_{2,\text{ad}}$) was found to occur at lower temperature than the dehydrogenation of the product from CD_3I ($\text{CD}_{3,\text{ad}}$) on Pt(111).

Our DFT results (Fig. 4.6) are also consistent with an alternative interpretation of our calorimetric measurements at 100 K. As mentioned above, the activation barrier for the initial C-I bond scission in $\text{CH}_2\text{I}_{2,\text{ad}}$ is $E_{a,1}=31/27$ kJ/mol (optB86b/PBE). While this is a small barrier, kinetically the process would still be slower at 100 K than the heat measurement time if this barrier is in this 27-32 kJ/mol range. We also calculated the molecular adsorption of CH_2I_2 at 1/16 and 1/9 ML and determined the differential energy of molecular adsorption of CH_2I_2 to be (204-4950) kJ/mol (optB86b), which is in close agreement with the measured differential heat of (222-4800) kJ/mol at 100 K (Fig. 4.2). Furthermore, the large difference between the optB86 and PBE values for the CH_2I_2 adsorption energy (89 kJ/mol; see Table 4.2), can be attributed primarily to vdW interactions, which are included in optB86. Interestingly, this difference is essentially identical to the multilayer heat of adsorption of CH_2I_2 (89 kJ/mol; Fig. 4.2). Thus the measurements at 100 K may predominantly correspond to molecular, not dissociative, adsorption of CH_2I_2 . The reason we do not prefer this model is that Trenary's group reported clear experimental evidence for the production of $\text{CH}_{2,\text{ad}}$ at 85 K upon adsorption of CH_2I_2 ¹⁰⁹. It is possible that this $\text{CH}_{2,\text{ad}}$ was stabilized by the high coverage used in that experiment, which could have blocked the sites needed for the further dissociation of this $\text{CH}_{2,\text{ad}}$. If the activation barrier for the initial C-I bond scission $\text{CH}_2\text{I}_{2,\text{ad}}$ is overestimated in DFT by only 8 kJ/mol, its rate would be fast at 100 K, consistent with our preferred interpretation.

For completeness, let us consider the alternate model in more detail, that $\text{CH}_2\text{I}_{2,\text{ad}}$ is the product at 100 K. Our DFT estimate of the activation barrier for its initial C-I bond scission is

27-31 kJ/mol. This requires to a temperature of 141-162 K for the time constant for this process to equal the heat measurement time of ~ 100 ms. This is not too far above the temperature of 125 K where a new process first becomes obvious in the heat measurements compared to the result at 100 K (see Fig. 4.4). As mentioned above, the activation barriers both for the C-I bond scission in CH_2I and for the C-H bond scission in CH_2 are lower than this first activation barrier according to DFT. Therefore, according to DFT, CH_2I_2 adsorption would yield CH_{ad} , 2I_{ad} , and H_{ad} once the temperature is high enough to cleave its first C-I bond, at least in the low-coverage limit, and when I_{ad} can rapidly diffuse away to create free sites needed for C-H cleavage. The overall reaction energy for this dissociative adsorption process is calculated to be 508/416 kJ/mol (optB86b/PBE; cf. Fig. 4.6) at the zero-coverage limit, with the optB86b value close to the experimental heat of 533 kJ/mol measured at 210 K. Thus the DFT results for the molecular and dissociative adsorption energies of CH_2I_2 , especially using the optB86b functional, are in close agreement with the measured adsorption heats at 100 and 210 K, respectively, within this alternate model. In either interpretation model, however, $\text{CH}_{2,\text{ad}}$ as a stable, *isolated* species is *not* produced in the zero-coverage limit. If $\text{CH}_{2,\text{ad}}$ is produced, as in our preferred model, it is necessarily confined to areas of high (local) surface coverage. Another DFT result that favors the alternate (less-favored) model is our observation that the $\text{CH}_{2,\text{ad}}$ and 2I_{ad} spontaneously (i.e., without any barrier) moved further apart than in either Figs. 4.5(f) or (g) when placed in a larger unit cell (not shown or discussed above), which implies that such repulsive local coverage situations would not be maintained. Thus, our preferred model implies either that DFT misses some small barrier that prevents these adsorbates from separating at 100 K, or that they are generated in a high local coverage situation even at very low average coverage, perhaps due to attractions between the molecularly adsorbed precursors that cause them to island before

dissociating. Such islanding seems unlikely, given the adsorbate-adsorbate repulsions apparent from the decrease in adsorption energy of $\text{CH}_2\text{I}_{2,\text{ad}}$ with coverage calculated with DFT (see Table 4.2 and above). The main reason we prefer the model where $\text{CH}_{2,\text{ad}} + 2 \text{I}_{\text{ad}}$ is produced at 100 K is that this reaction was observed by vibrational spectroscopy to occur already at 85 K by Deng et al.¹⁰⁹

The complication that the $\text{CH}_{2,\text{ad}} + 2 \text{I}_{\text{ad}}$ co-products remain so close together on the time scale of the heat measurement that they destabilize each other by a large amount highlights a problem that is common not only in SCAC but also in all other transient calorimetry techniques, such as standard solution-phase titration calorimetry. That is, one is not always able to produce more stable desired products on the time scale of the heat measurement, due to kinetic limitations. This can also be an advantage, however, when one wants to study the less stable species that are produced first. In all transient calorimetry techniques, knowing what is produced on the time scale of the heat measurement can prove to be an experimental challenge. In the case of SCAC, this refers to whatever surface spectroscopies are used to analyze the products (or were used in prior papers that led to the SCAC measurements). Our ability to vary the surface temperature in SCAC has proven valuable in matching SCAC temperatures to produce what is known from the prior experimental literature. However, just as it proved to be in this case, computational chemistry can also be a very important aid in determining what is produced on the calorimetry time scale.

Conclusions

CH_2I_2 was used to produce adsorbed methylene and methylidyne on a Pt(111) single crystal surface. The heats of adsorption were measured at six temperatures between 100 K and 210 K using SCAC and were used to calculate the heats of formation and bond energies for both

adsorbed fragments. At 100 K, the $\text{CH}_{2,\text{ad}}$ product is greatly destabilized by coadsorbed iodine atoms at near-neighbor sites, so an activation energy from TPD data in the literature was used to put an upper limit on the heats of formation of isolated $\text{CH}_{2,\text{ad}}$. At 210 K surface diffusion of iodine atoms is sufficiently fast that the coadsorption of iodine with CH_{ad} and H_{ad} are able to reach their most energetically favorable state, which at 0.04 ML approximates isolated CH_{ad} on a Pt(111) surface. DFT calculations for isolated $\text{CH}_{2,\text{ad}}$ and $\text{CH}_{2,\text{ad}}$ coadsorbed with I_{ad} suggest that coadsorption even at relatively low coverages can result in very strong repulsions, which can explain the large difference between the SCAC-derived stability of $\text{CH}_{2,\text{ad}}$ produced from CH_2I_2 with two I_{ad} nearby at 100 K and the stability of isolated $\text{CH}_{2,\text{ad}}$ on Pt(111) calculated with DFT. On the other hand, the stability of CH_{ad} produced from CH_2I_2 estimated by SCAC at 230 K (where the I_{ad} are able to rapidly diffuse away) is in close agreement with DFT. A complete enthalpy landscape for stepwise methane dehydrogenation on Pt(111) was constructed, where methylidyne was found to be the most stable alkyl fragment and methylene the least stable. This ranking of stability is in good agreement with what has been previously observed qualitatively from experiments using a wide variety of techniques and computational methods.

Tables and Figures

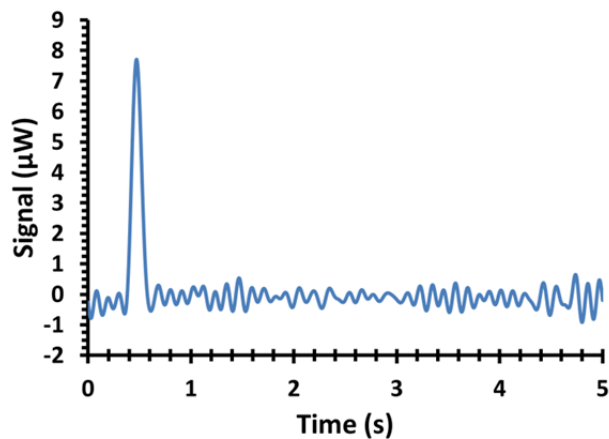


Figure 4.1. Typical deconvoluted heat versus time plot for a single 100 ms gas pulse that occurs at ~ 0.45 s on this scale. The method of deconvolution is explained in the text. Integration of the signal (μW) over time (s) yields the total adsorption energy (μJ) for that pulse. Discussion of the best choice of integration time-window is given in the text.

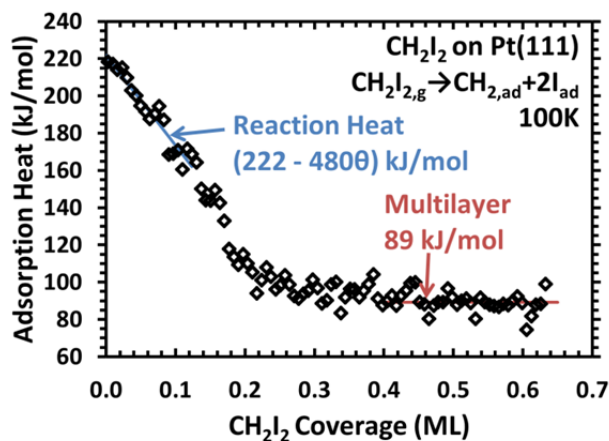


Figure 4.2. Differential heat of adsorption of CH_2I_2 on Pt(111) at 100 K as a function of total CH_2I_2 coverage (θ). Dissociation to $\text{CH}_{2,\text{ad}} + 2 \text{I}_{\text{ad}}$ occurs in the first 1/8 ML with a heat of (222-480 θ) kJ/mol. Continued dosing leads to adsorption in a second layer and then multilayer, with the heat of adsorption eventually approaching the bulk heat of sublimation for $\text{CH}_2\text{I}_{2,\text{s}}$ at 100K (measured to be 89 kJ/mol, estimated to be 87 kJ/mol from bulk thermodynamic values, see text).

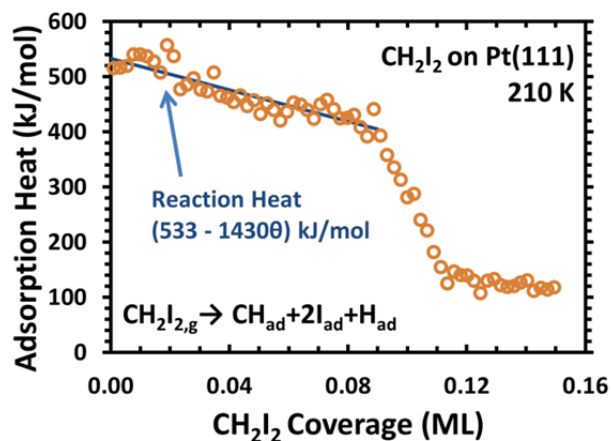


Figure 4.3. Differential heat of adsorption of CH_2I_2 on Pt(111) at 210 K as a function of total CH_2I_2 coverage (θ). Dissociation to $\text{CH}_{ad} + 2\text{I}_{ad} + \text{H}_{ad}$ occurs in the first 0.09 ML with a heat of (533-14300) kJ/mol. Continued dosing leads to adsorption in a second layer on top of the layer of fragments and atomic species. The long-term sticking probability measurements, not shown, show a rapid drop from unity to zero between 0.15 ML and 0.18 ML.

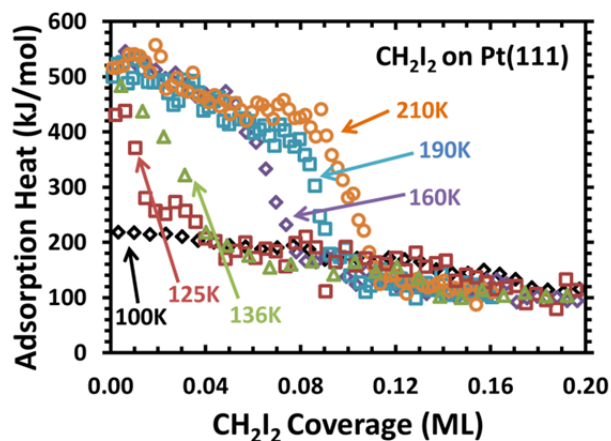


Figure 4.4. Summary of the differential heats of adsorption of CH_2I_2 on clean Pt(111) as a function of total CH_2I_2 coverage measured at different temperatures. These data are interpreted as follows (see text): At 100 K, adsorption produces $\text{CH}_{2,\text{ad}}$ plus 2 I_{ad} in near-neighbor sites. At 210 K, dissociation to $\text{CH}_{\text{ad}} + 2 \text{I}_{\text{ad}} + \text{H}_{\text{ad}}$ occurs in the first 0.09 ML. Increasing temperature above 100 K results in an increasing fraction of further decomposition of $\text{CH}_{2,\text{ad}}$ to $\text{CH}_{\text{ad}} + \text{H}_{\text{ad}}$, which is enabled by the increasing extent of diffusion of I_{ad} away from the near-neighbor sites of $\text{CH}_{2,\text{ad}}$, thus producing free Pt sites needed for $\text{CH}_{2,\text{ad}}$ decomposition (see text).

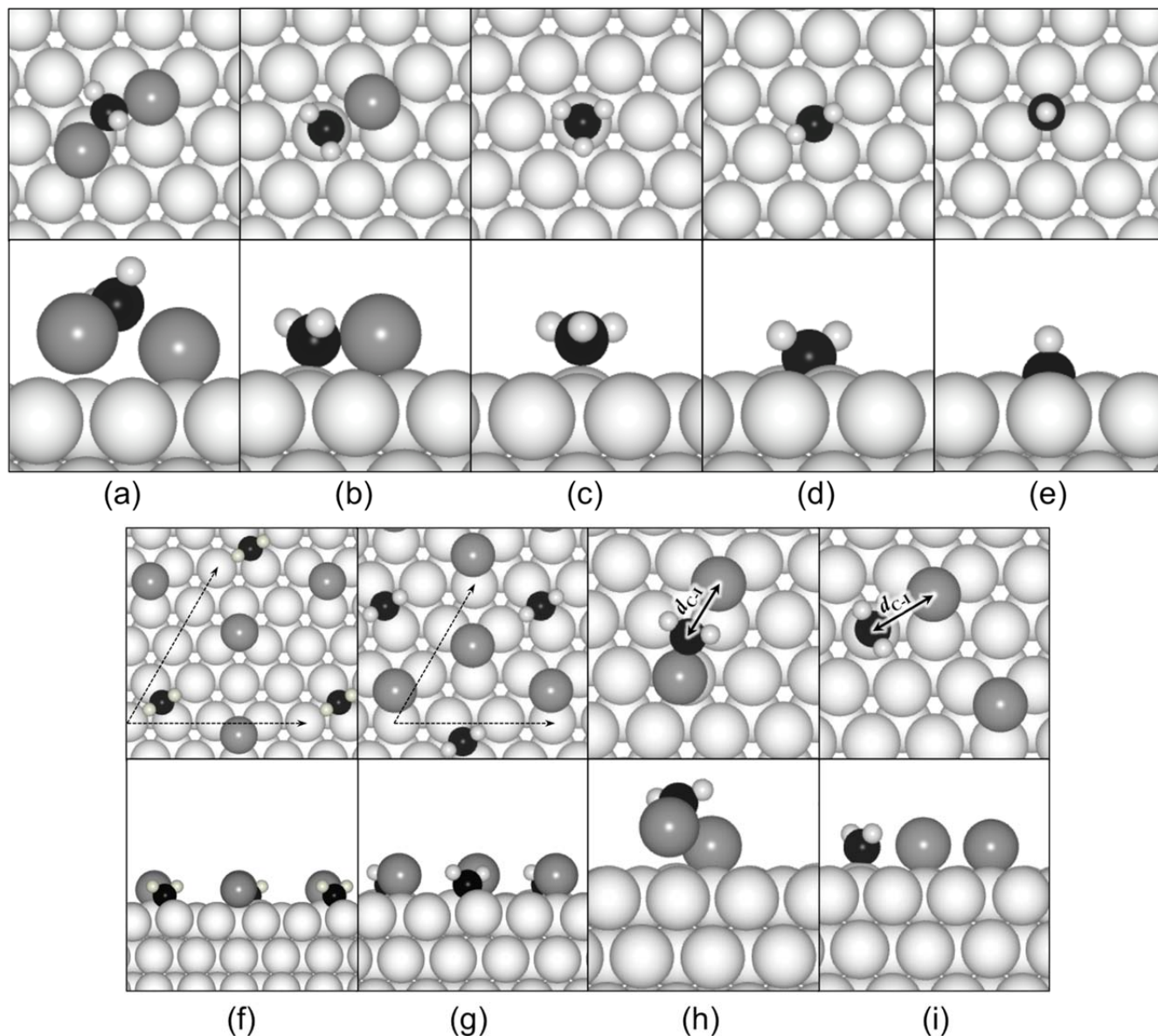


Figure 4.5. Top (upper panels) and side (lower panels) snapshots of the DFT (optB86b vdW-DF) calculated minimum-energy configurations for the various species adsorbed on Pt(111): (a) CH_2I_2 ; (b) CH_2I ; (c) CH_3 ; (d) CH_2 ; (e) CH ; (f-g) CH_2+2I ; and the transition states for C-I bond scission in (h) $\text{CH}_2\text{I}_{2,\text{ad}}$ and (i) $\text{CH}_2\text{I}_{\text{ad}}$ coadsorbed with one I_{a} . Large white, large grey, medium black, and small white spheres represent Pt, I, C, and H atoms, respectively. The coverage is 1/16 ML for (a-e), and 1/16 ML for (f, h, i) and 1/9 ML for (g), respectively, referring always to the starting amount of CH_2I_2 needed to generate each structure. The surface unit cell vectors are indicated in (f) and (g) for the (4×4) (corresponding to 1/16 ML) and (3×3) (corresponding to 1/9 ML) surface unit cells, respectively. The C-I bond distance ($d_{\text{C-I}}$) at the two transition states are: (h) 3.180 Å; (i) 3.034 Å.

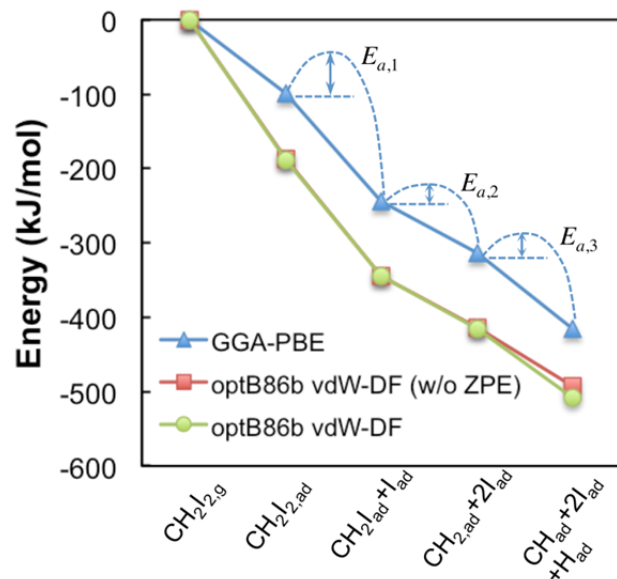


Figure 4.6. DFT-calculated reaction energy profile for the dissociative adsorption of $\text{CH}_2\text{I}_{2,\text{g}}$. Points 2-4 are each calculated on a (4×4) surface unit cell, whereas the last point is calculated with each adsorbate on a separate (4×4) surface unit cell, approximating the zero-coverage limit. The numberings of the three activation barriers for the successive decomposition of $\text{CH}_2\text{I}_{2,\text{ad}}$ to CH_{ad} are indicated, as referred to in the text.

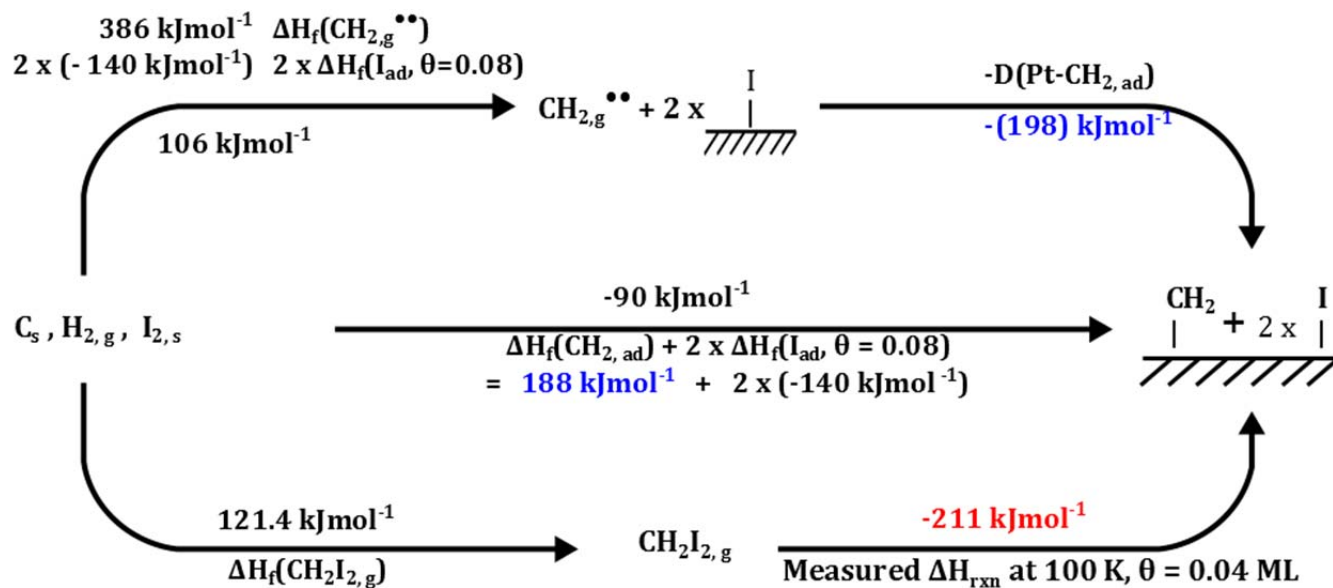


Figure 4.7. Thermodynamic cycle for the formation of adsorbed methylene on Pt(111) (with two nearby I_{ad}) from $\text{CH}_2\text{I}_{2,\text{g}}$ at 100 K, used to estimate the standard heat of formation and bond enthalpy of $\text{CH}_{2,\text{ad}}$ to Pt(111). The measured number reported in red is the integral heat of adsorption up to a coverage of 0.04 ML from Fig. 4.1. Numbers in blue are calculated, and numbers in black are taken from literature as described in the text. This heat of formation is strongly affected by the presence of two nearby I_{ad} (see text).

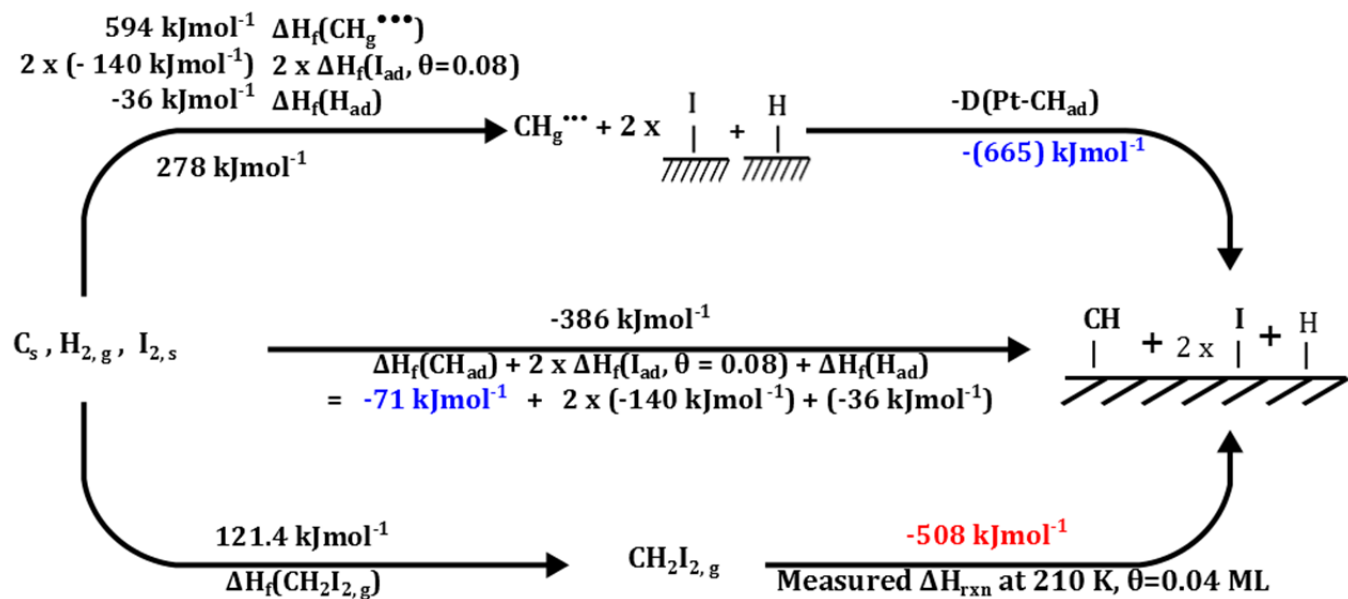


Figure 4.8. Thermodynamic cycle for the formation of methylidyne on Pt(111) from CH_2I_2 at 210 K, used to estimate the standard heat of formation and bond enthalpy of CH_{ad} to Pt(111). The measured number reported in red is the integral heat of adsorption up to a coverage of 0.04 ML from Fig. 4.3. Numbers in blue are calculated, and numbers in black are taken from literature as described in the text.

Table 4.1. Best-fit lines for experimental differential heats of adsorption, heat of formation, and bond enthalpies versus coverage for various fragments on Pt(111). Coverages here are defined for each reaction listed as the number of reactant species (CH_2I_2 , CH_3I , or I) adsorbed on the surface of the Pt(111) single crystal divided by the number of Pt atoms on the Pt(111) surface ($1.5 \times 10^{15}/\text{cm}^2$). Heat of adsorption determined by calorimetry for the reactions listed except for I_{ad} , which values come from TPD. Heats of formations were calculated using the integral heat of adsorption (differential heat of adsorption integrated over the stated coverage range) together with known enthalpies from the literature, as explained in Figs. 4.6 and 4.7. The numbers given here are from integration of the differential heat of adsorption's linear fit given in the 3rd column. (The data presented elsewhere in the paper come from numerical integration of data points.)

Adsorbate and reaction measured	Coverage Range (ML)	Differential Heat of Adsorption (kJ/mol)	Heat of Formation (kJ/mol)	Bond Enthalpy (kJ/mol) Coverage-integrated	Reference
CH_{ad}	0-0.09	533-14300	-79.6+3170	674-3170	this paper
$\text{CH}_2\text{I}_{2,\text{g}} \rightarrow \text{CH}_{\text{ad}} + 2 \text{I}_{\text{ad}} + \text{H}_{\text{ad}}$					
$\text{CH}_{2,\text{ad}}$ (near 2I_{ad})*	0-0.12	222-4800	195-1580	191+1580	this paper
$\text{CH}_2\text{I}_{2,\text{g}} \rightarrow \text{CH}_{2,\text{ad}} + 2 \text{I}_{\text{ad}}$					
$\text{CH}_{3,\text{ad}}$	0-0.045	233-9530	-70.3+3770	217-3770	48
$\text{CH}_3\text{I}_{\text{g}} \rightarrow \text{CH}_{3,\text{ad}} + \text{I}_{\text{ad}}$					
I_{ad}	0-0.33	255-1990	-148+990	255-990	134
$\text{I}_{\text{g}} \rightarrow \text{I}_{\text{ad}}$					
Calculated**					
optB86b	0.06-0.33	306-1490		306-740	this paper
PBE	0.03-0.33	258-1480		258-740	this paper

* The $\text{CH}_{2,\text{ad}}$ species here is destabilized by two I adatoms in near-neighbor sites even at the lowest coverage, so its zero-coverage enthalpies do not reflect isolated species. Due to adsorbate-adsorbate repulsions even near zero coverage that are not properly considered in calculating the apparent coverage dependences of its heat of formation and bond enthalpy, the values listed here are probably incorrect, even going in the wrong direction with coverage (see text).

** The DFT calculated values for I_{ad} are ZPE-corrected.

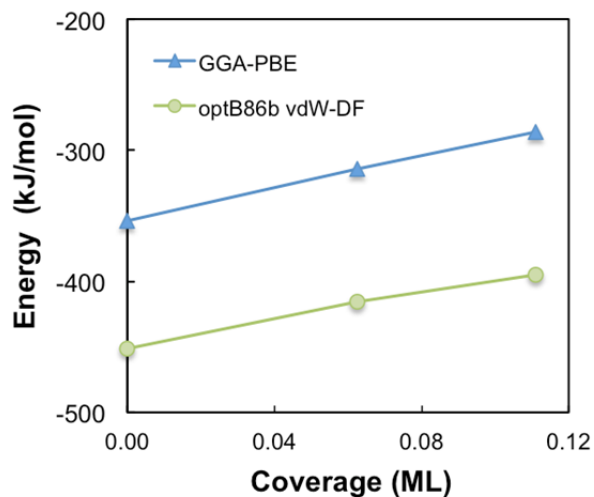


Figure 4.9. DFT-calculated differential dissociative adsorption energy of $\text{CH}_2\text{I}_{2,g} \rightarrow \text{CH}_{2,\text{ad}} + 2\text{I}_{\text{ad}}$ as a function of total dissociated CH_2I_2 coverage. The zero-coverage limit is approximated with each product calculated on a separate (4×4) surface unit cell.

Table 4.2. Comparison of experimentally measured bond energies of adsorbates to Pt(111) with DFT calculations

Species	Method or DFT functional	Coverage or cluster size	Bond energy (kJ/mol)	Reference
CH_{3,ad} (top)	SCAC (from CH ₃ I)	0.04 ML CH _{3,ad} with 0.04 ML I _{ad}	197	⁴⁸
	PBE	1/16 ML	195, 179 _{ZPE}	this paper
	optB86b	1/16 ML	232, 216 _{ZPE}	this paper
	PW91	1/4 ML	197	³³
	RPBE	1/4 ML	163	³³
CH_{2,ad} (bridge)	SCAC	0.04 ML, destabilized by 2 I _{ad} nearby	197	this paper
	From TPXPS ¹¹¹ : CH _{3,ad} dissociation barrier (sets limit of minimum stability)	0.04 ML (coverage where activation barrier for CH _{3,ad} → CH _{ad} + 2H _{ad} is measured)	≥338	this paper, see text for details
	PBE	1/16 ML	398, 378 _{ZPE}	this paper
	optB86b	1/16 ML	439, 419 _{ZPE}	this paper
	PBE	1/9 ML	392	⁵⁵
	PW91	1/4 ML	381	³³
	RPBE	1/4 ML	336	³³
	B3LYP	Pt ₃₅ cluster	400	¹⁴⁷
	B3LYP	Pt ₁₀ cluster	406	¹⁴⁸
	PW91	Pt ₁₀ cluster	440	¹⁴⁸
B3LYP	Pt ₈ cluster	436	¹⁴⁹	
CH_{ad} (fcc hollow)	SCAC (from CH ₂ I ₂)	At 0.04 ML, with 0.04 ML H _{ad} + 0.08 ML I _{ad}	663	this paper
	SCAC (from CH ₃ I)	At 0.11 ML CH, with 0.18 ML I _{ad}	549-568	⁴⁴
	PBE	1/16 ML	644, 624 _{ZPE}	this paper
	optB86b	1/16 ML	657, 637 _{ZPE}	this paper
	PBE	1/9 ML	643	⁵⁵
	PW91	1/4 ML	620	³³
	RPBE	1/4 ML	569	³³
	B3LYP	Pt ₃₅ cluster	613	¹⁴⁷
	B3LYP	Pt ₁₀ cluster	678	¹⁴⁸
	PW91	Pt ₁₀ cluster	728	¹⁴⁸
B3LYP	Pt ₈ cluster	697	¹⁴⁹	

CH₂I_{2,ad}	PBE	1/16 ML	98, 100 _{ZPE}	this paper
	optB86b	1/16 ML	188, 189 _{ZPE}	this paper
	optB86	1/9 ML	175, 177 _{ZPE}	this paper
CH₂I_{ad} (C_{top}- I_{bridge})	PBE	1/16 ML	242, 230 _{ZPE}	this paper
	optB86b	1/16 ML	315, 303 _{ZPE}	this paper

Bond energies are calculated by subtracting RT from the bond enthalpies, such as those listed in Figs. 4.6 and 4.7. All DFT calculations were performed on various Pt(111) surface models, and the subscript “ZPE” indicates that this energy includes a zero-point energy correction.

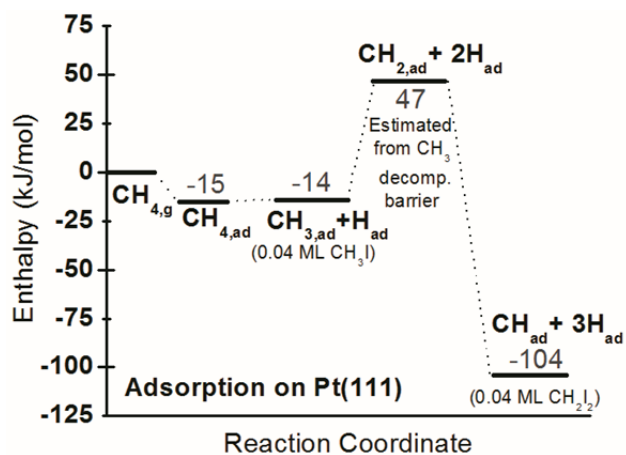


Figure 4.10. Experimental enthalpy landscape for stepwise dehydrogenation of methane on Pt(111) at low coverage. Adsorbing gas and its total coverage used for SCAC measurements are indicated in parentheses under each species. For other species, see text for citations.

Chapter 5: Energetics of Adsorption of D₂O on Fe₃O₄(111) and NiO(111)

Chapter Abstract

While a great deal of data has been gained from SCAC about adsorbed on Pt(111) surfaces, very little work has been done to study adsorbates on other surfaces whose irreversible adsorption (e.g., dissociative adsorption) demand the SCAC approach, particularly oxides. This chapter will provide a brief look at the study of D₂O adsorption on Fe₃O₄(111) and NiO(111). This work was aimed at trying to measure the heat of formation of hydroxyl species on these surfaces, which proved quite challenging due to possible problems with the literature and inadequately pure vacuum for one very demanding experiment. This chapter's report is expected to aid in the completion of this work under future graduate students.

Introduction

Metal oxides are a class of materials which are important in a wide variety of fields including catalysis, environmental science¹⁵⁰, and materials science¹⁵¹. In catalysis metal oxides play a role as both structural support¹⁵² and as catalysts themselves¹⁵³ and there has been a tremendous amount of effort to understand the strong metal support interaction (SMSI)^{154, 155} which has been observed in many nanoparticle on oxide systems to improve catalytic activity. Because of the complexity of working with oxide surfaces much less concrete information about adsorbate species on oxide surfaces is available than is available on metal surfaces. Particularly lacking is information on the energetics of various molecular fragments on these surfaces, which are important catalytic intermediates in catalytic reactions. While some work has been done studying adsorption energetics on powdered oxides¹⁵⁶, few studies have focused on the adsorption energetics of single crystal surfaces which have well defines site/adsorbate systems. An improvement in the understanding of such fundamental quantities as adsorption energy will

go a long way to aid in rational catalyst design, as well as providing benchmarks for the latest computational methods to check their absolute accuracy.

Iron oxide is a classic example of a metal oxide with a wide variety of applications in all of the aforementioned fields, particularly catalysis. In surface science of catalysis, iron oxide is used as a model oxide surface to explore the role of acid-base sites, the effects of surface oxidation/reduction, and as a support material for nanoparticle catalysis¹⁵⁷⁻¹⁶³, where it was observed that gold adsorbed as adatoms onto the oxygen sites of Fe₃O₄(111) and CO bonds only to those adatoms and not to larger Au nanoparticles¹⁶⁴. Further studies suggested that these Au adatoms suggested that they were cationic^{164, 165}. Other work showed that on Au/FeO_x, the highest activity was seen in bilayer Au nanocrystals containing ~10 atoms which also appeared to be cationic¹⁶⁶. In practical catalysis, iron oxide is used as both support and catalyst itself for reactions such as the conversion of ethylbenzene to styrene in the presence of steam^{167, 168}. Iron oxide catalysts have also been studied as potential catalysts for the water gas shift reaction¹⁶⁹. It has also been studied as a potential photocatalyst for water splitting¹⁷⁰.

A great deal of work has been done to study crystalline iron oxide thin films (<10nm) grown on Pt(111)¹⁷¹ under ultrahigh vacuum (UHV) conditions as a well-defined model for surfaces in more practical applications in catalysis. Such films have been characterized using x-ray photoelectron spectroscopy (XPS)¹⁷², Auger electron spectroscopy (AES), ultraviolet photoelectron spectroscopy (UPS), low energy ion scattering spectroscopy (LEIS), X-ray adsorption spectroscopy (XAS), low energy electron diffraction (LEED)¹⁷³, scanning tunneling microscopy (STM)¹⁷⁴, and a variety of less common surface science technique^{171, 175}. It has been found that iron oxide initially grows as a monolayer of FeO(111) before building up into magnetite, Fe₃O₄(111), upon further Fe deposition and annealing in the presence of 1x10⁻⁶ mbar

O₂. The transition to the more oxidized α -Fe₂O₃(111) structure has been found to only occur when annealing at partial pressure of oxygen near ambient (~ 1 mbar) levels¹⁷¹. The thin films of Fe₃O₄(111) grown on Pt(111) show a surface termination consisting of a hexagonal close packed layer of oxygen (density = 1.3×10^{14} O/cm²) covered with $\frac{1}{4}$ monolayer (ML) of Fe atoms located at three fold hollow sites with a surface density of 3.3×10^{14} Fe/cm². The iron atoms act as acid sites while the $\frac{1}{4}$ ML of oxygen atoms not adjacent to an iron atom act as base sites.

Water adsorption on iron oxide is relevant in nearly every application in which iron oxide is used. Water adsorption on magnetite (111) has been well studied by a variety of groups using temperature programmed desorption (TPD), ultraviolet photoelectron spectroscopy (UPS)¹⁷⁶, x-ray photoelectron spectroscopy (XPS), high resolution electron energy loss spectroscopy (HREELS)¹⁷⁷, reflection adsorption infrared spectroscopy (RAIRS)¹⁷⁸, scanning tunneling microscopy (STM)¹⁷⁹, and many other techniques^{171, 180, 181}. Unlike many nonpolar oxide surfaces, these studies have shown that the magnetite surface is highly reactive and that water adsorbs dissociatively on Fe₃O₄(111) surfaces. Hydroxyls adsorb at the surface iron sites and the remaining proton from dissociation is believed to rest on the undercoordinated lattice oxygen atom. Further dosing of the surface results in molecular water adsorption which interacts with the adsorbed hydroxyl species and surface oxygen.

Platinum is a ubiquitously studied material for catalysis at all scales, but it is far from the only metal used in catalysis. Nickel, another group 10 element, is much more common and therefore substantially cheaper than platinum and has been extremely well studied as a metal catalyst. Ni based catalysts are widely used in industrial catalysis for a variety of reactions including reforming of alcohols, hydrogenation, hydrocracking, and oxidation processes^{1, 182, 183}.

As was the case with platinum, there is little directly measured information available about the energetics of adsorption of molecular fragments on Ni surfaces.

While nickel catalysis is nearly as ubiquitous as platinum catalysis, nickel is not nearly as noble a metal as platinum. Therefore nickel oxides are also a material of intense study for catalysis. Aside from the fundamental understanding which would be gained from studying a variety of metal oxide surfaces, NiO is used as a catalyst for high temperature fuel cells¹⁸⁴ and is expected to exist in many high temperature oxidation reactions occurring over a nickel catalyst¹.

Epitaxial NiO(111) films can be grown on Ni(111) single crystals by annealing in a background of oxygen, and these serve as a well-defined model of NiO surfaces in more practical applications. Such films can grow to be 3 layers thick at high (~600K) temperatures and low (~300K) temperatures^{185, 186} before oxygen transport limitations prevent further growth. Because NiO grows in a rock salt structure the (111) face is polar and unstable in a planar configuration due to divergent dipoles. To stabilize the surface NiO(111) films undergo a surface reconstruction to a (2x2) NiO(111)/Ni(111) structure which creates a three dimensional octopole structure on the surface¹⁸⁷⁻¹⁸⁹. Because of this instability the NiO(111) surface tends to be more reactive than the NiO(100) surface.

On NiO(111) water adsorption is known to produce hydroxyls^{190, 191} as well as cause a surface restructuring^{192, 193}. Dosing water on a clean (2 x 2) NiO(111) surface results in the production of hydroxyls and a surface restructuring to a (1 x 1) structure. Heating these hydroxylated films above 600 K results in a return to the (2 x 2) clean structure^{190, 192, 194, 195}. These findings were also observed using DFT¹⁹⁶. There is some disagreement about the coverage of hydroxyls expected in literature. Kitakatsu et al.¹⁹¹ report 0.85 ML OH coverage using quantitative XPS analysis, while Langell et al.¹⁹⁵ report anywhere from 0.63 to 0.84 ML OH

coverage using quantitative XPS. Cappus et al.¹⁹⁰ used EELS and TPD of water and NO in an attempt to quantify the amount of hydroxylation on a NiO(111)/Ni(111) surface and found that 2/3 of the surface sites were hydroxylated.

Experimental details

Experiments were performed in a stainless steel UHV chamber (base pressure $< 2 \times 10^{-10}$ mbar) equipped with XPS, AES, LEIS, LEED, quadrupole mass spectrometry (QMS), liquid nitrogen cooled molecular beam, and SCAC. This apparatus and the procedures for SCAC have been described in detail previously⁴². For further details on SCAC experiments and instrumentation see Chapter 2.

Growth of Fe₃O₄(111) Film

A Fe₃O₄(111) thin film was grown on a 1 μm thick Pt(111) single crystal which had been cleaned by cycles of sputtering with 1.25 kV Ar⁺, annealing at 1123 K for 1 min, and annealing to 873 K in 1×10^{-8} mbar of O₂ for 2 min. After each cycle the cleanliness of the sample was checked using AES until no carbon residue is detected. The order of the cleaned Pt(111) surface was confirmed by LEED with a clear hexagon pattern. Iron oxide films were grown on the clean single crystal using the method of Zscherpal et al¹⁹⁷ by first depositing 1 ML of Fe then oxidizing at 1000K in 1×10^{-6} mbar O₂. Iron was then deposited in 1×10^{-7} mbar O₂ at room temperature until a film approximately 4 nm thick had been grown. Film thickness was determined by measuring the Fe deposition rate with a QCM. The film then underwent a final anneal in oxygen at 1000K and film cleanliness, composition, and order were checked using XPS, AES, and LEED. The sample was cleaned between individual SCAC experiments by flashing to 1000K in 5×10^{-7} mbar O₂. One ML is defined using the surface density of O atoms of 1.5×10^{15} O/cm².

Growth of NiO(111) Film

NiO(111) films were epitaxially grown on a 1 μm thick Ni(111) crystal. The Ni(111) sample was first cleaned by repeated cycles of sputtering with 1.25 keV Ar⁺ ions and annealing at 1000K. The cleanliness and order of these Ni(111) films was checked using AES and LEED. Once the Ni(111) sample was cleaned, NiO(111) films were prepared by heating the sample to 570K and exposing the surface to 1000L of O₂, followed by a final flash to 650K in vacuum, as in accordance with the method given by several papers from the group of H.-J. Freund^{190, 192} and also used by the group of Hirose and Domen¹⁹⁸⁻²⁰⁰ to study D₂O, CO₂, and formic acid on NiO(111)/Ni(111) surfaces. Sample composition was checked using AES, but the films grown were highly defective and no clear LEED pattern could be seen, which has been previously observed in the literature¹⁹². NiO(111) samples were flashed immediately before each experiment in vacuum to a temperature of 1000K to ensure sample cleanliness.

Experimental Procedure for Measuring Heat of Adsorption of D₂O on Oxide Surfaces

SCAC was performed by dosing D₂O vapor onto the surface through the molecular beam with a typical backing pressure of ~1.7 mbar resulting in an approximate flux of 0.02 ML per pulse, with each pulse being 102 ms in duration. There was a five-second delay between pulses to avoid adsorption/reaction overlap. D₂O with purity 99.9+ atom % D was supplied by Sigma Aldrich and was purified by repeated freeze pump thaw cycles. The flux of the beam was measured using a liquid nitrogen cool quartz crystal microbalance (QCM). The temperature of the dosing gas was 300K, and was controlled by heating a glass capillary array (GCA) which collimated the beam.

The heat released by the adsorption of each pulse of D₂O was measured using a pyroelectric polymer ribbon gently pushed to the backside of the sample. The sensitivity of the pyroelectric ribbon was calibrated using a HeNe (632.8 nm) laser with known energy for each

individual experiment. Experiments were performed with the sample cooled using a liquid nitrogen cryostat. Calorimetric measurements versus coverage at each temperature were repeated at least 5 times and the average values are reported.

D₂O on Fe₃O₄(111) Results

Experiments were conducted at 90 K to determine the multilayer heat and calibrate our heat data. It is expected that the reflectivity of our surface would decrease slightly from the pure platinum value of 0.76 as the thickness of Fe₃O₄ on the surface increases²⁰¹. Because the precise reflectivity of our sample is not known and cannot be measured in situ in our instrument, the heats of adsorption were normalized by setting the heat of adsorption of D₂O to make a thick multilayer film of D₂O(solid) at 90K equal to the value of 47.2 kJ/mol measured in a previous study by our group but on Pt(111)⁴³, which also agreed with literature values for the heat of sublimation of bulk D₂O(solid)²⁰². The reflectivity of our sample with a 4nm Fe₃O₄ film calculated using this method is 0.745, extremely similar to the reflectivity of 0.76 of our platinum single crystal⁶⁶.

Figure 5.1 shows the heat of adsorption vs coverage at 90 K. Unity sticking probability was observed at 90 K. On the timescale of our measurements (102 ms) only molecular adsorption is observed at this temperature. The data shows three distinct regions. An initial layer of molecular water adsorbing on the surface is observed up to 1 ML. This suggests that water is likely bonding with the surface oxygen through a hydrogen bonded network. The heat data then shows the development of a second layer up to 2 ML, suggesting the second layer is built in a layer-by-layer mechanism growing with the same surface density as the of lattice oxygen lattice. From there further dosing eventually reaches the multilayer heat of 47.2 kJ/mol.

Experiments were performed at higher temperatures as well and the heat of adsorption at 150 K is shown in Figure 5.1. At 150 K slightly higher heats were observed (~10 kJ/mol) than at

100K and the long-term sticking fraction was observed to drop to 0 at 1ML D₂O coverage. At still higher temperatures (160K to 220K) the heats were identical to those measured at 150K and the sticking fraction was seen to drop extremely rapidly as summarized in Table 5.1, resulting in no substantial build-up of adsorbates on the surface. In addition to these heats being much lower (~30 kJ/mol) than expected³⁶, this runs very counter to the previous observations in literature of hydroxyls being stable on the surface up to 280K^{176, 177, 203}. These results suggest that we are not forming hydroxyls on the surface at any coverage/temperature tested.

D₂O on NiO(111)

Experiments were conducted at 100K to measure the multilayer heat, which is identical to the heat of sublimation of water which is known. The flux of water was observed to drop slowly throughout the day and due to instability in the QCM, flux measurements could not be made between each experiment. When working up data, the molecular beam flux at the end of the run was assumed to be the value that gave a heat adsorption for the multilayer at 90 K to have the correct value. At 150K no multilayer was formed so we could not normalize the flux to the multilayer. Instead the sticking data was used, normalizing the flux so to give the same coverage at the point of the sharpest drop in long term sticking probability for each experiment. At higher temperatures, experiments were much shorter due to the rapid drop to zero sticking probability, and the flux was not observed to drop significantly between experiments.

Adsorption of D₂O on NiO(111) was performed at a variety of temperatures between 90 and 220 K shown in Figure 5.2. Higher temperature experiments were conducted at 300K and 320 K, but because of the extremely low saturation coverage (< .02 ML) are not included in Figure 5.2. The initial heats of adsorption measured were found to be largely similar, and only the sticking probability seemed to change as temperature increased, as shown in Figure 5.3. A

notable exception to this observation of identical heats was at 150K, where the same initial heat was observed as at 100K, but then a subsequent more significant drop in heat of adsorption was seen than at 100K, followed by eventually reaching the multilayer heat. This difference was most likely due to large the heat capacity of adsorbed water⁴³.

These results run very counter to the previous observations in literature of ~0.6-0.85 ML coverage of hydroxyls on NiO(111) being produced at temperatures as low as 300 K and stable up to as high as 600 K.^{190, 191, 195} This coverage would correspond to a coverage of ~0.3 - 0.425 ML in Figure 5.3 assuming each water produces 2 hydroxyls on the surface. Both the low heat and low sticking probabilities suggest it is much more likely only molecular adsorption is occurring in our experiment.

D₂O on Fe₃O₄(111) Discussion

The observed heats and sticking fraction for D₂O on Fe₃O₄(111) as a function of coverage and temperature show fairly low heats out to a coverage of 1 monolayer of D₂O, where a monolayer is defined at the surface density of O atoms ($ML_O = 1.3 \times 10^{14}/cm^2$) of coverage. At 100K the heats remain slightly high for what appears to be the growth of a second layer between 1 ML and 2 ML coverage before eventually reaching the sublimation heat at higher coverage. These initial, low coverage heats of 56.9 kJ/mol are considerably below the 89 kJ/mol expected for -OD on Fe₃O₄(111) from TPD³⁶, and are much more in line with what is expected from TPD of molecularly adsorbed water on top of a hydroxylated surface^{36, 176, 204}, which should have an adsorption energy around 50 kJ/mol. Additionally the hydroxyl species should only form on the Fe cations, which occupy ¼ ML of the surface, so a break in the heat versus coverage curve would be expected at ¼ ML coverage, not 1 ML. The sticking probability versus coverage plots are not shown, but unity sticking is observed at 100 K at all coverages. At 150K near unity

(>0.9) sticking probability is seen up to 1 ML_O at which point the sticking probability rapidly drops to zero. At higher temperatures (>175K) no sticking is seen at any coverage. Considering that the reported desorption temperature for molecular D₂O on Fe₃O₄(111) was observed in TPD to be ~190 K and the dissociated hydroxyl species (which should exist in a coverage range up to ¼ ML_O) is not observed to desorb until ~280 K, this further supports the idea that only molecular D₂O adsorption was observed in our experiments.

Table 5.2 shows a comparison between current, previous, and some theory results for the energetics of adsorption D₂O on Fe₃O₄(111). The DFT numbers presented in Table 5.2 are merely a sample of a larger pool of DFT literature related to water adsorption on the magnetite (111) surface^{179, 205-208}. Good agreement is seen with TPD results for molecular water, though DFT appears to be overbinding the species.

The most likely explanation for not seeing the formation of hydroxyls formation on the Fe₃O₄(111) surface is that the surface was already hydroxylated before the experiments began. Isobaric equilibrium adsorption experiments showed that you can make OH at temperatures as low as 100 K²⁰⁴. Weiss et al also showed using isobaric equilibrium adsorption measurements the formation of hydroxyls when cooling from high temperature in the presence of oxygen, suggesting a water mediated precursor was not necessary to produce the hydroxyl species²⁰⁴, unlike what had been reported by Thornton et al. who saw that an intermolecular mechanism of dissociation was needed to produce hydroxyls²⁰⁹. The most likely source of hydroxylation occurring prior to the beginning of experiments reported in this chapter is trace amounts of residual water vapor impurity produced by reactions with the vacuum chamber wall of the O₂ gas introduced during the flash immediately before the experiment begins. This procedure had been adopted to prevent possible reduction of the surface, but other groups showed that this was not

necessary and that it could in cause a buildup of O on the surface Fe sites in the case of bulk $\text{Fe}_3\text{O}_4(111)$ crystals^{174, 210}, though whether or not this behavior is seen in $\text{Fe}_3\text{O}_4(111)$ thin films is debated^{177, 211, 212}. Other common background impurities such as CO gas may also have reacted with the Fe sites needed for water dissociation and passivated them. Another possibility is that the surface hydroxylated species would not completely desorb from simple annealing, with the work of Kendelewicz et al.¹⁸⁰ reporting that annealing up 973K was insufficient to thermally clean the hydroxylated $\text{Fe}_3\text{O}_4(111)$ surface, and that Ar^+ sputtering was necessary to remove the OH groups.

Before experiments could be performed to test different surface preparation methods, it was discovered at the 2013 American Vacuum Society meeting in Long Beach, CA that the group of Shauermann et al. at the Fritz-Haber-Institut der Max-Planck-Gesellschaft had already performed this experiment and measured the heat of adsorption of hydroxyls on a $\text{Fe}_3\text{O}_4(111)$ surface and that a publication of these results would be forthcoming. Because of this discovery, it was elected to abandon further experiments of D_2O adsorption on $\text{Fe}_3\text{O}_4(111)$.

D_2O on NiO(111) Discussion

The initial heats observed at all temperatures are not consistent with the observation in literature that hydroxyls are easily produced on the surface by dosing water at T as low as 300 K and remain stable up to 600K. Using a simple Redhead TPD type analysis where we assume a prefactor¹⁴⁶ of 10^{17} s^{-1} and a fast heating rate of 50 K/s during the flash, we can ballpark the expected heat of adsorption for such a stable species (i.e., with a peak desorption T of 600 K) to be $\sim 190 \text{ kJ/mol}$, well above the highest heat we observed (74 kJ/mol).

At 150 K the heat deposition profile has the same initial heat as at 100K, but then drops lower than the 100 K heat curve at D_2O coverages between 0.2 and 1.2 ML before eventually

leveling out near the multilayer heat. Despite this unexpected change in heat of adsorption behavior from what was seen at 100K, the adsorption is still interpreted to consist entirely of molecular adsorption on the surface and at no point are hydroxyls forming as was expected. Lew et al.⁴³ previously observed a lower initial heat for molecular adsorption of D₂O on a clean Pt(111) surface which was attributed to a high heat capacity of adsorbed water molecules. The heat capacity was calculated by taking the difference in the integral heat of adsorption of D₂O in the first 1 ML on clean NiO(111) at 100K and 150K (=6.9 kJ/mol). This number is then corrected for the difference in enthalpy of D₂O gas (=1.7 kJ/mol), and is then divided by the 50 K temperature difference. Lew et al. calculated the heat capacity of adsorbed D₂O on Pt(111) as 130 ± 82 kJ/mol. Analyzing the data for adsorbed D₂O on NiO(111), we arrive at a heat capacity of 171 ± 107 kJ/mol (both error bars represent 95% confidence), quite similar to that of Lew et al. considering the large error bars.

At higher temperatures of 220K, 300K, and 320K (temperatures above 220K not shown in Figure 5.2) identical heats of adsorption were seen as those at low coverage at 100 and 150K as shown in Figure 5.2. The sticking probability begins to drop off rapidly at temperatures above 150K as shown in Figure 5.3. Previous literature suggests that roughly one monolayer of hydroxyls should form on the surface and should be stable up to 600K. This low sticking probability at higher temperatures is then further consistent with the hypothesis that we are only observing molecular adsorption at all temperatures.

The cause of not seeing hydroxyl formation is most likely due to a similar phenomenon as was suspected in the case of D₂O on Fe₃O₄(111), that the surface is already hydroxylated or otherwise passivated with adsorbed impurities before SCAC experiments begin. Whereas in Fe₃O₄(111) the most likely culprit was in the sample cleaning procedure, the cause here is more

murky. The extremely high instability of the hydroxyl free NiO(111)/Ni(111) films reported in literature suggest that actually obtaining a clean surface is very tricky¹⁹³. Rohr et al. observed that over long periods of time the clean NiO(111) surface will scavenge residual water from the background of the chamber to form the hydroxylated surface¹⁹². In order to ensure this was not the case for us, great care was taken to ensure an extremely low base pressure. Additional pumping was achieved by adding additional cryopumping by cooling a large copper block in the chamber which houses the TSP with liquid nitrogen. While a slightly lower base pressure was observed ($<1 \times 10^{-10}$ mbar), no difference was observed in collected SCAC data under these conditions.

In addition to already being hydroxylated there is some evidence in the literature that NiO films grown epitaxially on Ni(111) may not grow in an ordered (111) structure. Christensen et al.²¹³ observed the formation of large, thick NiO(100) islands after oxidizing a Ni(111) single crystal at 473 K. Similarly Kitakatsu et al.^{191, 214} observed that oxidation of Ni(111) single crystals at 500 K resulted in a surface that was predominantly (93%) covered by NiO(100) with only a small fraction (7%) being small triangular NiO(111) grains. Maurice et al. also observed that these NiO(100)/Ni(111) surfaces did not adsorb hydroxyl groups on regular sites, but possibly did on defects, in agreement with what was previously seen in literature for NiO(100) surfaces¹⁹⁰. However, Maurice et al. also observe that upon further heating to 550K the NiO(100) oxide decomposes to a Ni(111)-(2 x 2)O adsorbed phase, though the NiO(111) islands remain intact. For NiO films grown initially at lower temperatures (300K), Maurice et al. observe that some hydroxylated NiO(111) islands form, and then grow and coalesce when heated to 700K, but they do not observe the hydroxyl free surface.

Conclusions

D₂O on Fe₃O₄(111)

Our study of the heat of adsorption of D₂O on an Fe₃O₄(111) thin film observed only molecular adsorption. The surface of Fe₃O₄(111) was likely already hydroxylated or passivated by adsorbed impurity before experiments began due to the sample preparation procedure, or possibly simply due to the difficulty in removing hydroxyls from the surface¹⁸⁰. Before further experiments could be run to test a different sample preparation, it was discovered at the 2013 American Vacuum Society national meeting in Long Beach, CA that the group of Schauermann et al. at the Fritz-Haber-Institut der Max-Planck-Gesellschaft had already performed this experiment and measured the heat of adsorption of hydroxyls on a Fe₃O₄(111) surface and that a publication of these results would be forthcoming. Because of this discovery, it was elected to abandon further experiments of D₂O adsorption on Fe₃O₄(111).

D₂O on NiO(111)

The observations seen for the adsorption of D₂O on NiO(111) clearly do not support the previous observations in literature that hydroxyls should form on the surface up to a coverage of ~1 ML and be stable up to 600K. The results are much more consistent with molecular adsorption of water on the surface, possibly because the surface is already hydroxylated or passivated by adsorbed impurity, or because we somehow otherwise did not have the clean NiO(111) surface we expected^{191, 213, 214}. Further studies of D₂O and other adsorbates such as formic acid^{198, 199, 215, 216} on NiO(111) are expected to continue under future graduate students.

Figures and Tables.

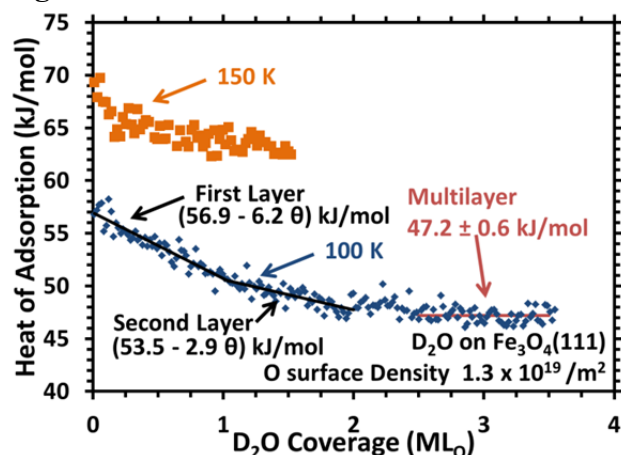


Figure 5.1. Heat of adsorption of D_2O on $Fe_3O_4(111)$ at 100K as a function of D_2O coverage. Surface of $Fe_3O_4(111)$ believed to already be hydroxylated before dosing begins. Adsorption is believed to be molecular D_2O adsorption on top of hydroxyls. Break is seen at 1 ML coverage and at 2 ML coverage suggesting growth of first and second layers. Heat eventually reaches the heat of sublimation at ~ 2.5 ML which is also the multilayer heat. Data is normalized to heat of sublimation in multilayer region because reflectivity of $Fe_3O_4(111)$ film is unknown and has been seen to depend on thickness as discussed in the text. The heat of adsorption of D_2O at 150 K is seen to be ~ 10 - 15 kJ/mol higher than at 100K in the first ML. The explanation for this is unclear, but it could be that the water molecules are more mobile at 150 K and are able to find more energetically favorable sites to adsorb. At 150 K no sticking is seen beyond ~ 1.25 ML of D_2O coverage and no multilayers are formed.

Temperature (K)	Saturation Coverage
100	Multilayers formed
150	1.25
160	1
175	0.1
190	0
220	0

Table 5.1. Summary of ultimate saturation coverage for D₂O on Fe₃O₄ calculated using sticking probabilities measured simultaneous to calorimetric measurements.

Method	Coverage	Reaction Products $\text{H}_2\text{O}_g + \text{Fe}_3\text{O}_4(111) \rightarrow$	ΔH_{rxn} (kJ/mol)	Ref.
SCAC	1 ML	$\text{D}_2\text{O}_{\text{ad}}$ (associative)	-54	This data
TPD	1/4 ML	$\text{H}_2\text{O}_{\text{ad}}$ (associative)	-50	²⁰⁴
DFT	1/4 ML	$\text{H}_2\text{O}_{\text{ad,Fe}}$ (associative)	-79	¹⁷⁹
DFT	1/4 ML H+OH with 1/4 ML H_2O	H_2O adsorbed with surface hydroxyls	-75	²⁰⁶

Table 5.2. Comparison of experimental results of this paper with TPD and DFT numbers for molecular (associative) adsorption of water on $\text{Fe}_3\text{O}_4(111)$. SCAC data reported is the integral heat in the first monolayer of D_2O coverage.

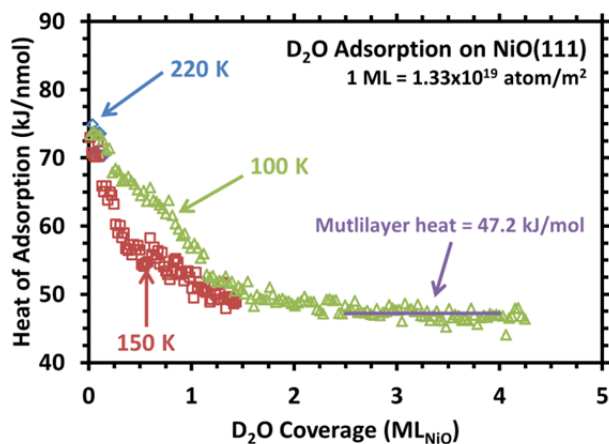


Figure 5.2. Heat of adsorption of D₂O on NiO (111) at different temperatures as a function of D₂O coverage. Surface of NiO(111) believed to already be hydroxylated before dosing begins. Adsorption is believed to be molecular D₂O adsorption on top of hydroxyls. Break is seen at 1 ML coverage at 100K, where heat of sublimation (which is equal to the multilayer heat) is reached. Data is normalized to heat of sublimation in multilayer region because reflectivity of NiO(111) film is unknown. Experiments performed at higher temperatures (150K) yielded similar, though slightly lower heat curves out to 1 ML, at which point the sticking probability dropped to 0. The slightly lower heat is attributed to the heat capacity of water as discussed in the text. Going to still higher temperatures (>220K) resulted in identical heats, but lower sticking probability even at zero coverage.

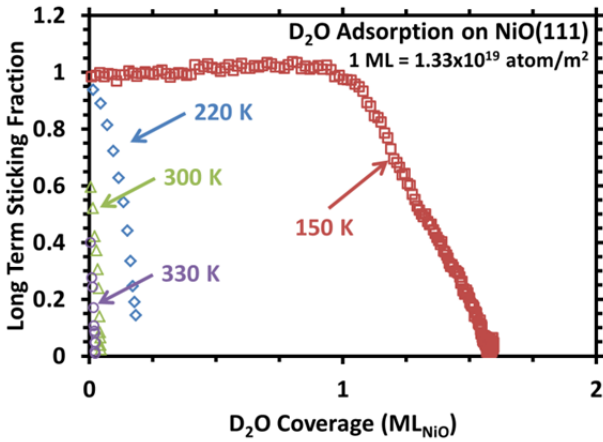


Figure 5.3. Sticking probability for D₂O on NiO(111) as a function of D₂O coverage and temperature. 100K sticking probability is 1 at all coverages, and is not shown. Break at 1 ML of coverage at 150K is similar to what has been observed for water on other surfaces where multilayers are not formed. Higher temperatures result in smaller coverages being reached before sticking probability becomes 0.

Chapter 6: Degree of Rate Control Approach to Computational Catalyst Screening

Chapter Abstract

A new method for computational catalyst screening that is based on the concept of the degree of rate control (DRC) is introduced. It uses the energies of the species in the reaction mechanism (i.e., adsorbed intermediates and transition states) with the highest degrees of rate control for the best reference catalyst as descriptors for estimating the rates on similar materials and identifying what materials are expected to have higher activity. This method relies upon the definition of the degree of rate control to calculate the change in net rate for a given reaction based upon the changes in energy (relative to the reference catalyst) of a small number of key intermediates and transition states. The predictions of this method regarding the relative rates of twelve late transition metals for methane steam reforming are compared to previous results by Xu et al. who studied this system using the more commonly-used descriptor approach developed by Nørskov and Bligaard (the bond energies of the surface to C and O atoms and linear scaling relations that give the energies of all other species from these). This comparison was made using the same input energies calculated from density functional theory (DFT) and the same mechanism for both approaches. The degrees of rate control for each species was determined using the Rh(211) surface as the reference catalyst. The relative rates on (211) faces of eleven other metals were then calculated. It is found that this new method shows excellent quantitative agreement with the rate predictions of the more common descriptor approach of Nørskov and Bligaard when the metals are relatively similar to the reference metal (descriptors <40 kJ/mol different), provided the same energies are used as input. In these cases, this new approach is far simpler to implement when screening a moderate number of materials (<100), since it does not require developing linear scaling relations. It is also more accurate, since it does not require

using this linear-scaling approximation, and instead can use numbers calculated directly by DFT for each descriptor energy. For example, the adsorption energy for CO on Ir is an outlier in the linear scaling relation, so the rate for Ir is predicted to be >300-fold higher from linear scaling than by using the direct DFT number for this key energy. Even when the descriptors of the new metal differ from the reference metal by 130 kJ/mol, the method still provides qualitative agreement with that by the Nørskov-Bligaard approach, but is no longer nearly quantitative, and when the descriptors differ by >200 kJ/mol, this new approach fails badly. This is because the degrees of rate control change too much (relative to the reference metal for which they were calculated) when changing these descriptors by such huge amounts. Thus, this new approach is a complimentary tool to the approach by Nørskov and Bligaard, but cannot replace it.

Introduction

There is no single “best” algorithm for developing an improved catalyst. This is unfortunate as the ubiquity of catalysis in modern chemical processes means that even minor improvements in catalyst performance could result in massive improvements in process performance^{1, 2, 54}. In many emerging areas like green energy and green materials, the room for improvement is great and an improvement in catalyst performance could make the difference between a feasible idea and infeasible one.

One method for finding better catalysts has been high-throughput experimental screening of many materials for their catalytic performance (activity, selectivity, lifetime)²¹⁷. However, this is costly, and with the evolution of ever faster computational methods that can more and more accurately predict catalytic reaction rates for different materials³¹, one expects that computational pre-screening of materials for catalytic activity or selectivity to find the best candidates for experimental testing will soon become a faster route to the discovery of new catalysts. Indeed, there have already been some successes in using high-throughput

computational screening to accelerate the discovery of new catalysts^{32, 34, 218, 219}. We describe here a new approach for computational screening of new catalysts that relies on the Degree of Rate Control (DRC) to help identify descriptors for estimating reaction rates on new materials. We show that it is faster than the most widely used method, and has some advantages in better accuracy for rather similar materials, but is not as accurate when treating dissimilar materials.

Perhaps the most successful method for computational screening of solid catalysts, and the most widely used, has been the method developed by Nørskov and Bligaard^{28, 29, 31, 50, 218, 220}, which relies on the following approach to calculate the rate or selectivity on a new material:

1. Determine the reaction's mechanism on a good known catalyst in a certain class of materials through a combination of experiment and theory. We will refer to this as the reference material (RM).
2. Develop a microkinetic model for that mechanism that can reproduce experimental measurements of the reaction rate for that reference material to all the products of interest at a variety of conditions, but relies on knowing the energies of all the adsorbed intermediates and transition states involved in every elementary as it occurs on that RM.
3. Assume that the same mechanism as the RM applies on all materials in this class.
4. Estimate all the needed energies for the new material based on a few "descriptors", which most frequently have been the adsorption energies of O and C atoms on the surface, using linear scaling relations that have been developed from trends in computational energies derived from quantum mechanics (such as density functional theory). These linear plots relate the energy of every adsorbed intermediate or transition state to the energies of these few descriptors. These descriptor energies are calculated for this new material by quantum mechanics.

5. Use these energies to calculate the rate for the new material to every product at the desired reaction conditions. Typically a microkinetic model requires the energies of more than 10 adsorbed intermediates and 10 transition states, and these are estimated using only two descriptors that are an order of magnitude faster to calculate than a transition state, so this can reduce the quantum mechanics' computational time needed to calculate rates on a new material by a factor of 100, provided the linear scaling relations are already in place.
6. Repeat 3-5 for all the new materials to be screened, and generate a volcano plot of rates versus descriptors' energies.

An example volcano plot generated by this procedure is shown in Fig. 6.1 for methane steam reforming on late transition metal surfaces, where the descriptors are the adsorption energies of O and C atoms. It will be discussed in more detail below.

Here, we use an alternate approach to the method outlined above which focuses instead only on the most relevant energies that most sensitively determine the catalyst's activity. This can significantly simplify the analysis of reactions in any multi-stepped catalytic reaction mechanism, like methane reforming, since a small change in the energy of any particular intermediate or transition state energy usually does not have any significant effect on the reaction rate, which is instead sensitive to only a few of these species' energies⁵³. It is therefore reasonable to assume that one can simplify computational screening by identifying a small number of rate-controlling species (intermediates and transition states) whose energies most strongly effect the reaction rate, and develop a screening model based on these energies alone.

A rigorous method of identifying the extent to which each species' energy affects the net reaction rate to any product (or the rate of consumption of any reactant) was developed by

Campbell et al.⁵³ called the degree of rate control. The degree of rate control of any such species i (which could be any intermediate or any transition state) is defined as:

$$X_i = \left(\frac{\partial(\ln r)}{\partial \left(\frac{-G_i}{RT} \right)} \right)_{G_{j \neq i}}, \quad (6.1)$$

where r is the rate to the product of interest at the chosen reaction conditions, and G_j is the standard state Gibbs free energy of species j . In general, X_i depends on the reaction conditions. For simple mechanisms where one can derive an analytical rate expression that applies at certain reaction conditions where there is a single rate-determining step, one finds that the degree of rate control of the transition state (TS) for the rate determining step is 1.0, and the sum of X_i over all transition states (TSs) is 1.0²²¹. There are, however, only a few TSs with X_i not close to zero²²²,²²³. Similarly, there are only a few adsorbed intermediates with X_i not close to zero, and the sum of X_i over all adsorbed intermediates is a small negative integer²²⁴⁻²²⁶.

By thus quantifying the impact that changing the free energy of a particular species in a reaction landscape will have on net reaction rate, it is straight forward to see that any species whose degree of rate control has a large magnitude can be categorized as a “rate-controlling” species. By shifting the focus from the kinetics of a small number of reaction steps to the standard state free energy of a small number of chemical species, it is substantially more straightforward to determine what to look for when trying to find an improved catalyst. This is especially true since the entropy contribution to the standard state free energy of the same adsorbed species differs very little across different materials^{146, 227}, whereas the zero-point energy contribution dominates its differences in standard state free energies between different materials.

Thus, instead of looking for a catalyst with a faster rate directly, all that is necessary is to identify a catalyst with improved zero-point formation energies for a small number of species. For example, when there is a single rate-determining transition state, one wants a material that

lowers its formation energy, and when there is a single rate-determining intermediate which blocks most surface sites, one wants to raise its energy. Things become more complicated when there is a branching pathway to undesired products, where one wants to instead increase the energy of the most rate controlling TS on that undesired branch.

Let us explain in more detail the most widely-used method for computational catalyst searches developed by Nørskov and Bligaard, discussed above and exemplified in Fig. 6.1. A typical hunt for an improved catalyst comes from the generation of such a volcano plot. Finding what parameters, or descriptors, to use in such a plot is a nontrivial issue³¹. Using density functional theory (DFT), it was found that many adsorbed surface species of the form AH_x , where A is O, S, C, or N, and x is typically between 1 and 3, a linear correlation exists between the M- AH_x bond energy and the M-A bond energy across different materials' surfaces, M ⁵⁰. Taking into account the prevalence of intermediates of the form AH_x in reaction mechanisms, and the existence of other linear correlations for example between the M-CO or M-COH bond energies and the M-C bond energy^{228, 229}, it is possible to use these linear bond energy relationships to estimate the energies of all adsorbed intermediates from a few of the easiest adsorbate energies to calculate. In Fig. 6.1 it is the M-O and M-C bond energies (i.e., the adsorption energies of O and C atoms on the surface). These energies are put into a microkinetic model where the rate is expressed using Arrhenius relationships. Further combining these with Bronsted or Evans-Polyani relationships, which give linear relationships between activation energies and reaction energies for elementary steps^{220, 230}, this also allows the energies of all transition states to be estimated from these few descriptors (M-C and M-O bond energies in Fig. 6.1). Thus, these can be great descriptors and this is a very powerful approach for computational catalyst discovery.

While this linear scaling relationship approach have proven very useful as a fast way to estimate catalyst activity, it has some shortcomings. Most obviously, there exists scatter about each of the linear M-AH_x/M-A relationships due to real errors in assuming that each energy scales linearly with the descriptor(s), leading to inaccuracies in their energy estimates and thus in the rate predictions. If a process contains many different intermediates, the noise introduced by the scatter from each linear relationship for each species might become cumulative, making its resulting rates even less accurate. Additionally because of the large number of species-surface combinations one needs to calculate by quantum mechanics to generate the needed M-A vs M-AH_x, M-CO and other linear scaling relationships, there is a very serious initial cost associated with the large computational time needed, thus limiting the feasibility of using the state of the art, most high accuracy, high computation time DFT techniques to calculate the energies of each species³⁰.

Though somewhat controversial, recently a great deal of attention and effort has been expended to discover and develop new methane reserves around the world from new fracking technologies²³¹. Whether as a potential source of hydrogen through steam reforming^{18, 232} or as a precursor for larger hydrocarbon molecules²³³, methane catalysis will only become more important in the foreseeable future. The performance and more importantly the cost of these catalysts will have a direct impact on how people chose to utilize these new methane reserves. It is also a system that has been thoroughly studied already by the linear-scaling approach described above^{234, 235}. We therefore have chosen this reaction as test system to demonstrate the utility of this new method for searching to find better catalyst materials.

Degree of Rate Control as a Screening Method for DFT

Instead of using select M-A bond energies as the descriptors in the quest to discover new catalysts with DFT based on their linear scaling relations, this paper proposes a new screening methodology which utilizes the concept of the degree of rate control. Instead of searching for materials with appropriate M-A bond energies only after establishing a full set of linear scaling relations of all energies of intermediates and transitions states to the M-A bond energies, we instead immediately focus on the energies of just a few key species in any particular reaction without any need for linear scaling relations.

To derive our screening methodology, we begin with the definition of degree of rate control given in Equation 1. We temporarily convert this from partial derivative to regular derivative for the special case where all the other parameters are constant, yielding

$$X_i = \frac{d(\ln r)}{d\left(\frac{-G_i}{RT}\right)} \quad . \quad (6.2)$$

Rearranging Equation (2) yields

$$X_i * d\left(\frac{-G_i}{RT}\right) = d(\ln r) \quad . \quad (6.3)$$

We can now integrate this over some change in G_i , from the value for some reference catalyst, denoted by a small o , to that for some new catalyst, denoted by a small n . Assuming that X_i remains constant over the range of interest, this gives:

$$X_i * \left(\frac{-G_{i,n} - (-G_{i,o})}{RT}\right) = \int_{r_o}^{r_n} d(\ln r) = \ln \frac{r_n}{r_o} \quad . \quad (6.4)$$

(Later, we address in detail this assumption of constant X_i .) Equation (4) shows the change in the total rate to the product of interest between catalyst o and catalyst n only due to the change in the energy of species G_i and its degree of rate control X_i . This is only true if all other $X_i = 0$ in the reaction. If some number N different species have non-zero X_i then the change in rate is equal to a sum of terms of identical form to the left hand side of Eqn. 4:

$$\sum_{i=1}^N X_i * \left(\frac{-G_{i,n} - (-G_{i,o})}{RT} \right) = \ln \frac{r_n}{r_o} . \quad (6.5)$$

Taking the exponent of both sides of the equation yields:

$$\frac{r_n}{r_o} = e^{\sum_{i=1}^N X_i * \left(\frac{-G_{i,n} - (-G_{i,o})}{RT} \right)} . \quad (6.6)$$

This equation allows one to estimate r_n/r_o for new but similar materials to the reference material. In practice, it is only necessary to perform this sum over all species with non-negligible X_i , which generally is a small fraction of the total species²²²⁻²²⁶. We show below that Eq. (6.6) can be used to computationally search for new catalyst materials which possesses higher activity than the reference material (i.e., $r_n/r_o > 1$), and sort amongst many of these to predict the best materials. Since the degrees of rate control for the reference material can be estimated experimentally as well, it also allows one to search for better materials without even developing a full microkinetic model for the reference material, or even knowing the complete mechanism.

Application of Method to Evaluate Catalysts for Methane Steam Reforming and Comparison to Prior Results by Linear-Scaling Approach

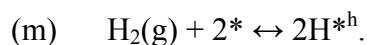
We now validate the utility of this method for catalyst discovery by comparing its predictions of the relative activities (rates) of different metal catalysts for methane steam reforming with the predictions of the more common linear-scaling approach developed by Nørskov, Bligaard et al. discussed above, as applied by Xu et al.²³⁵ to this reaction. To do this, we attempted to use the same exact energies they used, which include the relative energies of all the intermediates and transition states in all the elementary steps of methane steam reforming calculated directly using DFT or derived from linear scaling relationships derived from other DFT calculations. Xu et al. chose to study this reaction over a large number of different FCC

and HCP single crystal catalyst surfaces with a (211) surface geometry, and also probed many alloys. Xu et al. developed a microkinetic model to calculate the net rate of reaction, and constructed volcano plots of turn over frequency (TOF) as a function of M-O and M-C bond energies, including the one shown in Fig. 6.1.

Although Xu et al. probed a variety of experimental conditions and the impact of species-species interaction on modelling; we will focus on a single set of experimental conditions and ignore species-species interactions. These conditions are identical to the “lab scale” conditions used by Xu et al. and are listed in Table 6.1.

The volcano plot from Xu et al. for these conditions is reproduced in Fig. 6.1. The mechanism used by Xu et al. in their microkinetic model is given below, where a * symbol refers to a surface site:

- (a) $\text{CH}_{4(\text{g})} + 2* \leftrightarrow \text{CH}_3^{*\text{t}} + \text{H}^{*\text{h}}$,
- (b) $\text{CH}_3^{*\text{t}} + * \leftrightarrow \text{CH}_2^{*\text{t}} + \text{H}^{*\text{h}}$,
- (c) $\text{CH}_2^{*\text{t}} + * \leftrightarrow \text{CH}^{*\text{f}} + \text{H}^{*\text{h}}$,
- (d) $\text{CH}^{*\text{f}} + * \leftrightarrow \text{C}^{*\text{f}} + \text{H}^{*\text{h}}$,
- (e) $\text{H}_2\text{O}(\text{g}) + 2* \leftrightarrow \text{OH}^{*\text{s}} + \text{H}^{*\text{h}}$,
- (f) $\text{OH}^{*\text{s}} + * \leftrightarrow \text{O}^{*\text{s}} + \text{H}^{*\text{h}}$,
- (g) $\text{COH}^{*\text{t}} + * \leftrightarrow \text{C}^{*\text{f}} + \text{OH}^{*\text{s}}$,
- (h) $\text{COH}^{*\text{t}} + * \leftrightarrow \text{CO}^{*\text{s}} + \text{H}^{*\text{h}}$,
- (i) $\text{CHO}^{*\text{t}} + * \leftrightarrow \text{CO}^{*\text{s}} + \text{H}^{*\text{h}}$,
- (j) $\text{CHO}^{*\text{t}} + * \leftrightarrow \text{CH}^{*\text{f}} + \text{H}^{*\text{h}} + \text{O}^*$,
- (k) $\text{CO}(\text{g}) + * \leftrightarrow \text{CO}^{*\text{s}}$,
- (l) $\text{CO}^{*\text{s}} + * \leftrightarrow \text{C}^{*\text{f}} + \text{O}^{*\text{s}}$,



The kinetic parameters they used for this model can be found in that paper. In the microkinetic model adsorbates may be adsorbed on one of four different sites. the ‘step’ (*s) site corresponds to the upper part of a (211) step site. The ‘four-fold’ (*f) site corresponds to the lower four-fold site of a (211) step. The ‘terrace’ (*t) corresponds to a (211) terrace site. In addition, hydrogen is adsorbed in a special ‘hydrogen reservoir’ site (*h) which has the same energetics as a three-fold hollow site at steps.

In our analysis it was necessary to calculate the degree of rate control of a reference catalyst for each species in the microkinetic model used by Xu et al. at the conditions of Table 6.1. We selected Rh(211) as the “reference” catalyst because it showed one of the highest TOFs at these conditions, but also because, in order for us to do this analysis, it was necessary to have DFT energies for all species (intermediates and transition states), and Rh was a metal for which all these energies were readily available²³⁵⁻²³⁷.

Computational Methods

The microkinetic model of Xu et al. was reconstructed using the the Catalysis Microkinetic Analysis Package (CatMAP) module for Python.²³⁸ . CatMAP allows for the calculation of catalytic rates, as well as the degree of rate control after inputting an energy landscape (i.e., the energies of all the intermediates and transition states). The numbers for our energy landscape were taken from the work of Medford et al.²³⁶ The catalytic rates are calculated using a mean-field kinetic model where lateral adsorbate-adsorbate interactions are neglected. The pseudo-steady-state approximation is employed to solve the resulting set of differential

equations by assuming that the rate of change for all surface intermediates is zero. More details can be found in²³⁸. After obtaining the steady-state solution the degree of rate control is computed by numerical differentiation ($\delta E = 1 \times 10^{-14}$ eV). CatMAP allows for the computation of rates and the degrees of rate control either for any specific metal, as was done for Rh(211), or as a continuous function of the descriptor energies used for all the linear scaling relationships. It also calculates all of the needed linear scaling relationships after a library of s-energies of adsorbate / surface combination is provided as input.

Results

A volcano plot was constructed in an attempt to reproduce the one created by Xu et al. for the conditions of Table 6.1 with no adsorbate-adsorbate interactions, and a comparison to the results from Xu et al. are shown in Fig. 6.1. The model is not an exact replica, but is very close, with TOFs differing by less than an order of magnitude near the peak of the volcano and generally less than two orders of magnitude of the rest of the ranges studied (excepting at especially negative E_{O^*} values). The code used by Xu et al. to generate the plot was unavailable so an exact fit could not be obtained. The differences between the two volcano plots might be explained by differences in the older DFT input energies used to generate the linear scaling relations used here. Alternatively, Xu et al. used homemade code to construct the volcano plot and it is difficult to be certain whether it had some small error. This highlights one potential use of the new CatMAP-based approach: CatMAP is an easy to use, universal software tool for microkinetic modeling²³⁸ which should allow future researchers to exactly reproduce the results of this paper.

Knowing that our model successfully replicated Xu et al., we proceeded to calculate the degrees of rate control for Rh(211) using the formation energies of all species calculated by

DFT. The three species with the highest degrees of rate control for Rh(211) at these conditions were found to be the adsorbed CO intermediate ($X_{\text{CO}^*} = -0.99$), the transition state for the formation of adsorbed CO ($X_{\text{C-O}^*} = 0.98$), and the transition state for dehydrogenation of adsorbed intermediate of atomic carbon ($X_{\text{C}^*} = -0.66$). A complete list of the degree of rate control for all species is given in Table 6.2.

Assuming all other $X_i = 0$ for Rh(211) except the two key species with $X_i > 0.9$, one can directly estimate the rates of other catalysts relative to Rh using Eq. (6.6) together with the energies of the species CO^* and C-O^* as the parameters that define all other materials. The results are shown in Fig. 6.2 as a contour plot. Fig. 6.2 also shows distinct points for eleven of the other specific metal catalysts studied in the report of Xu et al., using the DFT energies of the CO^* and C-O^* species calculated directly by Medford et al.²³⁶ for these different metal (211) surfaces.

Note that Fig. 6.2 is not a volcano plot. As implied by Eq. (6.6) and the values of their degrees of rate control ($X_{\text{CO}^*} = -0.99$ and $X_{\text{C-O}^*} = 0.98$), the rate simply increases exponentially relative to Rh when adsorbed CO increases in energy relative to Rh, and when the transition state for adsorbed C-O dissociation decreases in energy, and the rate decreases exponentially for the opposite changes in their energies. Figure 6.2 is not believed to represent a complete implementation of this method for catalyst screening in this particular case, as this model has three species with large DRCs. Thus a more complete model would require a third dimension to truly capture the reaction with the highest possible quantitative accuracy. The effect of this third dimension is analyzed below (see Fig. 6.3).

Figure 6.2 can be used as a simple guide, requiring only the energies of the CO^* and C-O^* species to predict whether a particular catalyst would be superior to another catalysts. The

main question we aim to address here is: *How do these simpler descriptors perform compared to the more commonly used linear-scaling descriptors of Nørskov/Bligaard if analyzing the same computational set of energies?* We show next that it works as well and even better (i.e., more accurately) than that method, at least for materials that are similar enough to the reference material that they have similar degrees of rate control (i.e., have descriptor energies within 0.3 eV the reference material). We also show that it gives qualitatively correct trends even for materials that differ by ~ 1.3 eV in their descriptor energies relative to the reference material, but can fail miserably when the materials are so different in electronic character that completely different species become most rate controlling (i.e., when descriptor energies differ by >2 eV from the reference material).

Comparing Fig. 6.1 and 6.2, it is clear to see that in the region around the selection of our “reference” catalyst (Rh), there is excellent qualitative agreement between the two methods, as will be shown in detail in Fig. 6.3 below. The further one moves away from Rh however, the more one sees disagreement between the two methods. This is not surprising, as the assumption of constant X_i 's made in deriving Eq. (6.6) does not hold under these extremes. In Fig. 6.1, once E_C has increased by ~ 2 eV or more compared to Rh as is the case for the noble metals Cu, Ag, and Au, then E_{CO^*} increases by more than 1 eV in Fig. 6.2, and adsorbed CO becomes so unstable it will not exist at high concentration on the surface as it does on Rh. Thus the assumption that CO* is rate controlling is no longer correct: the fractional CO coverage (θ_{CO}) and thus X_{CO^*} will be close to zero⁵³. Therefore the assumption that X_{CO^*} has the same value for the noble metals as it does for Rh (-0.99) is not valid when this far from Rh in that direction on Figs. 6.1 and 6.2 (although moving in the opposite direction is not a problem since θ_{CO} stays high there).

Attempting to quantify these changes in accuracy, one must think about how the degree of rate control for an intermediate (in this case CO*) and the coverage of that intermediate are related. The absolute magnitude of X_{CO^*} (0.99) just equals θ_{CO} here, as expected⁵³, and the CO coverage is still low enough to change very sensitively with CO adsorption energy if it is decreased by much. For example, if we assume its coverage is determined by simple first-order adsorption/desorption equilibrium, θ_{CO} will decrease from 0.99 by a factor of ten for every decrease in its desorption energy (increase in E_{CO^*}) of $0.15 \text{ eV} = RT \ln 10$, after the first factor of ten, which requires a larger (0.5 eV) decrease due to the effect of near saturation in CO initially. Due to this, the large decrease in rate due to the change in E_{C-O^*} will not be nearly compensated by the increase from moving far to the right along the E_{CO^*} axis. This effect of moving to the right here is not so strong initially, since the CO coverage of 0.99 is almost saturated. It is also worth pointing out that when extending this model to include the three highest DRC species, the coverage of C* is also equal to its DRC (0.66) because it adsorbs on a different type of site than CO*.

This discussion above exemplifies how to predict where the assumption of similar degrees of rate control on metal surfaces, implicit in Eq. (6.6), might fail. It may fail relatively quickly when one moves along a descriptor axis (i.e., as one changes the energy of a rate-controlling species) in a direction that will decrease the degree of rate control for that species. This is the direction of higher energy (less stability) for adsorbed intermediates, and lower energy (higher stability) for transition states. But Eq. (6.6) will remain accurate much more robustly when changing these energies in the opposite directions.

To be more quantitative about the magnitude of energy changes that are problematic for Eq. (6.6), we break Fig. 6.1 down into three key regions:

- (1) Those species within ~ 0.5 eV of Rh, and thus possess very similar O and C bonding characteristics to Rh, which includes Ni, Ir, Ru, and Co for which Eq. (6.6) works well quantitatively.
- (2) Those species within ~ 1.3 eV which possess similar enough bonding character that Eq. (6.6) is at least qualitatively correct, including Pt, Pd, and Fe. Re straddles this group and the next.
- (3) Those species separated by > 2 eV which possess so little similarity in bonding character to Rh that Eq. (6.6) fails qualitatively, which includes Cu, Ag, and Au.

Figure 6.3 shows this analysis more quantitatively. To improve accuracy from Fig. 6.2, we have included all three species with high degrees of rate control (C^* , CO^* , and $C-O^*$), and not just the highest two as in Fig. 6.2. To show the differences between different groups of metals, we use the distance between Rh and other metal on the E_C , E_O plane of Fig. 6.1. The smaller this distance, the more likely that Eq. (6.6) will be accurate, since the changes in degrees of rate control will be smaller. The fairest way to compare with the results from the Nørskov-Bligaard method (which we will call “NB Direct LS”) is to use the same exact energies for the different metals in both methods. In practice, this requires estimating the energies for the key species with the highest DRCs using the same linear scaling (LS) relationships as employed in the NB Direct LS method. (For both methods, the direct DFT energies were used for the reference metal Rh, since these were needed for Rh to calculate the DRCs.) Figure 6.3 compares the results of the DRC method calculated in this way (i.e., using energies calculated from LS relationships, or the “DRC LS” method) and the results from the NB Direct LS method. Excellent quantitative agreement can be seen for those metals whose distance from Rh is small (< 0.5 eV) including Ni, Ir, Co and Ru. At the greater distance from Rh of ~ 1.3 eV, where Fe, Pt and Pd lie, qualitative agreement is still obtained, but there is less quantitative accuracy. When

the distance from Rh is >2.0 eV, as for Cu, Ag, and Au, there is a complete breakdown of both quantitative and qualitative agreement between the DRC LS method and the NB Direct LS method.

Further analysis is shown in Fig. 6.3, where we also calculate the rates again using the DRC method, only now using the energies for the key species (i.e., its descriptors) as calculated directly by DFT rather than as estimated from linear scaling relations. We refer to this method as the “DRC DFT” method. In the cases of Ir and Co, there is large disagreement between the rates predicted by this DRC DFT method and those by the DRC LS method, which agreed so well with the NB Direct LS method. This error is the result of substantial errors in the linear scaling relationships for the cases of Ir and Co. That is, at least one descriptor’s energy for each of these two metals deviates substantially from the best-fit straight line used to estimate its energy in this way. In the case of Ir, for example, it was found that the linear scaling relationships are quite inaccurate for Ir in the case of E_{CO^*} , where the formation energy of CO^* for Ir calculated from that linear scaling relationship is much higher than that calculated directly by DFT, as used in our analysis with Eq. (6.6) (1.16 eV from linear scaling versus 0.64 eV from DFT). Because the direct DFT energies are in principle more accurate for any given metal than the energies obtained from linear scaling approximations, these DRC DFT points are in principle more accurate than those from the DRC LS method (and therefore also more accurate than the NB Direct method). This highlights an advantage of this DRC method (when one is near the reference metal on the descriptor plot). Note that the rate improvement is quite large (a factor of $\sim 10^3$), and it qualitatively changes the conclusion as to Ir being more active than Rh: It should be less active!

Lastly, Fig. 6.3 also shows the results calculated from the DRC DFT method using only two descriptors (2D), which are the same points as those shown in Fig. 6.2. Comparing the DRC

DFT points with three descriptors (3D), it can be seen that reasonable fidelity can be obtained using just those two species with the largest DRCs.

The qualitative failures of this method with Cu, Ag, and Au, as well as the quantitative failure of this method with Fe, Pt, Pd, and Re point to its most major limitation, the limited locality for which it is useful, as highlighted in Fig. 6.3. While the linear scaling relationships used in the NB Direct LS method is able to cover a wider range of metals and can qualitatively agree with observations from experiment, our method only functions well in regions near the base case, or “reference” catalyst. That limitation aside, this technique shows an accuracy advantage over the linear scaling method as is shown particularly in the case of Ir and Co. There exists scatter in all of the linear scaling relationships used, and it is sometimes quite significant. By avoiding those linear approximations, the method of this paper allows for higher precision. Additionally, because the energies of only a small number of species need to be calculated, it is more feasible to use more expensive, higher accuracy, state-of-the-art computational methods to calculate those adsorbates energies on different potential catalyst surfaces, like alloys.

Further understanding of the deviations between these two methods can be seen by looking at the variations in the degrees of rate control for all species in this microkinetic model as a function of their position in E_{C^*} , E_{O^*} descriptor space. Figure 6.4 shows these plots for the six species with the largest degrees of rate control across all E_{C^*} , E_{O^*} space. The DRC method should only work well when all of the degrees of rate control are the same on the different materials being explored as on the reference metal Rh. On Rh, the species with highest DRCs were CO^* , $C-O^*$, and C^* . For the metals observed to agree well with the linear scaling methodology it can be seen that they possess similar degrees of rate control to Rh on those plots. For metals that agree less well (Fe, Re, Pt, Pd), the degree of rate control for one of these three

species is decreases in magnitude substantially, and another new species is beginning to have high degrees of rate control too. For example, Pt and Pd show a low DRC for C-O*, but now a high DRC for C-OH*.

There are a few cases in Figs. 6.3 and 6.4 where the linear scaling method and the DRC method agree even though the metals do not appear to possess the same DRCs. In Co for example, Fig. 6.4 shows a high DRC for C*, O*, and C-O*, but a low DRC for CO*, yet in Fig. 6.3 the two methods give similar rates. Such behavior is expected to occur in some cases due to compensation that arises from the general linear scaling of energies. In this case, for example, the C-O* energy scales linearly with the O* energy as well as with the C* energy, so they to some extent compensate. Additionally because the CO* energy scales linearly with the C* energy, some additional compensation is expected because in effect the C* energy is “being counted more than once”. Finally it is also worth pointing out that the DRCs calculated in Fig. 6.4 were calculated using the linear scaling relationships, and not the direct DFT energies. It is likely that for the metals where the linear scaling relations are less accurate (such as Ir, see above), the degrees of rate control calculated in this way could be in substantial error.

Note that the degrees of rate control for the reference material can be estimated experimentally as well. For example, when there is a rate-determining step, the degree of rate control for its transition state is 1.0. The degrees of rate control for adsorbed intermediates are proportional to their coverages⁵³, which can also be measured. For example when there is a single rate determining step, as frequently has been determined by experiments, the DRC for its transition state is 1. Thus, the new approach presented here also allows one to search for better catalyst materials without even developing a full microkinetic model for the reference material, or even knowing the complete mechanism. This is because Eq. (6.6) allows one to estimate the

rates for new materials using only the degrees of rate control and the energies of the most rate controlling species.

Computational Time Comparison

One potentially big advantage of this new approach is its computational efficiency when screening materials for catalytic activity. It is far simpler to implement (even though transition state energies are slow to calculate), since it does not require developing any of the many linear scaling relations needed for the approach of Nørskov and Bligaard. Furthermore, after the degree of rate control has been computed for the reference material, it is no longer necessary to use a kinetic model or solve complex differential equations for the other materials. One simply uses Eq. (6.6).

The time (t) required beyond the reference material for the NB Direct LS method can be estimated as:

$$t = (M * (N_I + \alpha N_T) + 2 * M_S)t_0 . \quad (6.7)$$

where t_0 is the approximate time for a single adsorption energy calculation (by DFT, for example), N_I is the number of adsorbed intermediates in the full mechanism, N_T is the number of transition-states, α is the average ratio of computational time needed for one transition state energy relative to that for one adsorbate, M is the number of additional material surfaces used to develop the LS relationships and M_S is the number of new material surfaces to be screened for rates.

The approximate time needed for catalyst screening using the DRC method can be estimated as:

$$t = (M_S * (N_{I,K} + \alpha N_{T,K}))t_0 . \quad (6.8)$$

where $N_{I,K}$ and $N_{T,K}$ represent the number of key adsorbed intermediates and key transition-states with large DRCs whose energies are used when applying Eq. (6.6) (typically 1 or 2 of each).

Figure 6.5 compares the computational time needed for these two approaches for typical values of the parameters in Eqs. (6.7)-(6.8). The new method of this paper (blue curve) leads to considerable speedup when only a moderate number of materials are screened (<100), but is actually slower for a large number of materials (>150) due to the additional computational cost of calculating these key transition-states for so many materials. One can also use LS relationships to estimate the energies of the key transition-states needed in this new method, but these relations are less accurate, as discussed above and shown to be a problem with the standard NB method. However, doing so leads to a much reduced computational time requirement for the new method of this paper, given by:

$$t = (M * (2 + \alpha) + M_S * (N'_A + 2N'_T))t_0 . \quad (6.9)$$

Figure 6.5 (red curve) demonstrates that when using LS for transition states only, our new DRC approach remains faster than the NB Direct LS approach out to much larger numbers of screened materials (~1000). The improvements in screening time and improved accuracy of the DRC method make it an excellent complement to the traditional approach of catalyst screening with microkinetic models. However, it is not as robust, since it only works for relatively similar materials (descriptor differences < 0.5 eV, as quantified in Fig. 6.3)

Comparison to Previous Theory and Experiments

Table 6.3 compares the predictions of these computational results regarding the relative activities of different metals to experiments from several groups.

Comparing to the results of Xu et al. in Table 6.3, it can be seen that the method of this paper matches their predictions of the relative catalyst activities of different metals almost exactly when using the same energies for our new descriptors obtained from linear scaling relations as those used for the calculations of Xu et al.. When using the numbers from DFT, this method more closely matches the theoretical results of Jones et al. with the exceptions of Co and Fe. Finally, comparing the results of the DFT DRC method to the experimental work of Jones et al.²³⁴, which used reaction conditions most similar to those modelled here (Table 6.1), we see similarly good agreement. Other experimental results are reported in Table 6.3, but these are at such different reaction conditions than modelled here that it is not clear that the relative activities should be the same as in the results of this paper. In their experiments, Jones et al. observed a change in TOF by a factor of about 10 between the highly active Rh and Ru catalysts and the less active Ni, Ir, Pd, and Pt catalysts.

Conclusions

A new method for catalyst screening is presented which is based on the concept of degree of rate control. The method is similar to the linear scaling relationships used previously to construct volcano plots, however by relying on the degree of rate control the number of adsorbate species which needs to be calculated can be reduced significantly. The method is used to reanalyze the data of Xu et al. who studied methane steam reforming using linear scaling relationships. The results of the new method agree very well with those of Xu et al. There are a few notable differences between the two methods, such as the artificially high activity predicted by Xu et al. for Ir, which highlights some of the advantages of not having to rely on linear scaling relations, and the artificially high rates for noble metals predicted by our method, showing the limited locality for which the DRC method is applicable. Another potential

advantage of the DRC method includes the narrowing of the number of adsorbates which need to be calculated with high accuracy by DFT. Because of how the DRC method is derived, however, it possesses the drawback of only being accurate in a region local to the selected “reference” catalyst. It was found that the accuracy of this method dropped as the distance between the “reference” catalyst and the test catalyst increased on a plane of the M-C and M-O formation energies. These changes in bonding character are indicative of a change in degree of rate control, causing this method to fail at extreme differences. Excellent quantitative agreement was observed between the DRC screening method and the linear scaling relationship method of Xu et al. out to a distance of ~ 0.5 eV on the (E_C, E_O) plane. Qualitative agreement is seen all the way out to ~ 1.3 eV, but the method was observed to breakdown completely when the distance is above ~ 2.0 eV. The DRC method presents a new, intuitive way of screening potential catalysts by focusing only on those adsorbates with the highest degree of rate control, and shows great potential as a tool to aid in new catalyst discovery.

Tables

Table 6.1. Reaction conditions used in microkinetic model for steam reforming of methane, from Xu et al.²³⁵. These are similar conditions to those used in the experiments conducted by Jones et al.²³⁴they. Note that these concentrations correspond to 29 % conversion starting from pure methane and water. The total pressure (P) is nearly constant throughout the reactor.

Condition	Lab Scale
T (K)	773
P (bar)	1
H ₂ O (mol%)	40
H ₂ (mol%)	15
CH ₄ (mol%)	40
CO (mol%)	5

Table 6.2. The degrees of rate control for all intermediates and transition states for Rh(211) at the conditions of Table 6.1, calculated using CatMAP software and the microkinetic model laid out in this paper.

Species	X_i	Species	X_i
Intermediates		Transition State	
CO*	-0.99	C-O*	0.98
C*	-0.66	H-OH*	0.01
CH*	-0.01	C-OH*	0.00
H*	0.00	CO-H*	0.00
O*	0.00	H-C*	0.00
OH*	0.00	H-CH*	0.00
CH3*	0.00	H-CH2*	0.00
CH2*	0.00	H-CO*	0.00
HCO*	0.00	H-CH3*	0.00
COH*	0.00	O-CH*	0.00
		H-H*	0.00
		O-H*	0.00

Table 6.3. Comparisons of the ranking of catalytic activities between different metals which are similar (defined as $\Delta E_M < 1.5$ eV, where ΔE_M is the distance from Rh on a plane of E_{C^*} , E_{O^*} , formation energies, see text of Fig. 6.3) to Rh for steam reforming of methane from experiments and theory.

Source	Reaction Cond.	Inlet Composition (mol fraction), and Conversion	Ranking
Theory			
Xu et al. ²³⁵	773 K, 1 bar	0.40 H ₂ O, 0.15 H ₂ , 0.40 CH ₄ , 0.05 CO, 29%	Co>Fe>Ir>Ru~Ni>Rh>Pt~Pd
This paper (NB Direct LS)	773K, 1 bar	0.40 H ₂ O, 0.15 H ₂ , 0.40 CH ₄ , 0.05 CO, 29%	Fe>Co>Ir>Ru>Ni>Rh>Pd>Pt
This paper (DRC LS)	773 K, 1 bar	0.40 H ₂ O, 0.15 H ₂ , 0.40 CH ₄ , 0.05 CO, 29%	Fe>Co>Ir>Ru~Ni>Rh>Pt>Pd
This paper (DRC DFT)	773K, 1 bar	0.40 H ₂ O, 0.15 H ₂ , 0.40 CH ₄ , 0.05 CO, 29%	Co>Fe>Ru>Ni>Rh>Ir>Pt>Pd
Jones et al. ²³⁴	773 K, 1 bar	0.74 H ₂ O, 0.07 H ₂ , 0.19 CH ₄ , 10%	Ru>Rh>Ni>Ir>Co>Pt~Pd>Fe
Experiments			
Jones et al. ²³⁴	773 K, 1 bar	0.74 H ₂ O, 0.07 H ₂ , 0.19 CH ₄ , <15%	Rh~Ru>Ni~Ir~Pt~Pd
Rostrup-Nielsen et al. ²³⁹	773 K, 1 bar	0.82 H ₂ O, 0.08 H ₂ , 0.10 CH ₄ , 5%	Rh~Ru>Ni~Pd~ Pt>Re>(Ni0.7Cu1.3)>Co
Kikuchi et al. ²⁴⁰	623 K to 773 K, 1 bar	0.75 H ₂ O, 0.25 CH ₄ , (27 to 48% depending on M)	Ru~Rh>Ni>Ir>Pd~Pd>>Co~Fe
Qin et al. ²⁴¹	873 K to 1173 K, 1 bar	0.14 H ₂ O, 0.57 N ₂ , 0.21 CH ₄ , 0.14 CO ₂ , (0 to 67%, depending on M, T)	Rh~Ru>Ir>Pt>Pd (T>980K) Rh~Ru>Ir~Pt~Pd (T<980K)
Wei et al. ²⁴²	873K, 1 bar	0.25 H ₂ O, 0.20 CH ₄ , 0.55 Ar (% conv. not reported)	Pt>Ir>Rh>Ru~Ni

Figures

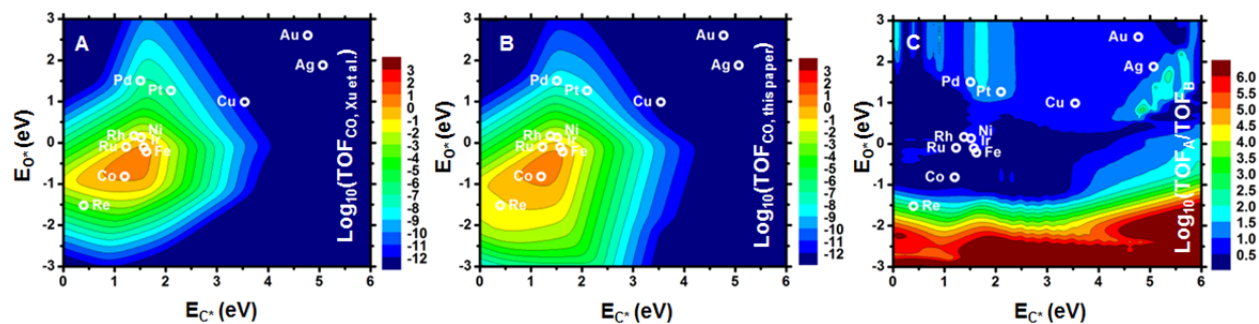


Figure 6.1. Volcano plot of catalyst activity (log TOF) for steam reforming of methane on the (211) face of different metals at the conditions of Table 6.1, plotted as a function of the two descriptors used in the most common method for computational catalyst screening: the formation energies of adsorbed O and C atoms. The energies for all other species needed in the microkinetic model were calculated from these descriptors using linear scaling relations. Three plots are shown, A) is the original volcano plot calculated by Xu et al. B) is the volcano plot produced in this paper in an attempt to reproduce that of Xu et al. and the differences between the two are discussed in the text. C) shows the log of the ratio of the TOFs between these two plots, and it can be seen that excellent agreement is seen near the top of the volcano (less than 1 order of magnitude difference) and good agreement (2 or less orders of magnitude difference) is seen for all cases where E_{O^*} is greater than -1 eV.

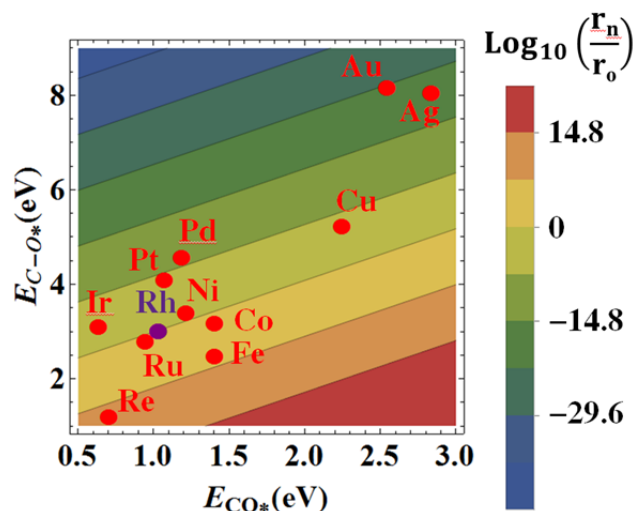


Figure 6.2. A plot of the relative rates of methane steam reforming for the (211) face of different metals, plotted versus the two new descriptors proposed in this paper: the energies of the two species in the reaction mechanism with the highest magnitude degrees of rate control. The rates were estimated using Eq. (6.6), assuming that only the two most rate-controlling species, the adsorbed CO intermediate of energy E_{CO^*} and the transition state of energy E_{C-O^*} , determine the rate. The color axis is the rate relative to the reference metal, (r_n/r_0) from Eq. (6.6) and plotted logarithmically. The red dots represent the calculated rates for various catalytic materials with their relative energies $E_{C-O^*,n}$ and $E_{CO^*,n}$ being the only two parameters which change relative to the purple dot, which represents the reference catalyst, Rh. The energies of the species on each metal are taken from Medford et al. and were all calculated directly by DFT on the (211) crystal surface. By definition, the purple dot (Rh), should have a relative rate equal to 1, all worse catalysts have relative rates below 1, and better catalysts above 1. Used as a screen for potential new catalysts, one sees here that materials with better rates than Rh require descriptor values in the range: $E_{CO^*,n} > E_{CO^*,Rh}$ and $E_{C-O^*,n} < E_{C-O^*,Rh}$. In these reaction conditions, there are actually three species with high degrees of rate control on Rh, so greater accuracy could be achieved by including this third species in Eq. (6.6), as done in Fig. 6.3 below.

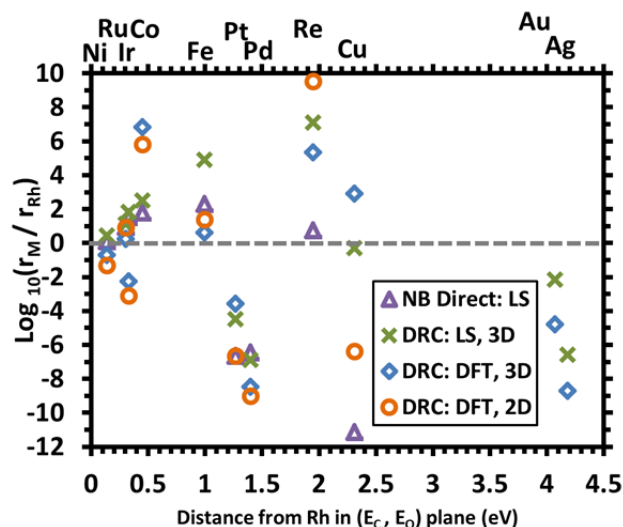


Figure 6.3. A comparison of the expected relative rate versus Rh(211) for different metals at the conditions of Table 6.1 as a function of distance from Rh on a plane of M-C (E_{C^*}), M-O (E_{O^*}) formation energies. Four sets of numbers are shown. The purple triangles are the rates calculated in this paper using the Nørskov-Bliggaard Direct method with linear scaling relationships, NB Direct LS. The rates from this NB Direct LS method are off scale for Ag, and Au at values of -18.8 and -19.0, respectively. The **X** points are calculated using the DRC method of this paper (ie., Eq. (6.6)) with three descriptors (3D), the energies of the three species with the largest DRCs: CO^* , C-O^* , and C^* , with the formation energies for each species in this case (DRC: LS, 3D) taken from the linear scaling relationships used to generate Fig. 6.1 (except for the Rh reference). These green **X**'s and the purple triangles show excellent agreement for metals similar to Rh. The blue diamonds are calculated also using the DRC method of this paper with the same three descriptors, s only now getting their energies directly from DFT calculations without invoking linear scaling approximations (DRC: DFT, 3D). Lastly, the orange circles are calculated using the DRC method of this paper with numbers from DFT, but now only using two descriptors (2D), the energies of the two species with the largest DRCs: CO^* and C-O^* (DRC: DFT, 2D). These points are identical to the points in Fig. 6.2. The X-axis positions for Pt and Pd are nearly identical and so their points have been nudged apart by 0.1eV here in order to more clearly differentiate those points. Points not shown are outside the range shown.

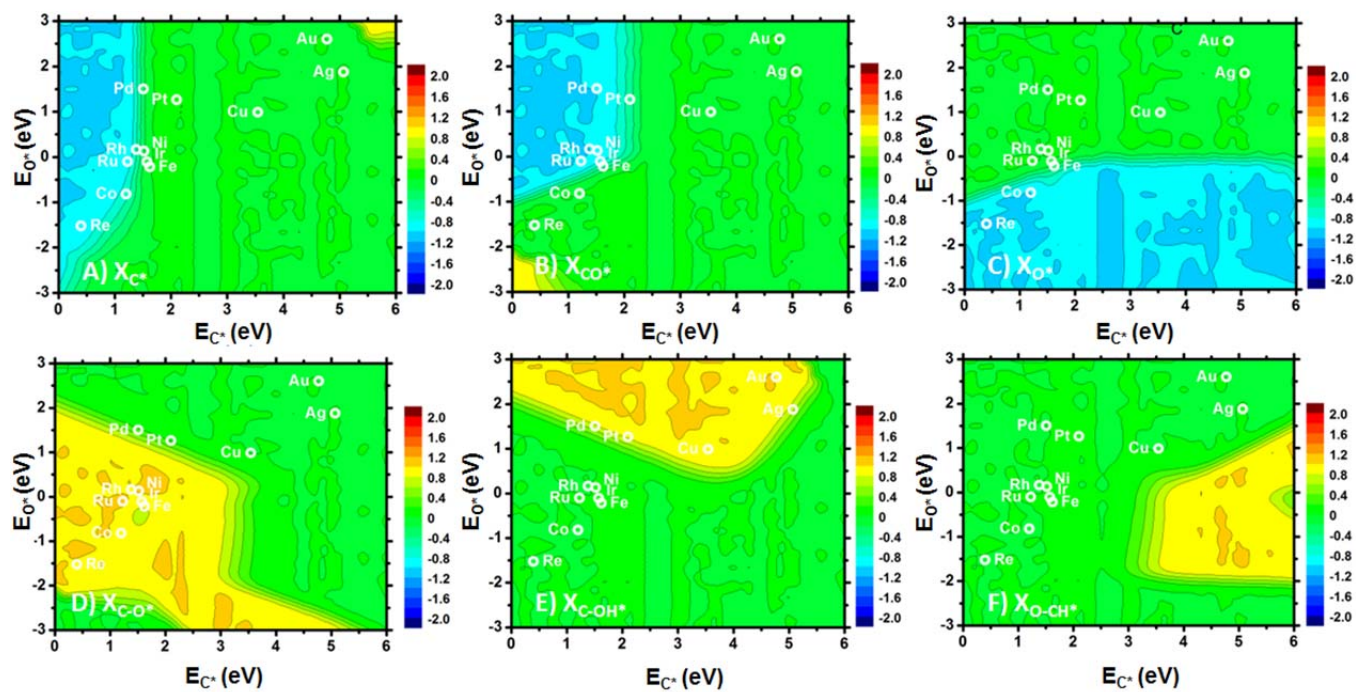


Figure 6.4. Degrees of rate control for different species as functions of E_{C^*} and E_{O^*} descriptors used in linear scaling relationships calculated by CATMAP. Species are A) C^* , B) CO^* , C) O^* , D) $C-O^*$, E) $C-OH^*$, and F) $O-CH^*$. The variability in these degrees of rate control corresponds to the observation in Fig. 6.3 that the further one moves from Rh in descriptor space, the more inaccurate the “constant DRC method” of predicting rates (i.e., Eq. (6.6)) becomes.

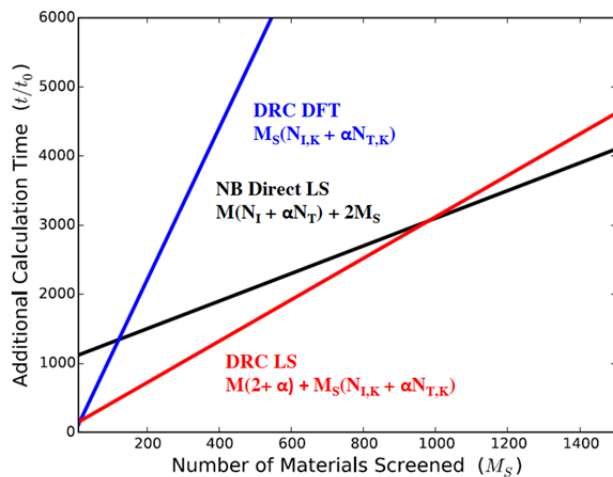


Figure 6.5. Comparison of estimated computer time needed for catalyst screening as a function of the number of surfaces to be screened. The black line shows the time for the traditional Nørskov-Bligaard approach. The blue line shows the integrated DRC method with transition-states computed using DFT, while the red line assumes that transition-states are estimated from linear scaling relationships. For this plot, reasonable values of $N_I = N_T = M = \alpha = 10$ and $N_{I,K} = N_{T,K} = 1$ were used. These numbers will differ from system to system, and in particular α will vary considerably based on the transition-state and the search algorithm used. However, the qualitative behavior shown here will remain.

Conclusion

Catalysts are used in more than 90% of commercial chemical processes, the majority of which are heterogeneous catalysts¹⁻⁴. Products of heterogeneous catalysis like fertilizers, fuels, and plastics are the basis of our entire modern society. Because of the incredible scale which these processes occur, even very small improvements in catalyst performance can result in millions of dollars in increased revenue. That motivation alone is enough to look for catalyst improvements, but catalysis also plays a role in many developing technologies including green chemistry, fuel cells, dye sensitized solar cells, and more. Despite all of this motivation and decades of research there remains a great deal of fundamental understanding to be gained in understanding precisely what is occurring on catalyst surfaces.

Solid understanding of reaction pathway and kinetics is missing for most catalytic systems. Without this basic knowledge making improvements in catalysis is a slow and expensive process²³⁻²⁵. Surface science has long been applied to catalytic systems in an attempt to gain a better fundamental understanding of these processes²⁶. This work has been fruitful for example, resulting in a step by step understanding of the Haber-Bosch process for ammonia synthesis on an iron catalyst, work which was awarded a Nobel Prize in 2007. As much of an accomplishment as this was, work remains to be done in many other systems.

While the number of surface science techniques used to study adsorbate-surface systems in catalysis is quite extensive^{2, 26, 243}, until relatively recently the ability to measure heats of adsorption directly proved elusive. Indirect measurement methods like temperature programmed desorption or Langmuir adsorption experiments were used to calculate adsorbate energies. These methods were often imprecise, requiring the development of kinetic models to extract

meaningful information. These methods worked best for reversibly adsorbed species like CO. If a molecule decomposed on the surface, like methanol on oxygen covered Pt(111)⁴⁷, its energetics were much more difficult to study. Because the majority of catalytically interesting surface species are created by dissociation processes like dehydrogenation or dehydration this left an understanding of surface species energetics either missing or on shaky ground. The absence of this information was and remains today especially important for the burgeoning field of computational chemistry, particularly density functional theory. When applied to catalytic systems DFT can calculate the energetics and kinetics of different adsorbates on surfaces²⁷, but had very few solid experimental numbers to compare their calculations to, leaving the accuracy and value of these calculations in doubt.

Single crystal adsorption calorimetry is a technique developed by Sir David King in the early 1990's to address this lack of understanding of surface energetics⁸⁷. Using a thin film surface sample, a molecular beam, and an optical pyrometer his group was able to measure minute temperature changes on in a crystal surface during gas adsorption. This work was the first direct measurements of the heat adsorption of a molecule. This design was improved upon over the years, with a major improvement in signal to noise being made by our group with the development of a polymer (β -polyvinylidene difluoride) pyroelectric heat detector⁴¹. This improvement was especially important by allowing adsorption energy measurements to be carried out at cryogenic temperatures⁸¹. This improved detector was coupled with the construction of a SCAC apparatus with a molecular beam designed to dose low vapor pressure molecules which dissociate upon adsorption, the door was now open to probe the energetics of a vast array of molecular fragments on surfaces directly⁴². From its development in 2004, this instrument has measured the heats of adsorption for benzene⁶¹, naphthalene⁸⁹, cyclohexene⁹⁰,

water⁴³, hydroxyl⁹², methanol⁴⁷, methoxy⁴⁷, methyl iodide⁴⁴, methyl⁴⁸, diiodomethane⁹⁴, methylene⁹⁴, methylidyne⁹⁴, formic acid⁴⁵, monodentate formate⁴⁵, bidentate formate⁴⁵, t-butyl iodide⁹³ and t-butyl⁹³ on a Pt(111) surface, populating a library⁸⁰ of adsorption energetics for a vast number of catalytic intermediates on Pt(111) for important reactions such as the water gas shift reaction, steam reforming, hydrocarbon reforming, and more.

In this thesis I have presented work which (1) expand the capabilities of SCAC with a new, universal data analysis technique which truly eliminates all requirements for a kinetic model even in the event of slow reaction kinetics, (2) applied this technique to expand the library of known adsorbate energies by measuring the adsorption of CH₂I₂ on Pt(111) to measure the heats of formation for CH_{2,ad} and CH_{ad}, (3) showed preliminary work to measure the heats of adsorption of D₂O on Fe₃O₄(111) and NiO(111) which are among the first ever measurements made using SCAC on a well-defined metal oxide surface, and 4) developed a new methodology for computational catalyst screening using the concept of degree of rate control.

The common theme throughout this work has been a desire to improve the understanding of adsorption energetics on surfaces. Under this theme there are two main thrusts, development of benchmarks for comparison with computational methods, and showing how one would use “chemically accurate” numbers obtained from computation to screen potential catalysts. Work continues under each of these directions. Experimental work to broaden the variety of surfaces studied to include more complexity, such as is present in metal oxides has a great deal of potential as a place where great improvements can be made to improve both fundamental understanding and to observe how computational tools can handle increased complexity. Once one was confident that one had “chemically accurate” computational numbers, how one best uses those numbers to explore catalyst activity remains an area where much work is likely to be done.

The new methodology we have developed which uses the degree of rate control is an important step in this process, as it allows for faithful reproduction of the volcano curves with only a very small number of adsorbed energies needing to be calculated. Additionally by not relying on the linear scaling relationships widely used today, the degree of rate control method allows for quicker calculation of rates which are expected to be more accurate because they rely on the numbers calculated directly by DFT for each individual catalyst studied rather than linear relationships which can possess a great deal of scatter. The new method works best when materials with similar properties to the reference catalyst are used while the Nørskov method is more robust when extended to materials that are dissimilar. It is likely going forward further refinement of both the degree of rate control methodology and the linear scaling relationship methodology will occur in tandem as studies of the energetics of elementary steps in catalysis continue to become more and more important in the development of new catalytic materials.

References

1. Thomas, J. M.; Thomas, W. J., *Principles and practice of heterogeneous catalysis*. 1st ed.; Weinheim: New York, 2008.
2. Ertl, G., *Reactions at Solid Surfaces*. John Wiley & Sons, Inc.: Hoboken, NJ, 2009.
3. Boehm, H.-P.; Knoezinger, H.; in: Anderson, J. R.; Boudart, M., *Catalysis Science and Technology*. Springer: Berlin, 1983; Vol. 4.
4. Centi, G.; in: Cornils, B.; Herrmann, W. A.; Schloegl, R.; Wong, C.-H., *Catalysis from A to Z*. Wiley-VCH: Weinheim, 2000.
5. Mitchell, S.; Michels, N. L.; Perez-Ramirez, J., From powder to technical body: the undervalued science of catalyst scale up. *Chemical Society Reviews* 2013, 42, 6094-6112.
6. Wasmus, S.; Kuver, A., Methanol oxidation and direct methanol fuel cells: a selective review. *Journal of Electroanalytical Chemistry* 1999, 461, 14-31.
7. Liu, H. S.; Song, C. J.; Zhang, L.; Zhang, J. J.; Wang, H. J.; Wilkinson, D. P., A review of anode catalysis in the direct methanol fuel cell. *Journal of Power Sources* 2006, 155, 95-110.
8. Song, C. S., Fuel processing for low-temperature and high-temperature fuel cells - Challenges, and opportunities for sustainable development in the 21st century. *Catalysis Today* 2002, 77, 17-49.
9. Markovic, N. M.; Schmidt, T. J.; Stamenkovic, V.; Ross, P. N., Oxygen Reduction Reaction on Pt and Pt Bimetallic Surfaces: A Selective Review. *Fuel Cells* 2001, 1, 105-116.
10. Lee, K.; Zhang, J. J.; Wang, H. J.; Wilkinson, D. P., Progress in the synthesis of carbon nanotube- and nanofiber-supported Pt electrocatalysts for PEM fuel cell catalysis. *Journal of Applied Electrochemistry* 2006, 36, 507-522.
11. Koper, M. T. M., *Fuel Cell Catalysis: A Surface Science Approach*. Wiley: Hoboken, N.J., 2009.
12. Anastas, P. T.; Kirchhoff, M. M., Origins, current status, and future challenges of green chemistry. *Accounts of Chemical Research* 2002, 35, 686-694.
13. Hughes, M. D.; Xu, Y. J.; Jenkins, P.; McMorn, P.; Landon, P.; Enache, D. I.; Carley, A. F.; Attard, G. A.; Hutchings, G. J.; King, F.; Stitt, E. H.; Johnston, P.; Griffin, K.; Kiely, C. J., Tunable gold catalysts for selective hydrocarbon oxidation under mild conditions. *Nature* 2005, 437, 1132-1135.
14. Clark, J. H., Green Chemistry: challenges and opportunities. *Green Chemistry* 1999, 1, 1-8.
15. Mason, B. P.; Price, K. E.; Steinbacher, J. L.; Bogdan, A. R.; McQuade, D. T., Greener approaches to organic synthesis using microreactor technology. *Chemical Reviews* 2007, 107, 2300-2318.
16. Huber, G. W.; Corma, A., Synergies between bio- and oil refineries for the production of fuels from biomass. *Angewandte Chemie-International Edition* 2007, 46, 7184-7201.
17. Song, C. S., Global challenges and strategies for control, conversion and utilization of CO₂ for sustainable development involving energy, catalysis, adsorption and chemical processing. *Catalysis Today* 2006, 115, 2-32.
18. Armor, J. N., The multiple roles for catalysis in the production of H₂. *Applied Catalysis a-General* 1999, 176, 159-176.
19. Besenbacher, F.; Chorkendorff, I.; Clausen, B. S.; Hammer, B.; Molenbroek, A. M.; Norskov, J. K.; Stensgaard, I., Design of a surface alloy catalyst for steam reforming. *Science* 1998, 279, 1913-1915.

20. Bulushev, D. A.; Ross, J. R. H., Catalysis for conversion of biomass to fuels via pyrolysis and gasification: A review. *Catalysis Today* 2011, 171, 1-13.
21. Yerga, R. M. N.; Alvarez-Galvan, M. C.; Mota, N.; de la Mano, J. A. V.; Al-Zahrani, S. M.; Fierro, J. L. G., Catalysts for Hydrogen Production from Heavy Hydrocarbons. *Chemcatchem* 2011, 3, 440-457.
22. Trincado, M.; Banerjee, D.; Grutzmacher, H., Molecular catalysts for hydrogen production from alcohols. *Energy & Environmental Science* 2014, 7, 2464-2503.
23. Richardson, J. T., *Principles of Catalyst Development*. Plenum Press: New York, USA, 1989.
24. Baerns, M.; Holena, M., *Combinatorial Development of Solid Catalytic Materials*. Imperial College Press: London, England, 2009; Vol. 7.
25. *Design of Heterogenous Catalysts*. Wiley: Weinheim, Germany, 2009.
26. Ertl, G., Heterogeneous catalysis on the atomic scale. *The Chemical Record* 2001, 1, 33-45.
27. Hammer, B.; Hansen, L. B.; Norskov, J. K., Improved adsorption energetics within density-functional theory using revised Perdew-Burke-Ernzerhof functionals. *Physical Review B* 1999, 59, 7413-7421.
28. Norskov, J. K.; Bligaard, T.; Logadottir, A.; Bahn, S.; Hansen, L. B.; Bollinger, M.; Bengaard, H.; Hammer, B.; Sljivancanin, Z.; Mavrikakis, M.; Xu, Y.; Dahl, S.; Jacobsen, C. J. H., Universality in heterogeneous catalysis. *Journal of Catalysis* 2002, 209, 275-278.
29. Norskov, J. K.; Bligaard, T.; Rossmeyl, J.; Christensen, C. H., Towards the computational design of solid catalysts. *Nature Chemistry* 2009, 1, 37-46.
30. Norskov, J. K.; Bligaard, T., The Catalyst Genome. *Angewandte Chemie-International Edition* 2013, 52, 776-777.
31. Norskov, J. K.; Abild-Pedersen, F.; Studt, F.; Bligaard, T., Density functional theory in surface chemistry and catalysis. *Proceedings of the National Academy of Sciences of the United States of America* 2011, 108, 937-943.
32. Greeley, J.; Mavrikakis, M., Alloy catalysts designed from first principles. *Nature Materials* 2004, 3, 810-815.
33. Ford, D. C.; Xu, Y.; Mavrikakis, M., Atomic and molecular adsorption on Pt(111). *Surface Science* 2005, 587, 159-174.
34. Andersson, M. P.; Bligaard, T.; Kustov, A.; Larsen, K. E.; Greeley, J.; Johannessen, T.; Christensen, C. H.; Norskov, J. K., Toward computational screening in heterogeneous catalysis: Pareto-optimal methanation catalysts. *Journal of Catalysis* 2006, 239, 501-506.
35. Ertl, G., Surface Science. *Chemphyschem* 2009, 10, 22-22.
36. Campbell, C. T.; Sellers, J. R. V., Enthalpies and Entropies of Adsorption on Well-Defined Oxide Surfaces: Experimental Measurements. *Chemical Reviews* 2013, 113, 4106-4135.
37. King, D. A., Thermal Desorption from Metal-Surfaces. *Surface Science* 1975, 47, 384-402.
38. Hodgson, A., State resolved desorption measurements as a probe of surface reactions. *Progress in Surface Science* 2000, 63, 1-61.
39. Kung, H. H., *Transition Metal-oxides: Surface Chemistry and Catalysis*. Elsevier: New York, 1991; Vol. 45.
40. Borroni-Bird, C. E.; King, D. A., An Ultrahigh-Vacuum Single-Crystal Adsorption Microcalorimeter. *Review of Scientific Instruments* 1991, 62, 2177-2185.

41. Stuckless, J. T.; Frei, N. A.; Campbell, C. T., A novel single-crystal adsorption calorimeter and additions for determining metal adsorption and adhesion energies. *Review of Scientific Instruments* 1998, 69, 2427-2438.
42. Ajo, H. M.; Ihm, H.; Moilanen, D. E.; Campbell, C. T., Calorimeter for adsorption energies of larger molecules on single crystal surfaces. *Review of Scientific Instruments* 2004, 75, 4471-4480.
43. Lew, W. D.; Crowe, M. C.; Karp, E.; Campbell, C. T., Energy of Molecularly Adsorbed Water on Clean Pt(111) and Pt(111) with Coadsorbed Oxygen by Calorimetry. *Journal of Physical Chemistry C* 2011, 115, 9164-9170.
44. Karp, E. M.; Silbaugh, T. L.; Campbell, C. T., Energetics of Adsorbed CH₃ and CH on Pt(111) by Calorimetry: Dissociative Adsorption of CH₃I. *Journal of Physical Chemistry C* 2013, 117, 6325-6336.
45. Silbaugh, T. L.; Karp, E. M.; Campbell, C. T., Energetics of Formic Acid Conversion to Adsorbed Formates on Pt(111) by Transient Calorimetry. *Journal of the American Chemical Society* 2014, 136, 3964-3971.
46. Silbaugh, T. L.; Karp, E. M.; Campbell, C. T., Surface kinetics and energetics from single crystal adsorption calorimetry lineshape analysis: Methyl from methyl iodide on Pt(111). *Journal of Catalysis* 2013, 308, 114-121.
47. Karp, E. M.; Silbaugh, T. L.; Crowe, M. C.; Campbell, C. T., Energetics of Adsorbed Methanol and Methoxy on Pt(111) by Microcalorimetry. *Journal of the American Chemical Society* 2012, 134, 20388-20395.
48. Karp, E. M.; Silbaugh, T. L.; Campbell, C. T., Energetics of Adsorbed CH₃ on Pt(111) by Calorimetry. *Journal of the American Chemical Society* 2013, 135, 5208-5211.
49. Lytken, O.; Lew, W.; Campbell, C. T., Catalytic reaction energetics by single crystal adsorption calorimetry: hydrocarbons on Pt(111). *Chemical Society Reviews* 2008, 37, 2172-2179.
50. Abild-Pedersen, F.; Greeley, J.; Studt, F.; Rossmeisl, J.; Munter, T. R.; Moses, P. G.; Skulason, E.; Bligaard, T.; Norskov, J. K., Scaling properties of adsorption energies for hydrogen-containing molecules on transition-metal surfaces. *Physical Review Letters* 2007, 99, 4.
51. Grabow, L. C.; Studt, F.; Abild-Pedersen, F.; Petzold, V.; Kleis, J.; Bligaard, T.; Norskov, J. K., Descriptor-Based Analysis Applied to HCN Synthesis from NH₃ and CH₄. *Angewandte Chemie-International Edition* 2011, 50, 4601-4605.
52. Sehested, J.; Larsen, K. E.; Kustov, A. L.; Frey, A. M.; Johannessen, T.; Bligaard, T.; Andersson, M. P.; Norskov, J. K.; Christensen, C. H., Discovery of technical methanation catalysts based on computational screening. *Topics in Catalysis* 2007, 45, 9-13.
53. Stegelmann, C.; Andreasen, A.; Campbell, C. T., Degree of Rate Control: How Much the Energies of Intermediates and Transition States Control Rates. *Journal of the American Chemical Society* 2009, 131, 8077-8082.
54. Norskov, J. K.; Bligaard, T.; Kleis, J., Rate Control and Reaction Engineering. *Science* 2009, 324, 1655-1656.
55. Yang, M. L.; Zhu, Y. A.; Fan, C.; Sui, Z. J.; Chen, D.; Zhou, X. G., Density functional study of the chemisorption of C-1, C-2 and C-3 intermediates in propane dissociation on Pt(111). *Journal of Molecular Catalysis a-Chemical* 2010, 321, 42-49.
56. Silbaugh, T. L.; Jorge, J.; Zaera, F.; Campbell, C. T., submitted.

57. Tait, S. L.; Dohnalek, Z.; Campbell, C. T.; Kay, B. D., n-alkanes on Pt(111) and on C(0001)/Pt(111): Chain length dependence of kinetic desorption parameters. *Journal of Chemical Physics* 2006, 125.
58. Vines, F.; Lykhach, Y.; Staudt, T.; Lorenz, M. P. A.; Papp, C.; Steinruck, H. P.; Libuda, J.; Neyman, K. M.; Gorling, A., Methane Activation by Platinum: Critical Role of Edge and Corner Sites of Metal Nanoparticles. *Chemistry-a European Journal* 2010, 16, 6530-6539.
59. Zhang, R. G.; Song, L. Z.; Wang, Y. H., Insight into the adsorption and dissociation of CH₄ on Pt(h k l) surfaces: A theoretical study. *Applied Surface Science* 2012, 258, 7154-7160.
60. Nykanen, L.; Honkala, K., Density Functional Theory Study on Propane and Propene Adsorption on Pt(111) and PtSn Alloy Surfaces. *Journal of Physical Chemistry C* 2011, 115, 9578-9586.
61. Ihm, H.; Ajo, H. M.; Gottfried, J. M.; Bera, P.; Campbell, C. T., Calorimetric measurement of the heat of adsorption of benzene on Pt(111). *Journal of Physical Chemistry B* 2004, 108, 14627-14633.
62. Liu, W.; Carrasco, J.; Santra, B.; Michaelides, A.; Scheffler, M.; Tkatchenko, A., Benzene adsorbed on metals: Concerted effect of covalency and van der Waals bonding. *Physical Review B* 2012, 86.
63. Goda, A. M.; Neurock, M.; Barteau, M. A.; Chen, J. G., Effect of hydrocarbon chain length and cyclization on the adsorption strength of unsaturated hydrocarbons on Pt/3d bimetallic surfaces. *Surface Science* 2008, 602, 2513-2523.
64. Morin, C.; Simon, D.; Sautet, P., Trends in the chemisorption of aromatic molecules on a Pt(111) surface: Benzene, naphthalene, and anthracene from first principles calculations. *Journal of Physical Chemistry B* 2004, 108, 12084-12091.
65. Saeys, M.; Reyniers, M. F.; Marin, G. B.; Neurock, M., Density functional study of benzene adsorption on Pt(111). *Journal of Physical Chemistry B* 2002, 106, 7489-7498.
66. Karp, E. M.; Campbell, C. T.; Studt, F.; Abild-Pedersen, F.; Nerskov, J. K., Energetics of Oxygen Adatoms, Hydroxyl Species and Water Dissociation on Pt(111). *Journal of Physical Chemistry C* 2012, 116, 25772-25776.
67. Blonski, P.; Lopez, N., On the Adsorption of Formaldehyde and Methanol on a Water-Covered Pt(111): a DFT-D Study. *Journal of Physical Chemistry C* 2012, 116, 15484-15492.
68. Cahyanto, W. T.; Padama, A. A. B.; Escano, M. C. S.; Kasai, H., Preferential sites for adsorption of methanol and methoxy on Pt and Pt-alloy surfaces. *Physica Scripta* 2012, 85, 6.
69. Greeley, J.; Mavrikakis, M., A first-principles study of methanol decomposition on Pt(111). *Journal of the American Chemical Society* 2002, 124, 7193-7201.
70. Greeley, J.; Mavrikakis, M., Competitive paths for methanol decomposition on Pt(111). *Journal of the American Chemical Society* 2004, 126, 3910-3919.
71. Skoplyak, O.; Menning, C. A.; Barteau, M. A.; Chen, J. G. G., Reforming of Oxygenates for H₂ Production on 3d/Pt(111) Bimetallic Surfaces. *Topics in Catalysis* 2008, 51, 49-59.
72. Desai, S. K.; Neurock, M.; Kourtakis, K., A periodic density functional theory study of the dehydrogenation of methanol over Pt(111). *Journal of Physical Chemistry B* 2002, 106, 2559-2568.
73. Silbaugh, T. L.; Karp, E. M.; Campbell, C. T., Energetics of formic acid conversion to adsorbed formates on Pt(111) by transient calorimetry. *In preparation*.
74. Gao, W.; Keith, J. A.; Anton, J.; Jacob, T., Oxidation of formic acid on the Pt(111) surface in the gas phase. *Dalton Transactions* 2010, 39, 8450-8456.

75. Grabow, L. C.; Gokhale, A. A.; Evans, S. T.; Dumesic, J. A.; Mavrikakis, M., Mechanism of the water gas shift reaction on Pt: First principles, experiments, and microkinetic modeling. *Journal of Physical Chemistry C* 2008, 112, 4608-4617.
76. Michaelides, A.; Hu, P., Catalytic water formation on platinum: A first-principles study. *Journal of the American Chemical Society* 2001, 123, 4235-4242.
77. Fischer-Wolfarth, J. H.; Hartmann, J.; Farmer, J. A.; Flores-Camacho, J. M.; Campbell, C. T.; Schauermaun, S.; Freund, H. J., An improved single crystal adsorption calorimeter for determining gas adsorption and reaction energies on complex model catalysts. *Review of Scientific Instruments* 2011, 82, 15.
78. Schiesser, A.; Hertz, P.; Schafer, R., Thermodynamics and kinetics of CO and benzene adsorption on Pt(111) studied with pulsed molecular beams and microcalorimetry. *Surface Science* 2010, 604, 2098-2105.
79. Gajdos, M.; Eichler, A.; Hafner, J., CO adsorption on close-packed transition and noble metal surfaces: trends from ab initio calculations. *Journal of Physics-Condensed Matter* 2004, 16, 1141-1164.
80. Silbaugh, T. L.; Campbell, C. T., A review of catalytic intermediates studied by SCAC. in preparation.
81. Lew, W.; Lytken, O.; Farmer, J. A.; Crowe, M. C.; Campbell, C. T., Improved pyroelectric detectors for single crystal adsorption calorimetry from 100 to 350 K. *Review of Scientific Instruments* 2010, 81, 9.
82. King, D. A.; Wells, M. G., Molecular-beam investigation of adsorption kinetics on bulk metal targets - nitrogen on tungsten. *Surface Science* 1972, 29, 454-&.
83. Sellers, J. R. V.; James, T. E.; Hemmingson, S. L.; Farmer, J. A.; Campbell, C. T., Adsorption calorimetry during metal vapor deposition on single crystal surfaces: Increased flux, reduced optical radiation, and real-time flux and reflectivity measurements. *Review of Scientific Instruments* 2013, 84, 9.
84. Fischer-Wolfarth, J. H.; Hartmann, J.; Farmer, J. A.; Flores-Camacho, J. M.; Campbell, C. T.; Schauermaun, S.; Freund, H. J., An improved single crystal adsorption calorimeter for determining gas adsorption and reaction energies on complex model catalysts. *Review of Scientific Instruments* 2011, 82, 024102.
85. Etzel, K. D.; Bickel, K. R.; Schuster, R., A microcalorimeter for measuring heat effects of electrochemical reactions with submonolayer conversions. *Review of Scientific Instruments* 2010, 81, 8.
86. Rodriguez-Reyes, J. C. F.; Siler, C. G. F.; Liu, W.; Tkatchenko, A.; Friend, C. M.; Madix, R. J., van der Waals Interactions Determine Selectivity in Catalysis by Metallic Gold. *Journal of the American Chemical Society* 2014, 136, 13333-13340.
87. King, D. A., Adsorption Calorimeter on Single-Crystal Surfaces - a new Technique. *Physica Scripta* 1993, T49B, 560-562.
88. Brown, W. A.; Kose, R.; King, D. A., Femtomole adsorption calorimetry on single-crystal surfaces. *Chemical Reviews* 1998, 98, 797-831.
89. Gottfried, J. M.; Vestergaard, E. K.; Bera, P.; Campbell, C. T., Heat of adsorption of naphthalene on Pt(111) measured by adsorption calorimetry. *Journal of Physical Chemistry B* 2006, 110, 17539-17545.
90. Lytken, O.; Lew, W.; Harris, J. J. W.; Vestergaard, E. K.; Gottfried, J. M.; Campbell, C. T., Energetics of cyclohexene adsorption and reaction on Pt(111) by low-temperature microcalorimetry. *Journal of the American Chemical Society* 2008, 130, 10247-10257.

91. Lew, W.; Crowe, M. C.; Campbell, C. T.; Carrasco, J.; Michaelides, A., The Energy of Hydroxyl Coadsorbed with Water on Pt(111). *Journal of Physical Chemistry C* 2011, 115, 23008-23012.
92. Lew, W.; Crowe, M. C.; Karp, E.; Lytken, O.; Farmer, J. A.; Arnadottir, L.; Schoenbaum, C.; Campbell, C. T., The Energy of Adsorbed Hydroxyl on Pt(111) by Microcalorimetry. *Journal of Physical Chemistry C* 2011, 115, 11586-11594.
93. Silbaugh, T. L.; Giorgi, J. B.; Xu, Y.; Tillekaratne, A.; Zaera, F.; Campbell, C. T., Adsorption Energy of tert-Butyl on Pt(111) by Dissociation of tert-Butyl Iodide: Calorimetry and DFT. *Journal of Physical Chemistry C* 2014, 118, 427-438.
94. Wolcott, C. A.; Green, I. X.; Silbaugh, T. L.; Xu, Y.; Campbell, C. T., Energetics of Adsorbed CH₂ and CH on Pt(111) by Calorimetry: The Dissociative Adsorption of Diiodomethane. *The Journal of Physical Chemistry C* 2014, In Press.
95. Farmer, J. A.; Campbell, C. T.; Xu, L.; Henkelman, G., Defect Sites and Their Distributions on MgO(100) by Li and Ca Adsorption Calorimetry. *Journal of the American Chemical Society* 2009, 131, 3098-3103.
96. Farmer, J. A.; Ruzycski, N.; Zhu, J. F.; Campbell, C. T., Lithium adsorption on MgO(100) and its defects: Charge transfer, structure, and energetics. *Physical Review B* 2009, 80, 8.
97. Starr, D. E.; Campbell, C. T., Low-temperature adsorption microcalorimetry: Pb on MgO(100). *Journal of Physical Chemistry B* 2001, 105, 3776-3782.
98. Starr, D. E.; Bald, D. J.; Musgrove, J. E.; Ranney, J. T.; Campbell, C. T., Microcalorimetric measurements of the heat of absorption of Pb on well-defined oxides: MgO(100) and p(2x1)-oxide on Mo(100). *Journal of Chemical Physics* 2001, 114, 3752-3764.
99. Smedh, M.; Diaz, S. F.; Campbell, C. T., Adsorption and adhesion energies of Pb on (1x1)-Mo₂C/Mo(100) by calorimetry. *Physical Review B* 2003, 67, 8.
100. Farmer, J. A.; Baricuatro, J. H.; Campbell, C. T., Ag Adsorption on Reduced CeO₂(111) Thin Films. *Journal of Physical Chemistry C* 2010, 114, 17166-17172.
101. Sharp, J. C.; Yao, Y. X.; Campbell, C. T., Silver Nanoparticles on Fe₃O₄(111): Energetics by Ag Adsorption Calorimetry and Structure by Surface Spectroscopies. *Journal of Physical Chemistry C* 2013, 117, 24932-24936.
102. Starr, D. E.; Diaz, S. F.; Musgrove, J. E.; Ranney, J. T.; Bald, D. J.; Nelen, L.; Ihm, H.; Campbell, C. T., Heat of absorption of Cu and Pb on hydroxyl-covered MgO(100). *Surface Science* 2002, 515, 13-20.
103. Fischer-Wolfarth, J. H.; Farmer, J. A.; Flores-Camacho, J. M.; Genest, A.; Yudanov, I. V.; Rosch, N.; Campbell, C. T.; Schauermann, S.; Freund, H. J., Particle-size dependent heats of adsorption of CO on supported Pd nanoparticles as measured with a single-crystal microcalorimeter. *Physical Review B* 2010, 81, 241416.
104. Bebensee, F.; Zhu, J. F.; Baricuatro, J. H.; Farmer, J. A.; Bai, Y.; Steinruck, H. P.; Campbell, C. T.; Gottfried, J. M., Interface Formation between Calcium and Electron-Irradiated Poly(3-hexylthiophene). *Langmuir* 2010, 26, 9632-9639.
105. Diaz, S. F.; Zhu, J. F.; Harris, J. J. W.; Goetsch, P.; Merte, L. R.; Campbell, C. T., Heats of adsorption of Pb on pristine and electron-irradiated poly(methyl methacrylate) by microcalorimetry. *Surface Science* 2005, 598, 22-34.
106. Etzel, K. D.; Bickel, K. R.; Schuster, R., Heat Effects upon Electrochemical Copper Deposition on Polycrystalline Gold. *Chemphyschem* 2010, 11, 1416-1424.

107. Bickel, K. R.; Etzel, K. D.; Halka, V.; Schuster, R., Microcalorimetric determination of heat changes caused by overpotential upon electrochemical Ag bulk deposition. *Electrochimica Acta* 2013, 112, 801-812.
108. Stuckless, J. T.; Frei, N. A.; Campbell, C. T., Pyroelectric detector for single-crystal adsorption microcalorimetry: analysis of pulse shape and intensity. *Sensors and Actuators B-Chemical* 2000, 62, 13-22.
109. Deng, R. P.; Herceg, E.; Trenary, M., Characterization of methylidyne on Pt(111) with infrared spectroscopy. *Surface Science* 2004, 573, 310-319.
110. Fuhrmann, T.; Kinne, M.; Trankenschuh, B.; Papp, C.; Zhu, J. F.; Denecke, R.; Steinruck, H. P., Activated adsorption of methane on Pt(111) - an in situ XPS study. *New Journal of Physics* 2005, 7.
111. Papp, C.; Fuhrmann, T.; Trankenschuh, B.; Denecke, R.; Steinruck, H. P., Kinetic isotope effects and reaction intermediates in the decomposition of methyl on flat and stepped platinum (111) surfaces. *Chemical Physics Letters* 2007, 442, 176-181.
112. French, C.; Harrison, I., Orientation and decomposition kinetics of methyl iodide on Pt(111). *Surface Science* 1995, 342, 85-100.
113. Fairbrother, D. H.; Peng, X. D.; Viswanathan, R.; Stair, P. C.; Trenary, M.; Fan, J., Carbon carbon coupling of methyl groups on Pt(111). *Surface Science* 1993, 285, L455-L460.
114. Henderson, M. A.; Mitchell, G. E.; White, J. M., CH₃ and CH₃I chemistry on Pt(111) - The influence of CO. *Surface Science* 1991, 248, 279-286.
115. Marsh, A. L.; Becraft, K. A.; Somorjai, G. A., Methane dissociative adsorption on the Pt(111) surface over the 300-500 K temperature and 1-10 torr pressure ranges. *Journal of Physical Chemistry B* 2005, 109, 13619-13622.
116. Zaera, F., Mechanism for the catalytic exchange of methane with deuterium on Pt(111) surfaces. *Catalysis Letters* 1991, 11, 95-104.
117. Herceg, E.; Celio, H.; Trenary, M., Sensitivity improvement in surface infrared spectroscopy: Design, characteristics, and application of a high-temperature graphite source. *Review of Scientific Instruments* 2004, 75, 2545-2550.
118. Zaera, F.; Hoffmann, H., Detection of chemisorbed methyl and methylene groups - surface-chemistry of methyl-iodide on Pt(111). *Journal of Physical Chemistry* 1991, 95, 6297-6303.
119. Odelius, M.; Kadi, M.; Davidsson, J.; Tarnovsky, A. N., Photodissociation of diiodomethane in acetonitrile solution and fragment recombination into iso-diiodomethane studied with ab initio molecular dynamics simulations. *Journal of Chemical Physics* 2004, 121, 2208-2214.
120. Yaws, C. L., *Yaws' Handbook of Thermodynamic Properties for Hydrocarbons and Chemicals*. Knovel: 2009.
121. Kresse, G.; Furthmuller, J., Efficiency of ab-initio total energy calculations for metals and semiconductors using a plane-wave basis set. *Computational Materials Science* 1996, 6, 15-50.
122. Kresse, G.; Furthmuller, J., Efficient iterative schemes for ab initio total-energy calculations using a plane-wave basis set. *Physical Review B* 1996, 54, 11169-11186.
123. Kresse, G.; Joubert, D., From ultrasoft pseudopotentials to the projector augmented-wave method. *Physical Review B* 1999, 59, 1758-1775.
124. Perdew, J. P.; Burke, K.; Ernzerhof, M., Generalized gradient approximation made simple. *Physical Review Letters* 1996, 77, 3865-3868.

125. Klimes, J.; Bowler, D. R.; Michaelides, A., Chemical accuracy for the van der Waals density functional. *Journal of Physics-Condensed Matter* 2010, 22, 5.
126. Klimes, J.; Bowler, D. R.; Michaelides, A., Van der Waals density functionals applied to solids. *Physical Review B* 2011, 83, 13.
127. Blochl, P. E., Projector Augmented-Wave Method. *Physical Review B* 1994, 50, 17953-17979.
128. Methfessel, M.; Paxton, A. T., High-Precision Sampling for Brillouin-Zone Integration in Metals. *Physical Review B* 1989, 40, 3616-3621.
129. Neugebauer, J.; Scheffler, M., Adsorbate-Substrate and Adsorbate-Adsorbate Interactions of Na and K adlayers on Al(111). *Physical Review B* 1992, 46, 16067-16080.
130. Ashcroft, N. W.; Mermin, N. D., *Solid State Physics*. Holt, Rinehart, and Winston: New York, 1976.
131. Henkelman, G.; Uberuaga, B. P.; Jonsson, H., A climbing image nudged elastic band method for finding saddle points and minimum energy paths. *Journal of Chemical Physics* 2000, 113, 9901-9904.
132. Henkelman, G.; Jonsson, H., A dimer method for finding saddle points on high dimensional potential surfaces using only first derivatives. *Journal of Chemical Physics* 1999, 111, 7010-7022.
133. Frank, D. G.; Chyan, O. M. R.; Golden, T.; Hubbard, A. T., Probing 3 distinct iodine monolayer structures at Pt(111) by means of angular-distribution Auger microscopy - Results agree with scanning tunneling microscopy. *Journal of Physical Chemistry* 1993, 97, 3829-3837.
134. Labayen, M.; Furman, S. A.; Harrington, D. A., A thermal desorption study of iodine on Pt(111). *Surface Science* 2003, 525, 149-158.
135. Kua, J.; Faglioni, F.; Goddard, W. A., Thermochemistry for hydrocarbon intermediates chemisorbed on metal surfaces: CH_n-m(CH₃)(m) with n=1, 2, 3 and m ≤ n on Pt, Ir, Os, Pd, Ph, and Ru. *Journal of the American Chemical Society* 2000, 122, 2309-2321.
136. Kudchadker, S. A.; Kudchadker, A. P., Ideal Gas Thermodynamic Properties of the Eight Bromo- and Iodomethanes. *Journal of Physical and Chemical Reference Data* 1975, 4, 457-470.
137. Chickos, J. S.; Acree, W. E. J., Enthalpies of Vaporization of Organic and Organometallic Compounds, 1880--2002. *Journal of Physical and Chemical Reference Data* 2003, 32, 519-878.
138. Norton, P. R.; Davies, J. A.; Jackman, T. E., Absolute coverage and isosteric heat of adsorption of deuterium on Pt(111) studied by nuclear microanalysis. *Surface Science* 1982, 121, 103-110.
139. Guo, H. S.; Zaera, F., Thermal chemistry of diiodomethane on Ni(110) surfaces I. Clean and hydrogen-covered. *Surface Science* 2003, 547, 284-298.
140. Tkatchenko, A.; Batina, N.; Cedillo, A.; Galvan, M., Charge transfer and adsorption energies in the iodine-Pt(111) interaction. *Surface Science* 2005, 581, 58-65.
141. Michaelides, A.; Hu, P., Insight into microscopic reaction pathways in heterogeneous catalysis. *Journal of the American Chemical Society* 2000, 122, 9866-9867.
142. Zaera, F., Preparation and reactivity of alkyl-groups adsorbed on metal-surfaces. *Accounts of Chemical Research* 1992, 25, 260-265.
143. Chase, M. W., National Institute of Standards and T. NIST-JANAF thermochemical tables American Chemical Society; American Institute of Physics for the National Institute of Standards and Technology: Woodbury, NY, 1998.

144. Yeo, Y. Y.; Stuck, A.; Wartnaby, C. E.; King, D. A., Microcalorimetric study of ethylene adsorption on the Pt{111} surface. *Chemical Physics Letters* 1996, 259, 28-36.
145. Zhou, X. L.; White, J. M., Predosed oxygen temperature-programmed desorption as a kinetic probe of dehydrogenation on Pt(111). *Journal of Vacuum Science & Technology a-Vacuum Surfaces and Films* 1993, 11, 2210-2216.
146. Campbell, C. T.; Arnadottir, L.; Sellers, J. R. V., Kinetic Prefactors of Reactions on Solid Surfaces. *Zeitschrift Fur Physikalische Chemie-International Journal of Research in Physical Chemistry & Chemical Physics* 2013, 227, 1435-1454.
147. Jacob, T.; Goddard, W. A., Chemisorption of (CH_x and C₂H_y) hydrocarbons on Pt(111) clusters and surfaces from DFT studies. *Journal of Physical Chemistry B* 2005, 109, 297-311.
148. Psofogiannakis, G.; St-Amant, A.; Ternan, M., Methane oxidation mechanism on Pt(111): A cluster model DFT study. *Journal of Physical Chemistry B* 2006, 110, 24593-24605.
149. Kua, J.; Goddard, W. A., Oxidation of methanol on 2nd and 3rd row Group VIII transition metals (Pt, Ir, Os, Pd, Rh, and Ru): Application to direct methanol fuel cells. *Journal of the American Chemical Society* 1999, 121, 10928-10941.
150. Hasselov, M.; von der Kammer, F., Iron Oxides as Geochemical Nanovectors for Metal Transport in Soil-River Systems. *Elements* 2008, 4, 401-406.
151. Lu, A. H.; Salabas, E. L.; Schuth, F., Magnetic nanoparticles: Synthesis, protection, functionalization, and application. *Angewandte Chemie-International Edition* 2007, 46, 1222-1244.
152. Estrella, M.; Barrio, L.; Zhou, G.; Wang, X. Q.; Wang, Q.; Wen, W.; Hanson, J. C.; Frenkel, A. I.; Rodriguez, J. A., In Situ Characterization of CuFe₂O₄ and Cu/Fe₃O₄ Water-Gas Shift Catalysts. *Journal of Physical Chemistry C* 2009, 113, 14411-14417.
153. Kuhrs, C.; Arita, Y.; Weiss, W.; Ranke, W.; Schlogl, R., Understanding heterogeneous catalysis on an atomic scale: a combined surface science and reactivity investigation for the dehydrogenation of ethylbenzene over iron oxide catalysts. *Topics in Catalysis* 2001, 14, 111-123.
154. Farmer, J. A.; Campbell, C. T., Ceria Maintains Smaller Metal Catalyst Particles by Strong Metal-Support Bonding. *Science* 2010, 329, 933-936.
155. Bruix, A.; Rodriguez, J. A.; Ramirez, P. J.; Senanayake, S. D.; Evans, J.; Park, J. B.; Stacchiola, D.; Liu, P.; Hrbek, J.; Illas, F., A New Type of Strong Metal-Support Interaction and the Production of H₂ through the Transformation of Water on Pt/CeO₂(111) and Pt/CeO_x/TiO₂(110) Catalysts. *Journal of the American Chemical Society* 2012, 134, 8968-8974.
156. Ushakov, S. V.; Navrotsky, A., Direct measurements of water adsorption enthalpy on hafnia and zirconia. *Applied Physics Letters* 2005, 87, 3.
157. Hodge, N. A.; Kiely, C. J.; Whyman, R.; Siddiqui, M. R. H.; Hutchings, G. J.; Pankhurst, Q. A.; Wagner, F. E.; Rajaram, R. R.; Golunski, S. E., Microstructural comparison of calcined and uncalcined gold/iron-oxide catalysts for low-temperature CO oxidation. *Catalysis Today* 2002, 72, 133-144.
158. Edwards, J. K.; Solsona, B.; Landon, P.; Carley, A. F.; Herzing, A.; Watanabe, M.; Kiely, C. J.; Hutchings, G. J., Direct synthesis of hydrogen peroxide from H₂ and O₂ using Au-Pd/Fe₂O₃ catalysts. *Journal of Materials Chemistry* 2005, 15, 4595-4600.
159. Finch, R. M.; Hodge, N. A.; Hutchings, G. J.; Meagher, A.; Pankhurst, Q. A.; Siddiqui, M. R. H.; Wagner, F. E.; Whyman, R., Identification of active phases in Au-Fe catalysts for low-temperature CO oxidation. *Physical Chemistry Chemical Physics* 1999, 1, 485-489.

160. Golunski, S.; Rajaram, R.; Hodge, N.; Hutchings, G. J.; Kiely, C. J., Low-temperature redox activity in co-precipitated catalysts: a comparison between gold and platinum-group metals. *Catalysis Today* 2002, 72, 107-113.
161. Schubert, M. M.; Hackenberg, S.; van Veen, A. C.; Muhler, M.; Plzak, V.; Behm, R. J., CO oxidation over supported gold catalysts-"inert" and "active" support materials and their role for the oxygen supply during reaction. *Journal of Catalysis* 2001, 197, 113-122.
162. Avgouropoulos, G.; Ioannides, T.; Papadopoulou, C.; Batista, J.; Hocevar, S.; Matralis, H. K., A comparative study of Pt/gamma-Al(2)O(3), Au/alpha-Fe(2)O(3) and CuO-CeO(2) catalysts for the selective oxidation of carbon monoxide in excess hydrogen. *Catalysis Today* 2002, 75, 157-167.
163. Kung, H. H.; Kung, M. C.; Costello, C. K., Supported Au catalysts for low temperature CO oxidation. *Journal of Catalysis* 2003, 216, 425-432.
164. Rim, K. T.; Eom, D.; Liu, L.; Stolyarova, E.; Raitano, J. M.; Chan, S. W.; Flytzani-Stephanopoulos, M.; Flynn, G. W., Charging and Chemical Reactivity of Gold Nanoparticles and Adatoms on the (111) Surface of Single-Crystal Magnetite: A Scanning Tunneling Microscopy/Spectroscopy Study. *Journal of Physical Chemistry C* 2009, 113, 10198-10205.
165. Hutchings, G. J.; Hall, M. S.; Carley, A. F.; Landon, P.; Solsona, B. E.; Kiely, C. J.; Herzing, A.; Makkee, M.; Moulijn, J. A.; Overweg, A.; Fierro-Gonzalez, J. C.; Guzman, J.; Gates, B. C., Role of gold cations in the oxidation of carbon monoxide catalyzed by iron oxide-supported gold. *Journal of Catalysis* 2006, 242, 71-81.
166. Herzing, A. A.; Kiely, C. J.; Carley, A. F.; Landon, P.; Hutchings, G. J., Identification of active gold nanoclusters on iron oxide supports for CO oxidation. *Science* 2008, 321, 1331-1335.
167. Lee, E. H., Iron-Oxide Catalyst for Dehydrogenation of Ethylbenzene in the Presence of Steam. *Catalysis Reviews-Science and Engineering* 1973, 8, 285-305.
168. Hirano, T., Dehydrogenation of Ethylbenzene over Potassium-Promoted Iron-Oxide Containing Cerium and Molybdenum Oxides. *Applied Catalysis* 1986, 28, 119-132.
169. Rhodes, C.; Hutchings, G. J.; Ward, A. M., Water-Gas Shift Reaction - Finding the Mechanistic Boundary. *Catalysis Today* 1995, 23, 43-58.
170. Khader, M. M.; Vurens, G. H.; Kim, I. K.; Salmeron, M.; Somorjai, G. A., Photoassisted Catalytic Dissociation of H₂O to Produce Hydrogen on Partially Reduced Alpha-Fe₂O₃. *Journal of the American Chemical Society* 1987, 109, 3581-3585.
171. Weiss, W.; Ranke, W., Surface chemistry and catalysis on well-defined epitaxial iron-oxide layers. *Progress in Surface Science* 2002, 70, 1-151.
172. Weiss, W., Structure and composition of thin epitaxial iron oxide films grown onto Pt(111). *Surface Science* 1997, 377, 943-947.
173. Ritter, M.; Weiss, W., Fe₃O₄(111) surface structure determined by LEED crystallography. *Surface Science* 1999, 432, 81-94.
174. Lennie, A. R.; Condon, N. G.; Leibsle, F. M.; Murray, P. W.; Thornton, G.; Vaughan, D. J., Structures of Fe₃O₄ (111) surfaces observed by scanning tunneling microscopy. *Physical Review B* 1996, 53, 10244-10253.
175. Kim, Y. J.; Westphal, C.; Ynzunza, R. X.; Wang, Z.; Galloway, H. C.; Salmeron, M.; Van Hove, M. A.; Fadley, C. S., The growth of iron oxide films on Pt(111): a combined XPD, STM, and LEED study. *Surface Science* 1998, 416, 68-111.
176. Joseph, Y.; Kuhrs, C.; Ranke, W.; Weiss, W., Adsorption of water on Fe₃O₄(111) studied by photoelectron and thermal desorption spectroscopy. *Surface Science* 1999, 433, 114-118.

177. Lemire, C.; Meyer, R.; Henrich, V. E.; Shaikhutdinov, S.; Freund, H. J., The surface structure of Fe₃O₄(111) films as studied by CO adsorption. *Surface Science* 2004, 572, 103-114.
178. Leist, U.; Ranke, W.; Al-Shamery, K., Water adsorption and growth of ice on epitaxial Fe₃O₄(111), FeO(111) and Fe₂O₃(biphase). *Physical Chemistry Chemical Physics* 2003, 5, 2435-2441.
179. Rim, K. T.; Eom, D.; Chan, S. W.; Flytzani-Stephanopoulos, M.; Flynn, G. W.; Wen, X. D.; Batista, E. R., Scanning Tunneling Microscopy and Theoretical Study of Water Adsorption on Fe₃O₄: Implications for Catalysis. *Journal of the American Chemical Society* 2012, 134, 18979-18985.
180. Kendelewicz, T.; Liu, P.; Doyle, C. S.; Brown, G. E.; Nelson, E. J.; Chambers, S. A., Reaction of water with the (100) and (111) surfaces of Fe₃O₄. *Surface Science* 2000, 453, 32-46.
181. Petitto, S. C.; Tanwar, K. S.; Ghose, S. K.; Eng, P. J.; Trainor, T. P., Surface structure of magnetite (111) under hydrated conditions by crystal truncation rod diffraction. *Surface Science* 2010, 604, 1082-1093.
182. Rodriguez, J. A.; Hanson, J. C.; Frenkel, A. I.; Kim, J. Y.; Perez, M., Experimental and theoretical studies on the reaction of H₂ with NiO: Role of O vacancies and mechanism for oxide reduction. *Journal of the American Chemical Society* 2002, 124, 346-354.
183. Achenbach, E.; Riensche, E., Methane Steam Reforming Kinetics for Solid Oxide Fuel-Cells. *Journal of Power Sources* 1994, 52, 283-288.
184. deSouza, S.; Visco, S. J.; DeJonghe, L. C., Reduced-temperature solid oxide fuel cell based on YSZ thin-film electrolyte. *Journal of the Electrochemical Society* 1997, 144, L35-L37.
185. Rieder, K. H., Combined SIMS-AES-LEED Study of Room-Temperature Oxidation of Ni(110) and Ni(111) Surfaces. *Applications of Surface Science* 1978, 2, 74-84.
186. Okazawa, T.; Nishizawa, T.; Nishimura, T.; Kido, Y., Oxidation kinetics for Ni(111) and the structure of the oxide layers. *Physical Review B* 2007, 75, 4.
187. Wolf, D., Reconstruction of NaCl Surfaces from a Dipolar Solution to the Madelung Problem. *Physical Review Letters* 1992, 68, 3315-3318.
188. Barbier, A.; Mocuta, C.; Kuhlbeck, H.; Peters, K. F.; Richter, B.; Renaud, G., Atomic structure of the polar NiO(111)-p(2 x 2) surface. *Physical Review Letters* 2000, 84, 2897-2900.
189. Erdman, N.; Warschkow, O.; Ellis, D. E.; Marks, L. D., Solution of the p(2 x 2) NiO(111) surface structure using direct methods. *Surface Science* 2000, 470, 1-14.
190. Cappus, D.; Xu, C.; Ehrlich, D.; Dillmann, B.; Ventrice, C. A.; Alshamery, K.; Kuhlbeck, H.; Freund, H. J., Hydroxyl-Groups on Oxide Surfaces - NiO(100), NiO(111), and Cr₂O₃(111). *Chemical Physics* 1993, 177, 533-546.
191. Kitakatsu, N.; Maurice, V.; Hinnen, C.; Marcus, P., Surface hydroxylation and local structure of NiO thin films formed on Ni(111). *Surface Science* 1998, 407, 36-58.
192. Rohr, F.; Wirth, K.; Libuda, J.; Cappus, D.; Baumer, M.; Freund, H. J., Hydroxyl Driven Reconstruction of the Polar NiO(111) Surface. *Surface Science* 1994, 315, L977-L982.
193. Ciston, J.; Subramanian, A.; Kienzle, D. M.; Marks, L. D., Why the case for clean surfaces does not hold water: Structure and morphology of hydroxylated nickel oxide (111). *Surface Science* 2010, 604, 155-164.
194. Ventrice, C. A.; Bertrams, T.; Hannemann, H.; Brodde, A.; Neddermeyer, H., Stable Reconstruction of the Polar (111) Surface of NiO on Au(111). *Physical Review B* 1994, 49, 5773-5776.
195. Langell, M. A.; Nassir, M. H., Stabilization of NiO(111) Thin-Films by Surface Hydroxyls. *Journal of Physical Chemistry* 1995, 99, 4162-4169.

196. Ebensperger, C.; Meyer, B., First-principles study of the reconstruction and hydroxylation of the polar NiO(111) surface. *Physica Status Solidi B-Basic Solid State Physics* 2011, 248, 2229-2241.
197. Zscherpel, D.; Ranke, W.; Weiss, W.; Schlogl, R., Energetics and kinetics of ethylbenzene adsorption on epitaxial FeO(111) and Fe₃O₄(111) films studied by thermal desorption and photoelectron spectroscopy. *Journal of Chemical Physics* 1998, 108, 9506-9515.
198. Bandara, A.; Kubota, J.; Wada, A.; Domen, K.; Hirose, C., Adsorption and decomposition of formic acid on the NiO(111)-p(2x2) surface: TPD and steady state kinetics studies. *Surface Science* 1996, 364, L580-L586.
199. Bandara, A.; Kubota, J.; Onda, K.; Wada, A.; Kano, S. S.; Domen, K.; Hirose, C., Short-lived reactive intermediate in the decomposition of formate on NiO(111) surface observed by picosecond temperature jump. *Journal of Physical Chemistry B* 1998, 102, 5951-5954.
200. Matsumoto, T.; Kubota, J.; Kondo, J. N.; Hirose, C.; Domen, K., Adsorption structures of carbon dioxide on NiO(111) and hydroxylated NiO(111) studied by infrared reflection adsorption spectroscopy. *Langmuir* 1999, 15, 2158-2161.
201. Flores-Camacho, J. M.; Fischer-Wolfarth, J. H.; Peter, M.; Campbell, C. T.; Schauermann, S.; Freund, H. J., Adsorption energetics of CO on supported Pd nanoparticles as a function of particle size by single crystal microcalorimetry. *Physical Chemistry Chemical Physics* 2011, 13, 16800-16810.
202. Speedy, R. J.; Debenedetti, P. G.; Smith, R. S.; Huang, C.; Kay, B. D., The evaporation rate, free energy, and entropy of amorphous water at 150 K. *Journal of Chemical Physics* 1996, 105, 240-244.
203. Joseph, Y.; Kuhrs, C.; Ranke, W.; Ritter, M.; Weiss, W., Adsorption of water on FeO(111) and Fe₃O₄(111): identification of active sites for dissociation. *Chemical Physics Letters* 1999, 314, 195-202.
204. Joseph, Y.; Ranke, W.; Weiss, W., Water on FeO(111) and Fe₃O₄(111): Adsorption behavior on different surface terminations. *Journal of Physical Chemistry B* 2000, 104, 3224-3236.
205. Zhou, C. G.; Zhang, Q. F.; Chen, L.; Han, B.; Ni, G.; Wu, J. P.; Garg, D.; Cheng, H. S., Density Functional Theory Study of Water Dissociative Chemisorption on the Fe₃O₄(111) Surface. *Journal of Physical Chemistry C* 2010, 114, 21405-21410.
206. Grillo, M. E.; Finnis, M. W.; Ranke, W., Surface structure and water adsorption on Fe₃O₄(111): Spin-density functional theory and on-site Coulomb interactions. *Physical Review B* 2008, 77, 5.
207. Yu, X. H.; Li, Y. N.; Li, Y. W.; Wang, J. G.; Jiao, H. J., DFT plus U Study of Molecular and Dissociative Water Adsorptions on the Fe₃O₄(110) Surface. *Journal of Physical Chemistry C* 2013, 117, 7648-7655.
208. Tombacz, E.; Hajdu, A.; Illes, E.; Laszlo, K.; Garberoglio, G.; Jedlovsky, P., Water in Contact with Magnetite Nanoparticles, as Seen from Experiments and Computer Simulations. *Langmuir* 2009, 25, 13007-13014.
209. Cutting, R. S.; Murny, C. A.; Vaughan, D. J.; Thornton, G., Substrate-termination and H₂O-coverage dependent dissociation of H₂O on Fe₃O₄(111). *Surface Science* 2008, 602, 1155-1165.
210. Berdunov, N.; Murphy, S.; Mariotto, G.; Shvets, I. V., Room temperature study of a strain-induced electronic superstructure on a magnetite (111) surface. *Physical Review B* 2004, 70, 7.

211. Shaikhutdinov, S. K.; Joseph, Y.; Kuhrs, C.; Ranke, W.; Weiss, W., Structure and reactivity of iron oxide surfaces. *Faraday Discussions* 1999, 114, 363-380.
212. Weiss, W.; Barbieri, A.; Vanhove, M. A.; Somorjai, G. A., Surface-Structure Determination of an Oxide Film Grown on a Foreign Substrate - Fe₃O₄ Multilayer on Pt(111) Identified by Low-Energy-Electron Diffraction. *Physical Review Letters* 1993, 71, 1848-1851.
213. Christensen, T. M.; Raoul, C.; Blakely, J. M., Change in Oxide Epitaxy on Ni(111) - Effects of Oxidation Temperature. *Applied Surface Science* 1986, 26, 408-417.
214. Kitakatsu, N.; Maurice, V.; Marcus, P., Local decomposition of NiO ultra-thin films formed on Ni(111). *Surface Science* 1998, 411, 215-230.
215. Xu, C.; Goodman, D. W., Surface-Chemistry of Polar Oxide Surfaces - Formic-Acid on NiO(111). *Journal of the Chemical Society-Faraday Transactions* 1995, 91, 3709-3715.
216. Kubota, J.; Bandara, A.; Wada, A.; Domen, K.; Hirose, C., IRAS study of formic acid decomposition on NiO(111)/Ni(111) surface: Comparison of vacuum and catalytic conditions. *Surface Science* 1996, 368, 361-365.
217. Turner, H. W.; Volpe, A. F.; Weinberg, W. H., High-throughput heterogeneous catalyst research. *Surface Science* 2009, 603, 1763-1769.
218. Studt, F.; Abild-Pedersen, F.; Bligaard, T.; Sorensen, R. Z.; Christensen, C. H.; Norskov, J. K., Identification of non-precious metal alloy catalysts for selective hydrogenation of acetylene. *Science* 2008, 320, 1320-1322.
219. Greeley, J.; Stephens, I. E. L.; Bondarenko, A. S.; Johansson, T. P.; Hansen, H. A.; Jaramillo, T. F.; Rossmeisl, J.; Chorkendorff, I.; Norskov, J. K., Alloys of platinum and early transition metals as oxygen reduction electrocatalysts. *Nature Chemistry* 2009, 1, 552-556.
220. Bligaard, T.; Norskov, J. K.; Dahl, S.; Matthiesen, J.; Christensen, C. H.; Sehested, J., The Bronsted-Evans-Polanyi relation and the volcano curve in heterogeneous catalysis. *Journal of Catalysis* 2004, 224, 206-217.
221. Campbell, C. T., Finding the rate-determining step in a mechanism - Comparing DeDonder relations with the "degree of rate control". *Journal of Catalysis* 2001, 204, 520-524.
222. Sanchez-Castillo, M. A.; Agarwal, N.; Miller, C.; Cortright, R. D.; Madon, R. J.; Dumesic, J. A., Reaction kinetics study and analysis of reaction schemes for isobutane conversion over USY zeolite. *Journal of Catalysis* 2002, 205, 67-85.
223. Linic, S.; Barteau, M. A., Construction of a reaction coordinate and a microkinetic model for ethylene epoxidation on silver from DFT calculations and surface science experiments. *Journal of Catalysis* 2003, 214, 200-212.
224. Stegelmann, C.; Schiodt, N. C.; Campbell, C. T.; Stoltze, P., Microkinetic modeling of ethylene oxidation over silver. *Journal of Catalysis* 2004, 221, 630-649.
225. Kozuch, S.; Shaik, S., A combined kinetic-quantum mechanical model for assessment of catalytic cycles: Application to cross-coupling and Heck reactions. *Journal of the American Chemical Society* 2006, 128, 3355-3365.
226. Meskine, H.; Matera, S.; Scheffler, M.; Reuter, K.; Metiu, H., Examination of the concept of degree of rate control by first-principles kinetic Monte Carlo simulations. *Surface Science* 2009, 603, 1724-1730.
227. Campbell, C. T.; Sellers, J. R. V., The Entropies of Adsorbed Molecules. *Journal of the American Chemical Society* 2012, 134, 18109-18115.
228. Ferrin, P.; Nilekar, A. U.; Greeley, J.; Mavrikakis, M.; Rossmeisl, J., Reactivity descriptors for direct methanol fuel cell anode catalysts. *Surface Science* 2008, 602, 3424-3431.

229. Lausche, A. C.; Hummelshoj, J. S.; Abild-Pedersen, F.; Studt, F.; Norskov, J. K., Application of a new informatics tool in heterogeneous catalysis: Analysis of methanol dehydrogenation on transition metal catalysts for the production of anhydrous formaldehyde. *Journal of Catalysis* 2012, 291, 133-137.
230. Michaelides, A.; Liu, Z. P.; Zhang, C. J.; Alavi, A.; King, D. A.; Hu, P., Identification of general linear relationships between activation energies and enthalpy changes for dissociation reactions at surfaces. *Journal of the American Chemical Society* 2003, 125, 3704-3705.
231. Howarth, R. W.; Ingraffea, A.; Engelder, T., Natural gas: Should fracking stop? *Nature* 2011, 477, 271-275.
232. Holladay, J. D.; Hu, J.; King, D. L.; Wang, Y., An overview of hydrogen production technologies. *Catalysis Today* 2009, 139, 244-260.
233. Hickman, D. A.; Schmidt, L. D., Production of Syngas by Direct Catalytic-Oxidation of Methane. *Science* 1993, 259, 343-346.
234. Jones, G.; Jakobsen, J. G.; Shim, S. S.; Kleis, J.; Andersson, M. P.; Rossmeisl, J.; Abild-Pedersen, F.; Bligaard, T.; Helveg, S.; Hinnemann, B.; Rostrup-Nielsen, J. R.; Chorkendorff, I.; Sehested, J.; Norskov, J. K., First principles calculations and experimental insight into methane steam reforming over transition metal catalysts. *Journal of Catalysis* 2008, 259, 147-160.
235. Xu, Y.; Lausche, A. C.; Wang, S.; Khan, T. S.; Abild-Pedersen, F.; Studt, F.; Norskov, J. K.; Bligaard, T., In silico search for novel methane steam reforming catalysts. *New Journal of Physics* 2013, 15.
236. Medford, A. J.; Lausche, A. C.; Abild-Pedersen, F.; Temel, B.; Schjodt, N. C.; Norskov, J. K.; Studt, F., Activity and Selectivity Trends in Synthesis Gas Conversion to Higher Alcohols. *Topics in Catalysis* 2014, 57, 135-142.
237. Lausche, A. C.; Medford, A. J.; Khan, T. S.; Xu, Y.; Bligaard, T.; Abild-Pedersen, F.; Norskov, J. K.; Studt, F., On the effect of coverage-dependent adsorbate-adsorbate interactions for CO methanation on transition metal surfaces. *Journal of Catalysis* 2013, 307, 275-282.
238. Medford, A. J.; Sehested, J.; Rossmeisl, J.; Chorkendorff, I.; Studt, F.; Norskov, J. K.; Moses, P. G., Thermochemistry and micro-kinetic analysis of methanol synthesis on ZnO (0001). *Journal of Catalysis* 2014, 309, 397-407.
239. Rostrup-Nielsen, J. R., Activity of Nickel Catalysts for Steam Reforming of Hydrocarbons. *Journal of Catalysis* 1973, 31, 173-199.
240. Kikuchi, E.; Tanaka, S.; Yamazaki, Y.; Morita, Y., Steam Reforming of Hydrocarbons on Nobel Metal Catalysts (Part 1). *Bulletin of the Japan Petroleum Institute* 1974, 16, 95-98.
241. Qin, D.; Lapszewicz, J., Study of Mixed Steam and CO₂ Reforming of CH₄ to Syngas on MgO-Supported Metals. *Catalysis Today* 1994, 21, 551-560.
242. Wei, J. M.; Iglesia, E., Isotopic and kinetic assessment of the mechanism of reactions of CH₄ with CO₂ or H₂O to form synthesis gas and carbon on nickel catalysts. *Journal of Catalysis* 2004, 224, 370-383.
243. Ertl, G.; Kueppers, J., *Low Energy Electrons and Surface Chemistry*. VCH Verlagsgesellschaft mbH: Weinheim, Germany, 1985.

Curriculum Vitae

Christopher A. Wolcott
3624 Phinney Ave. N Apt 101
Seattle, WA 98103
(571) 246-2237
chrisw28@uw.edu

Education: University of Washington, Seattle, WA
Ph. D. in Chemical Engineering, expected graduation December 2014
Dissertation: “Energetics of Elementary Steps in Catalysis and Their Use to Search for New Catalysts”
Advisor: Charles T. Campbell

M.S. in Chemical Engineering, GPA 3.81/4.0, 2012

Illinois Institute of Technology, Chicago, IL
B. S. in Chemical Engineering, GPA 3.90/4.0 *Summa Cum Laude*, 2010

Publications:

1. C. A. Wolcott, I. X. Green, T. L. Silbaugh, Y. Xu, C. T. Campbell, Energetics of Adsorbed CH₂ and CH on Pt(111) by Calorimetry of Dissociative Adsorption of Diiodomethane, *J. Phys. Chem. C*, Article ASAP, DOI: 10.1021/jp505494a
2. C.A. Wolcott, C.T. Campbell, Method for direct deconvolution of heat signals in transient adsorption calorimetry, *Surf. Sci.* (2014), DOI: 10.1016/j.susc.2014.11.005
3. C.A. Wolcott, A.J. Medford, F. Studt, C.T. Campbell, Degree of Rate Control Approach to Computation Catalyst Screening, (in preparation)

Presentations:

1. C.A. Wolcott, I.X. Green, C.T. Campbell, “Adsorption and Reaction of D₂O on Fe₃O₄(111) Thin Films”, American Vacuum Society 2013 Meeting, Long Beach, CA
2. C.A. Wolcott, I.X. Green, T.L. Silbaugh, C.T. Campbell, “The Energetics of –CH₃, –CH₂, and –CH on Pt(111) Studied by Single Crystal Adsorption Calorimetry”, University of Washington Chemical Engineering Department 2013 Symposium, Seattle, WA
3. C.A. Wolcott, J. Guilfoyle, “Networking with Industry and Alumni”, American Institute of Chemical Engineers National Student Meeting 2008, Philadelphia, PA

Experience: University of Washington, Advisor: Professor Charles T. Campbell
Seattle, WA 98105
Ph. D. Candidate April 2012-Present

- Studying energetics of molecular fragments on metal and metal-oxide surfaces using microcalorimetry. Preparation and characterization of metal and metal oxide thin films using Auger electron spectroscopy, X-ray photoelectron spectroscopy, low energy electron diffraction, ultra-high vacuum systems, mass spectrometry.

University of Washington, Advisor: Professor Hugh Hillhouse

Seattle, WA 98105

Graduate Research Assistant

Nov 2010-April 2012

- Development, preparation, and characterization of a novel thin film fuel cell device using spin coating, sol gel chemistry, physical vapor deposition, chemical vapor deposition, current-voltage techniques and impedance spectroscopy. Development of theoretical model for device performance in Mathematica.

Illinois Institute of Technology, Advisor: Professor Jai Prakash

Chicago, IL 60616

Undergraduate Research Assistant

Sept 2008 – May 2010

- Investigation of heat evolution in Li-ion batteries using isothermal microcalorimetry and differential scanning calorimetry.

University of Delaware, Advisor: Professor Jochen Lauterbach

Newark, DE 19716

National Science Foundation Research Experience for Undergraduates Fellowship

June 2009-Aug 2009

- Study of CO adsorption on Pt(100) surface using polarization modulation infrared reflection adsorption spectroscopy

Activities: University of Washington Chemical Engineering Department Distinguished Young Scientist Seminar Series

Lead Organizer 2013, Panelist 2011-14

- Solicit for and collect application packages for potential seminar speakers. Lead application review panel of 24 graduate students. Organize schedules and travel for seminar speakers.

Puget Sound Chapter American Institute of Chemical Engineers

Webmaster 2012-2014, Member 2010-2014

- Post/Advertise event announcements and job opportunities. Manage event registration and event payment systems. Maintain chapter website.

Young Engineering Professionals of Puget Sound

Annual Meeting Planning Committee 2013,14

- Coordinate with 12 professional engineering societies to plan annual meeting including a networking session, dinner, and presentations from each society. Created webpage to advertise event and manage registration payments.

University of Washington Association of Chemical Engineering Graduate Students

Professional Development Committee 2010, Member 2010-Present

- Organize 2010 Chemical Engineering Graduate Symposium

IIT Student Chapter of the American Institute of Chemical Engineers

President 2008, Treasurer 2007, Member 2006-10

Awards:

2010 McCormack Award – AIChE Chicago Section

2009 NSF REU Fellow at University of Delaware
Heald Scholarship at Illinois Institute of Technology

Outreach: University of Washington Engineering Discover Days 2011-13
University of Washington Paws on Science 2013
Seattle Science Festival 2012-13